Luiz Henrique Accorsi Gans

Design study of a reversible lobe pump-turbine for low-head seawater pumped hydro storage applications

Doctoral thesis
for the degree of Philosophiae Doctor

Trondheim, April 2024

Norwegian University of Science and Technology
Faculty of Engineering
Department of Energy and Process Engineering

NTNU
Norwegian University of
Science and Technology

NTNU

Norwegian University of Science and Technology

Doctoral thesis
for the degree of Philosophiae Doctor

Faculty of Engineering
Department of Energy and Process Engineering

ISBN 978-82-326-7826-6 (printed version)
ISBN 978-82-326-7825-9 (electronic version)
ISSN 1503-8181 (printed version)
ISSN 2703-8084 (electronic version)

Doctoral theses at NTNU, 2024:116

Printed by Skipnes Kommunikasjon AS

We keep moving forward, opening new doors, and doing new things, because we're curious and curiosity keeps leading us down new paths.

- Walt Disney

To my wife Ana Luiza and my little son Henrique.
Thank you for inspiring and motivating me.
Amo vocês.

Abstract

Hydropower stands as the world's largest renewable electrical grid source, playing a pivotal role in the current green transition. Beyond its inherent significance in power generation, hydropower has leveraged energy storage for over a century through pumped hydro storage (PHS). This technology allows the storage of surplus power generated from diverse sources, subsequently reintroducing it to the grid during periods of increased demand. In contemporary times, PHS also contributes significantly to grid stability, particularly for intermittent sources like wind and solar power.

As water reservoirs at higher elevations have been extensively tapped, attention has shifted towards lower-level reservoirs. Exploring very low-head reservoirs, up to 30 m, poses unique challenges where conventional fluid machinery used in high-head scenarios becomes impractical. In this unexplored domain, alternative machines capable of operating in both pump and turbine modes emerge as promising technologies, offering innovative solutions for harnessing hydropower in diverse settings.

Therefore, the research in this PhD Thesis focuses on designing an efficient Positive Displacement Reversible Pump-Turbine (PD RPT) within Work Package 2 (WP2) of the European project ALPHEUS. Specifically, the study optimizes the round-trip efficiency of a reversible lobe-pump through Computational Fluid Dynamics (CFD) simulations.

Parameter calculations guided an experiment design at Chalmers, where valuable measurements and Particle Image Velocimetry (PIV) data validated numerical simulations for a three-lobe pump and turbine model scale.

Simulations with the Immersed Boundary Method (IBM) started as the potential technique for lobe pump applications, but due to issues related to accuracy, reliability, and computational cost, it was replaced by the deforming mesh approach with pre-generated meshes with TwinMesh. The new technique excluded the need for any interpolations due to overlapping meshes like in IBM, and since it presents a fixed structured mesh topology, no interpolation solution was needed during transient

simulations, as it occurs in the remeshing approach. That change in technique led to a substantial reduction in numerical errors and decreased simulation time while maintaining a high-quality, rotating, and adaptable mesh.

During validation, sensitivity studies assessed the impact of gaps in flow rate values, which is crucial for low-head pumped hydro storage. ANSYS CFX simulations with rotors at low rotation speeds probed machine properties under low-head conditions.

Subsequent CFD simulations were geared towards parametric design optimization, evaluating factors such as gaps between rotors, gaps between rotors and casing, and the ratio between the inlet width and the rotor diameter for fixed pressure head and rotation speed. Additionally, a simplified structural analysis was performed to assess structural loads and deformations.

The culmination of the research involved synthesizing insights gained from the first rig, CFD validation, third-party publications, and design optimization analyses to contribute to the formulation of a new experiment design at Technische Universität Braunschweig (TUB). This model-scale rig is expected to serve as a proof of concept for the reversible lobe pump-turbine. Analytical estimations and CFD simulations provided valuable characteristics curves for the system dynamics, offering insights into flow rates in pump and turbine modes, torques, generated power, efficiency as functions of rotation speed, and as well for pulsation levels. The culmination of this effort resulted in a commendable maximum round-trip efficiency of 83.9% when operating at 140 rpm, aligning with the primary objective of this thesis to attain round-trip efficiency values surpassing 70%.

In summary, this PhD thesis not only enhances the understanding of positive displacement reversible pump-turbines but also contributes to the broader goal of developing sustainable hydropower solutions. While providing valuable insights, unanswered questions and emerging challenges underscore the need for continued research. Additionally, exploring prototype-scale applications could be a promising avenue for future investigations.

Sammendrag

Vannkraft står frem som verdens største fornybare elektriske kraftkilde, og spiller en avgjørende rolle i den pågående grønne overgangen. Ut over sin iboende betydning for kraftproduksjon har vannkraft benyttet energilagring i over et århundre gjennom pumpekraftlagring (PHS). Denne teknologien tillater lagring av overskuddskraft generert fra forskjellige kilder, og gjeninnfører det deretter til strømnettet under perioder med økt etterspørsel. I moderne tid bidrar PHS også betydelig til nettstabilitet, spesielt for intermittente kilder som vind- og solkraft.

Etter at vannreservoarer i høyere høyder har blitt grundig utnyttet, har fokuset blitt rettet mot reservoarer på lavere nivå. Utforsking av svært lavtliggende reservoarer, opp til 30 m, gir unike utfordringer der konvensjonell fluidmaskinteknologi brukt i høytliggende scenarier blir upraktisk. I dette uutforskede området dukker alternative maskiner opp, som er i stand til å operere både som pumpe og turbin, og fremstår som lovende teknologier som tilbyr innovative løsninger for å utnytte vannkraft i forskjellige miljøer.

Derfor fokuserer forskningen i denne doktoravhandlingen på å utforme en effektiv positiv fortrengnings-reversibel pumpe-turbin innenfor arbeidspakke 2 (WP2) av det europeiske prosjektet ALPHEUS. Spesifikt optimaliserer studien round-trip-effektiviteten til en reversibel lobe-pumpe gjennom simuleringer med Computational Fluid Dynamics (CFD).

Parametervalg veiledet et eksperimentelt design ved Chalmers, der verdifulle målinger og Particle Image Velocimetry (PIV) data validerte numeriske simuleringer for en trelappet pumpe- og turbinmodell i liten skala.

Simuleringer med Immersed Boundary Method (IBM) startet som den potensielle teknikken for lobe-pumpeapplikasjoner, men på grunn av problemer knyttet til nøyaktighet, pålitelighet og beregningskostnader ble den erstattet av tilnærmingen med deformerende mesh ved bruk av forhåndsopprettede mesh med TwinMesh. Den nye teknikken utelukket behovet for interpolasjoner på grunn av overlappende mesh som i IBM, og siden den presenterer en fast strukturert mesh-topologi, var det ikke nødvendig med interpolasjonsløsning under transient simuleringer, som det

skjer i remeshing-tilnærmingen. Denne endringen i teknikk førte til en betydelig reduksjon i numeriske feil og redusert simuleringstid samtidig som det opprettholdt et høykvalitets, roterende og tilpasningsdyktig mesh.

Under validering vurderte sensitivitetsstudier virkningen av hull i verdier for strømningshastighet, noe som er avgjørende for lavtrykkspumpekraftlagring. ANSYS CFX-simuleringer med rotorer ved lave rotasjonshastigheter utforsket maskinegenskaper under lavtrykksforhold.

Etterfølgende CFD-simuleringer var rettet mot parametrisk designoptimalisering, der faktorer som hull mellom rotorer, hull mellom rotorer og hus, og forholdet mellom innløpsbredde og rotordiameter ble evaluert for fast trykkhode og rotasjonshastighet. I tillegg ble det utført en forenklet strukturanalyse for å vurdere strukturelle belastninger og deformasjoner.

Forskningens kulminasjon involverte syntese av innsikt fra det første riggen, CFD-validering, tredjeparts publikasjoner og designoptimeringsanalyser for å bidra til formuleringen av et nytt eksperimentelt design ved Technische Universität Braunschweig (TUB). Denne modellskala riggen forventes å fungere som en konseptbevis for den reversible lobe pumpe-turbinen. Analytiske estimater og CFD-simuleringer ga verdifulle karakteristikk-kurver for systemdynamikken, og tilbød innsikt i strømnivåer i pumpe- og turbinmodi, dreiemomenter, generert kraft, effektivitet som funksjoner av rotasjonshastighet, samt for pulsnivåer. Kulminasjonen av denne innsatsen resulterte i en prisverdig maksimal round-trip-effektivitet på 83.9% ved drift ved 140 rpm, i tråd med hovedmålet for denne avhandlingen om å oppnå round-trip-effektivitetsverdier over 70%.

Oppsummert forbedrer denne doktoravhandlingen ikke bare forståelsen av positive fortrengnings-reversible pumpe-turbiner, men bidrar også til det bredere målet om å utvikle bærekraftige løsninger for vannkraft. Mens den gir verdifulle innsikter, understreker ubesvarte spørsmål og nye utfordringer behovet for fortsatt forskning. I tillegg kan utforsking av prototypskala-applikasjoner være en lovende vei for fremtidige undersøkelser.

Resumo

A energia hidrelétrica destaca-se como a maior fonte renovável de eletricidade do mundo, desempenhando um papel fundamental na atual transição verde. Além de sua importância intrínseca na geração de energia, a energia hidrelétrica tem utilizado o armazenamento de energia por mais de um século por meio do armazenamento bombeado (PHS). Essa tecnologia permite o armazenamento de energia excedente gerada por diversas fontes, reintroduzindo-a posteriormente na rede durante períodos de aumento da demanda. Atualmente, o PHS também contribui significativamente para a estabilidade da rede, especialmente para fontes intermitentes como energia eólica e solar.

À medida que os reservatórios de água em altas elevações foram extensivamente explorados, a atenção voltou-se para reservatórios em níveis mais baixos. A exploração de reservatórios de muito baixa queda, até 30 m, apresenta desafios únicos, nos quais máquinas de fluido convencionais usadas em cenários de alta queda se tornam impraticáveis. Nesse domínio inexplorado, máquinas alternativas capazes de operar tanto no modo bomba quanto em modo turbina surgem como tecnologias promissoras, oferecendo soluções inovadoras para aproveitar a energia hidrelétrica em ambientes diversos.

Portanto, a pesquisa nesta Tese de Doutorado concentra-se no projeto de uma eficiente Bomba-Turbina Reversível de Deslocamento Positivo (PD RPT) dentro do Pacote de Trabalho 2 (WP2) do projeto europeu ALPHEUS. Especificamente, o estudo otimiza a eficiência de ida e volta de uma bomba de lóbulo reversível por meio de simulações de Dinâmica dos Fluidos Computacional (CFD).

Cálculos de parâmetros orientaram um projeto experimental na Chalmers, onde medidas valiosas e dados de Velocimetria por Imagem de Partículas (PIV) validaram simulações numéricas para um modelo em escala reduzida de bomba e turbina de três lóbulos.

Simulações com o Método de Contorno Imerso (IBM) foram iniciadas como uma potencial técnica para aplicações de bomba de lóbulo, mas devido a questões relacionadas à precisão, confiabilidade e custo computacional, foi substituído pela

abordagem de malha deformável com malhas pré-geradas com TwinMesh. A nova técnica excluiu a necessidade de quaisquer interpolações devido a malhas sobrepostas, como no IBM, e, uma vez que apresenta uma topologia de malha estruturada fixa, nenhuma solução de interpolação foi necessária durante simulações transitórias, como ocorre na abordagem de remeshing. Essa mudança de técnica resultou em uma redução substancial nos erros numéricos e no tempo de simulação, mantendo uma malha rotativa e adaptável de alta qualidade.

Durante a validação, estudos de sensibilidade avaliaram o impacto das folgas nos valores de taxa de fluxo, o que é crucial para o armazenamento bombeado em baixa queda d'água. Simulações realizadas no ANSYS CFX com rotores em baixas velocidades de rotação exploraram as propriedades da máquina em condições de baixa queda.

Em seguida, novas simulações CFD foram direcionadas para a otimização do projeto paramétrico, avaliando fatores como folga entre rotores, folga entre rotores e caixa, e a proporção entre a largura da entrada e o diâmetro do rotor para uma pressão e velocidade de rotação fixas. Além disso, uma análise estrutural simplificada foi realizada para avaliar cargas e deformações estruturais.

Essa pesquisa culminou na síntese de insights obtidos a partir do primeiro experimento, validação por CFD, publicações de terceiros e análises de otimização de design para a formulação de um novo projeto experimental na Technische Universität Braunschweig (TUB). Espera-se que este experimento em escala modelo sirva como uma prova de conceito para a bomba-turbina de lóbulo reversível. Estimativas analíticas e simulações CFD forneceram curvas características valiosas para a dinâmica do sistema, oferecendo insights sobre as taxas de fluxo nos modos de bomba e turbina, torques, potência gerada, eficiência em função da velocidade de rotação e também para níveis de pulsação. Esse esforço culminou em uma eficiência máxima de ciclo de 83.9% ao operar a 140 rpm, alinhando-se com o objetivo principal desta tese de atingir valores de eficiência de ciclo superiores a 70%.

Em resumo, esta tese de doutorado não apenas aprimora a compreensão das bombas-turbinas reversíveis de deslocamento positivo, mas também contribui para o objetivo mais amplo de desenvolver soluções sustentáveis para a energia hidrelétrica. Ao fornecer insights valiosos, perguntas não respondidas e desafios emergentes destacam a necessidade de pesquisas contínuas. Além disso, a exploração de aplicações em escala de protótipo pode ser uma via promissora para investigações futuras.

Preface

This doctoral thesis represents the culmination of slightly over three years of rigorous and focused study. The research was conducted between September 2020 and January 2024 at the Waterpower Laboratory within the Department of Energy and Process Engineering at the Norwegian University of Science and Technology (NTNU). Additionally, a brief but intensive one-week research stint took place at the Laboratory of Fluid and Thermal Science at Chalmers University of Technology.

This work has received funding from the ALPHEUS project, a European Union's Horizon 2020 research and innovation program under grant agreement No. 883553. The ALPHEUS project intends to enhance and advance reversible pump turbine (RPT) technology along with the development of adjacent civil structures needed to make pumped hydro storage economically viable in shallow seas and coastal environments with flat topography.

The research endeavor encompassed the execution of computational fluid dynamic simulations for both pump and turbine modes within a reversible lobe pump machine, denoted as a positive displacement reversible pump turbine. Substantial progress in numerical validation was realized through extensive collaboration with our project partner at Chalmers University of Technology. Notably, the collaborative efforts with Delft University of Technology and Technische Universität Braunschweig expanded to encompass the design and implementation of a larger-scale rig specifically crafted for a reversible lobe pump turbine. This development represents a noteworthy advancement, marking a substantial stride towards attaining the overarching objectives of the ALPHEUS project.

In addition to the thesis, the author actively collaborated with diverse researchers, contributing to scientific publications. A review paper, a collaborative effort among multiple PhD candidates, supervisors, and other project partner scientists, has been successfully published in a peer-reviewed journal:

- Hoffstaedt, J.P., Truijen, D.P.K., Fahlbeck, J., **Gans, L.H.A.**, Qudaih, M., Laguna, A.J., De Kooning, J.D.M., Stockman, K., Nilsson, H., Storli, P.-T.,

Engel, B., Marence, M., & Bricker, J.D. (2022). Low-head pumped hydro storage: A review of applicable technologies for design, grid integration, control and modelling. *Renewable and Sustainable Energy Reviews, 158*, 112119. https://doi.org/10.1016/j.rser.2022.112119

Another peer-reviewed publication was published and presented at the International Symposium on "Current Research in Hydropower Technologies, CRHT-XI" in Kathmandu, Nepal, in 2023. In this paper, crucial insights from numerical investigations using the immersed boundary method are discussed and presented in Chapter 4 of this thesis, giving rise to the subsequent work:

- **Gans, L.H.A.**, Trivedi, C., Iliev, I., & Storli, P.T. (2023). An experimental and numerical study of a three-lobe pump for pumped hydro storage applications. *Journal of Physics: Conference Series, 2629(1)*, 012010. https://doi.org/10.1088/1742-6596/2629/1/012010

As a participant in the European project ALPHEUS, team members compile and document results in Deliverables for the Horizon 2020 European Commission. Throughout my PhD, I played a central role in shaping Deliverable 2.4. The associated published report, outlined below, encompasses various aspects and studies related to the multidisciplinary optimization of a positive displacement design.

- **Gans, L.H.A.** & Storli, P-T (2023). Multidisciplinary optimized PD design. *European Union's Horizon 2020, ALPHEUS*, grant agreement 883553. https://alpheus-h2020.eu/wp-content/uploads/2020/06/D2.4-Multidisciplinary-optimized-PD-design-V2.0.pdf

Furthermore, additional sections of this doctoral thesis are currently being prepared for publication in peer-reviewed journals.

Acknowledgments

First and foremost, I would like to express my deepest gratitude to my wife, Ana Luiza, for her unwavering support and understanding throughout these challenging years. Her encouragement and love have been my anchor, giving me the strength, motivation, and animation to persevere.

To my son, Henrique, whose infectious joy and laughter brought light to my life. Your presence has been a constant reminder of how great life can be and also to persevere amid my academic endeavors.

I owe a debt of gratitude to my main supervisor, Professor Pål-Tore Storli, for his guidance and support over three years. Pål-Tore not only made my days easier but also instilled in me the confidence to pursue my ideas and maintain a healthy work-life balance. I would like to acknowledge Professor Chirag Trivedi, who initially started as my co-supervisor but later took on the role of main supervisor. His assistance was invaluable in navigating the final steps of my thesis. Special thanks go to Dr. Igor Iliev, my co-supervisor, for countless hours of insightful discussions on numerical results. His contributions played a crucial role in launching the simulations and setting the foundation for the research.

This work was only possible within the framework of the ALPHEUS project, funded by the European Union's Horizon 2020 research and innovation program under grant agreement No. 883553. I express my gratitude to the European Union for its financial support of this project. I also want to express my gratitude to all the PhD students and researchers in the ALPHEUS project for the sense of community and shared experiences during consortium and regular meetings. Your collaboration provided a valuable platform for exchanging crucial information, enriching my research journey. Thank you all.

A heartfelt thank you to all the professors, researchers, PhD and Master's students from Vannkraftlaboratoriet at NTNU who shared in my daily experiences. Your presence made my days more enjoyable and brought fun to the challenging academic environment, especially during the quizzes and table tennis matches. I would also like to express my thanks to the Department of Energy and Process

Engineering (EPT) at NTNU for welcoming me into this exceptional academic community.

Last but not least, I cannot adequately express my gratitude to my family in Brazil who supported and cheered for me from afar, and also to my Brazilian friends in Trondheim, who made my stay feel a bit more like home.

In conclusion, I am grateful to everyone who contributed to my academic and personal growth. This thesis is a collective effort, and I am fortunate to have had such a dedicated and supportive network of individuals around me.

Contents

List of Tables

List of Figures

List of Symbols

Greek

Symbol	Definition	Unit
Δ	variation of a variable or function	
η	efficiency	
ρ	density	kg/m^3
ω	rotational speed	rad/s
ω_s	specific speed	

Latin

Symbol	Definition	Unit
A_r	rotor cross-section area	m^2
A_{rw}	rotor total water area	m^2
A_{rwc}	rotor water area of one chamber	m^2
B	rotor height	m
D	rotor diameter	m
g_{rr}	rotor-rotor gap	m
H	head	m
H_g	gross head	m
H_n	net head	m
k	number of cusps	
m	number of lobes	
n	rotational speed	rpm
n_s	rotational speed	rps
N_r	number of rotors	
p	pressure	Pa (bar)

p_{atm}	atmospheric pressure	Pa (atm)
P	power	W
P_n	net power	W
Q	volumetric flow rate	m^3/s (LPM)
r	radius of the rolling circle	m
t	parametric parameter	
T	torque	N m
u	velocity component in the x-axis	m/s
v	velocity component in the y-axis	m/s
V	volume	m^3
w	velocity component in the z-axis	m/s
W	width	m
x, y, z	coordinate-axes	

Mathematical constants

Symbol	Definition	Value
π		3.14159

Physical constants

Symbol	Definition	Value
g	gravitational acceleration	$9.8067\ \text{m s}^{-2}$

Subscripts

Symbol	Definition
atm	atmospheric
avg	average
epi	epicycloid
g	gross
hyp	hypocycloid
max	maximum
n	net
p	pump
pot	potential
t	turbine

List of Acronyms

ALPHEUS	Augmenting Grid Stability Through Low Head Pumped Hydro Energy Utilization and Storage
CAD	Computer-Aided Design
CFD	Computational Fluid Dynamics
EU	European Union
FSI	Fluid-Structure Interaction
GHG	Greenhouse Gases
IBM	Immersed Boundary Method
IPCC	Intergovernmental Panel on Climate Change
LH	Low-Head
MSSF	Momentum Source Scaling Factor
NTNU	Norges Teknisk-Naturvitenskapelige Universitet
PD	Positive Displacement
PhD	Philosophiae Doctor
PHS	Pumped Hydro Storage
PIV	Particle Image Velocimetry

RANS	Reynolds-Averaged Navier–Stokes
RPT	Reversible Pump Turbine
TUB	Technische Universität Braunschweig
WP2	Work Package 2

CHAPTER

ONE

Introduction

The escalating levels of greenhouse gases (GHG) in the atmosphere have precipitated a surge in the global average temperature. In response, the Earth is witnessing more pronounced climatic events, including the alarming melting of the Arctic, rising sea levels, increased ocean acidity, diminishing drinking water sources, and other ecological shifts (IPCC, 2013).

Since the Third Assessment Report of the Intergovernmental Panel on Climate Change (IPCC), there has been a heightened certainty that an average temperature increase of 1.5ºC-2.5ºC compared to pre-industrial levels poses significant risks to numerous unique and threatened ecosystems. The potential extinction risk for nearly 20%-30% of species looms large if the global average warming surpasses these thresholds. The repercussions extend to food safety and human health, with cereal crop productivity expected to decline in low latitudes and alterations in the distribution of disease vectors, such as malaria-bearing mosquitoes (IPCC, 2023).

In a concerted effort to mitigate the consequences of global warming and bolster the safety of all species, diverse solutions have been implemented to decarbonize the system. Among these, the widespread adoption of renewable energies has garnered international attention. Power derived from hydropower plants, solar and wind energy, and biomass can supplant polluting sources like oil, gas, shale, and coal, facilitating the world's transition towards cleaner energy options.

As the share of intermittent renewable energy sources grows, and to facilitate higher penetration of these energy supplies, the implementation and expansion of energy storage systems become imperative for maintaining grid stability and enhancing flexibility. Energy storage technologies play a crucial role in storing energy during periods of low demand or costs and redistributing it when demand or costs are high (ALPHEUS, 2023).

In the ever-evolving landscape of global energy systems, the imperative to

transition towards sustainable and renewable sources is indisputable. Among the contributors to this transformative journey, pumped hydro storage (PHS) stands out as a cornerstone technology, demonstrating resilience and adaptability since its inception at the beginning of the 20th century. As of 2020, PHS accounted for over 90% of the world's bulk energy storage, exemplifying its historical dominance in providing grid stability and energy balancing (*Renewables 2021 global status report* 2021).

Renewable energy sources, particularly solar photovoltaics and wind generation, have experienced remarkable growth, constituting 29% of the worldwide electricity mix in 2020 (IEA, 2021). However, the intermittent nature of these sources poses challenges to grid stability, necessitating advanced energy storage solutions. While PHS has traditionally been a stalwart in energy storage, its historical reliance on high-head applications limited its deployment to specific topographies, leaving regions with flat landscapes underserved.

This thesis delves into the pivotal realm of low-head pumped hydro storage, an emerging frontier that has, until now, received limited attention (Barnhart and Benson, 2013). The conventional high-head PHS, leveraging significant topographic differences, has proven effective but faces constraints in scalability and geographical applicability. The need for diverse energy storage solutions, especially in regions lacking the necessary topographic features, has driven a shift in focus towards low-head PHS as a potential game-changer (Jülch, 2016).

The historical trajectory of PHS reveals its roots in the mountainous regions of central Europe in the early 20th century, with small-scale plants utilizing separate pumps and turbines (Rehman et al., 2015). The subsequent evolution toward combined reversible pump-turbines in the mid-20th century marked a turning point, fostering a boom in Europe, Asia, and North America during the 1960s, 1970s, and 1980s. This expansion was particularly pronounced alongside the increasing capacity of nuclear power and the energy crisis of the 1970s, where PHS provided a flexible solution for matching varying demand with the baseload generation of nuclear power plants (Rehman et al., 2015).

However, the historical growth of PHS experienced a slowdown in many regions after the 1980s, with the exception of China, whose rapidly growing economy and reliance on non-flexible coal plants spurred a demand for major energy storage (Barbour et al., 2016). Noteworthy advancements in the 1990s introduced variable speed operation in Japan, enhancing efficiency, reducing switching times, and facilitating quicker response times (Joseph et al., 2018). This marked a pivotal moment, laying the groundwork for continued innovation in response to the evolving landscape of renewable energy sources in subsequent decades.

The emerging trends in PHS underscore the pressing need for flexible and large-scale energy storage solutions, especially with the increasing share of intermittent

renewable energy sources (IRES) in recent decades (Ardizzon et al., 2014). Two notable trends driving innovation include the changing grid characteristics necessitated by a reduction in spinning reserves and the expanding operating range and application of PHS. To address these trends, research efforts are exploring improved control mechanisms, novel hybrid storage solutions, and the potential of low-head PHS for regions with flat topographies (Kougias et al., 2019). Figure 1.1 shows a conceptual design of a low-head pumped hydro storage station at the seawater level.

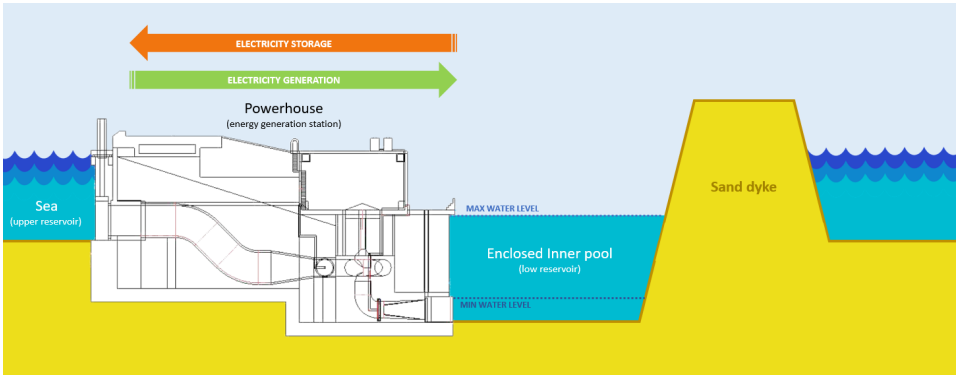

Figure 1.1: Conceptual design of a low-head PHS station (ALPHEUS, 2023).

1.1 ALPHEUS Project

To meet European Union targets on climate emissions reduction and expedite the green transition, the ALPHEUS Horizon 2020 project is focused on utilizing pumped hydropower energy storage systems (PHS). This matured technology accounts for the majority of global energy storage capacity (*Renewables 2021 global status report* 2021). ALPHEUS aims to enhance reversible pump-turbine (RPT) technology and related civil structures, making PHS economically viable in shallow seas and coastal environments with flat topography (Qudaih et al., 2023).

Specifically, ALPHEUS seeks to develop low-head seawater-compatible pumped hydro storage technologies suitable for European sites. These implementations will address discrepancies between energy supply and demand on timescales ranging from minutes to days. The modular design allows for scalability between 300 kW and 30 MW, accommodating local and regional demand and supply characteristics variations.

In the realm of various reversible pump-turbine technologies being assessed by ALPHEUS for low-head seawater pumped storage applications, the positive displacement RPT emerges as a potentially fish-friendly, seawater-robust, and cost-effective technology.

A significant challenge for ALPHEUS is to comprehensively understand the

advantages and disadvantages of such a machine. Consequently, this doctoral project will investigate a positive displacement RPT technology to optimize its design and position it as a feasible solution. The description of such machines are presented in Chapter 2 Section 2.1.

1.2 Overall Objectives

The main objective of this Thesis is to provide an optimized design of a reversible positive displacement pump, determine its operating conditions, and check its applicability in low-head pumped hydro storage applications.

Given the absence of tested and validated positive displacement (PD) pumps as a viable reversible machine for low-head PHS and the lack of prior exploration in this domain, several pertinent questions arise. In a landscape where centrifugal pumps traditionally dominate power production and PHS applications, the feasibility of PD machines handling low-viscosity fluids like water while maintaining commendable efficiencies in turbine mode becomes a focal inquiry. Questions also extend to the overall efficiencies achievable in both pump and turbine modes, the power generation capacity of a single PD machine under varying conditions, and whether the inherent pulsating nature of PD machines presents challenges or restrictions.

In light of these queries, a concise set of specific objectives has been formulated.

1.3 Specific Objectives

- Execute numerical investigations, especially Computational Fluid Dynamics (CFD) for a positive displacement reversible pump-turbine.
- Validate models and simulations by comparing the results with experimental data.
- Address possible design optimizations to increase the round-trip efficiency, which is expected to be 70% or higher.
- Examine the characteristic curves thoroughly and address any concerns related to the relevant pulsations.
- Perform simple structural analyses to determine mechanical loads and deformations on the rotors in order to present an initial estimation of structural safety.

1.4 Scope

This project primarily focuses on the geometry optimization of rotary positive displacement pumps in low-head applications, specifically studying lobe pumps. Various characteristics will be addressed and numerically investigated to enhance their performance. These include the number of lobes, profile of the rotor surface, gap size between the rotor and casing, clearance between two rotors, inlet and outlet shapes and sizes, twist angle for twisted rotors, etc. The optimization process

will be conducted through Computational Fluid Dynamics (CFD) simulations. Subsequent structural analyses are planned to identify loads in the rotors. However, comprehensive simulations involving fluid-structure interaction (FSI), which could offer insights into fatigue-related issues, are not covered in this Thesis.

An experienced member of the ALPHEUS project will orchestrate experimental tests at Chalmers and perform measurements using the index-matching Particle Image Velocimetry (PIV) technique. Data obtained from these tests will be a foundational basis for validating the CFD results.

Despite the interface between fluid and solid mechanics, studies regarding material selection are separate from the scope and should be separate from a deeper investigation. Cavitation studies are also excluded.

The principal objective of this project is to furnish technical data on efficiency values for one Positive Displacement Reversible Pump/Turbine (PD RPT) technology and economic analyses are explicitly excluded from the scope.

CHAPTER
TWO

Literature Review

The selection of a reversible pump-turbine (RPT) unit is influenced by various factors. Primarily, the power of a hydropower plant is a function of head, flow rate, and overall efficiency, given by Eq. (1), which is also described by Dixon and Hall (2014).

$$P = \rho g H Q \eta \tag{2.1}$$

Here, ρ represents water density, g is the gravity acceleration, H is the head applied to the machine after deducting hydraulic losses in the system (friction and local losses), Q is the volumetric flow rate, and η is the overall efficiency. Notably, low-head scenarios with high volumetric flow rates present better opportunities for power production (McLean and Kearney, 2014).

Defining low-head is subject to interpretation among different institutions. Heads in the range of 2-30 meters are considered low-head, under The European Small Hydropower Association (ESHA) classification for low-head hydropower plants (Loots et al., 2015). Low-head pumped hydro storage (LH PHS) poses economic challenges as the overall efficiency is more sensitive to head losses (Hunt et al., 2020).

The specific speed ω_s of a reversible pump-turbine or a pump used as a turbine is a crucial parameter in selecting the appropriate configuration. It is defined as per Dixon and Hall (Dixon and Hall, 2014):

$$\omega_s = \omega Q^{1/2} (gH)^{3/4} \tag{2.2}$$

Here, ω is the runner rotational speed, Q is the volumetric flow rate, and H is the head. Machines with low rotational speeds and small shear forces are more fish-friendly, while axial configurations are preferable for higher specific speeds (Ak et al., 2017; Karassik, 2001).

Pump-turbine selection depends on factors such as the type of machine, operation mode (variable or fixed speed), and reservoir configuration. Radial or mixed-flow machines are suitable for high heads, while axial configurations are more effective in low-head (LH) applications due to their higher flow rates and cost-effectiveness (Breeze, 2018; Karassik, 2001).

Axial-flow pump-turbines with two counter-rotating runners have been proposed for low-head PHS, offering advantages such as smaller size, stable head-flow rate characteristics, and a wider efficiency range with individual speed control (Fahlbeck et al., 2021; Furukawa et al., 2007; Kim et al., 2018). Non-conventional machines like the Archimedes screw and positive displacement pumps are also explored for specific scenarios (Krampe and Ørke, 2012; YoosefDoost and Lubitz, 2020).

Pump-turbines in PHS applications can operate at fixed or variable rotational speeds. Variable speed machines provide a wider operating range and greater flexibility but come with higher costs (Bocquel and Janning, 2005; Hunt et al., 2020; Javed et al., 2020).

In conclusion, the design and configuration of pump-turbines for low-head pumped hydro storage involve carefully evaluating various parameters. The choice of machine type, specific speed, and operational mode depends on the particular characteristics of the hydropower plant and its intended application.

For an in-depth examination of pump-turbine design and configuration tailored for low-head pumped hydro storage, kindly consult Appendix B.1 for the co-authored paper produced during this Thesis, in the comprehensive work of Hoffstaedt et al. (2022). This paper constitutes an integral research component contributing to developing this PhD Thesis.

2.1 Positive Displacement Machines

Positive Displacement (PD) pumps, by definition, move a specific volume of liquid with each revolution of the pumping elements. These pumps achieve displacement by creating a space (commonly referred to as a cavity or chamber) between the pumping elements, wherein the liquid is trapped. The rotation of these pumping elements then expels the liquid from the pump. Positive displacement pumps exhibit versatility, accommodating fluids of various viscosities up to 1,320,000 cSt, capacities reaching up to 1,150 m^3/h, and pressures up to 700 bar. Notably, positive displacement pumps present numerous advantages compared to kinetic flow machines. PD pumps are self-priming and can provide a consistent, smooth flow, unaffected by pressure fluctuations. They usually generate low flow rates, possess the capability to manage significant variations in head without a notable impact on their efficiency, and are frequently considered an optimal option for handling viscous fluids or those containing solids or precipitates that require treatment. Typically, these machines are categorized into two main groups: reciprocating and rotary.

However, their elevated initial cost stands as a drawback when contrasting these machines with centrifugal counterparts (Karassik, 2008; Pump School, 2023; White and Chul, 2016).

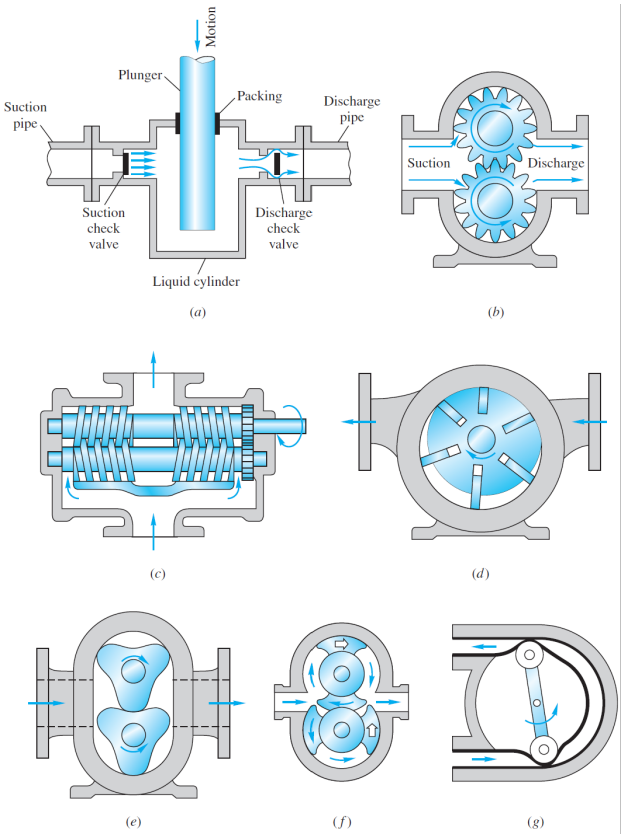

Figure 2.1: Examples of positive-displacement pumps: (a) reciprocating piston or plunger, (b) external gear pump, (c) double-screw pump, (d) sliding vane, (e) three-lobe pump, (f) double circumferential piston, (g) flexible-tube squeegee. Source: White and Chul (2016).

Several types of positive displacement machines include internal gear, external gear, vane, flexible member, lobe, circumferential piston, and screw pumps. Figure 2.1 illustrates a few examples of these PD pumps.

Figure 2.2 shows different general performance behavior between PD and centrifugal machines. The performance chart highlights significant differences, showing that centrifugal pumps exhibit variable flow based on pressure or head, while PD pumps maintain a more constant flow regardless of pressure. Another critical distinction emerges in the impact of viscosity on pump capacity, evident in the flow rate chart. Centrifugal pumps experience a decrease in flow with rising viscosity,

whereas PD pumps show an increase due to higher volumetric efficiency caused by viscous liquids filling pump clearances. Examining efficiency charts reveals varying responses to pressure changes, with PD pumps remaining relatively unaffected while centrifugal pumps exhibit significant sensitivity. Additionally, viscosity influences mechanical efficiency, leading to decreased efficiency in centrifugal pumps at higher viscosities, in contrast to PD pumps, where efficiency often increases with viscosity.

For water applications, where viscosity typically hovers around 1 cSt, this singular parameter alone could elucidate the prevalent choice of centrifugal machines. This comprehensive understanding aids in making informed decisions when selecting the appropriate pump type based on specific operational considerations. Consider that a centrifugal pump performs optimally at the center of its curve, with additional factors influencing pump life if deviating to the left or right, such as shaft deflection or increased cavitation. In contrast, a positive displacement pump allows operation at any point on the curve, with improved volumetric efficiency at high speeds due to the constant nature of slip (leakage), which is more pronounced at lower speeds.

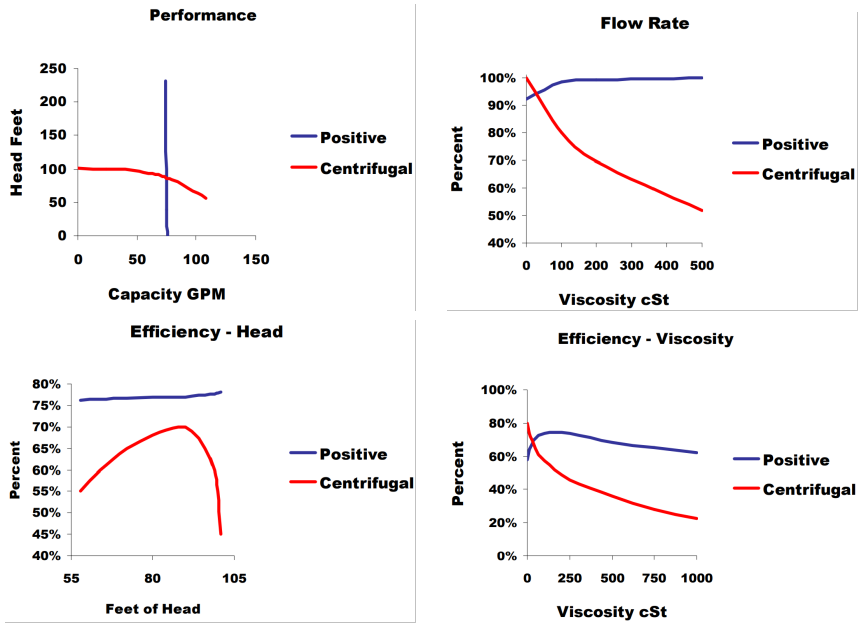

Figure 2.2: Comparison between characteristic curves from positive displacement machines and centrifugal machines. Source: Pump School (2023).

Among PD machines five distinct technologies are commonly selected for various applications. Table 2.1 illustrates their differences concerning overall decision

criteria. This nuanced understanding establishes the foundation for making informed and strategic decisions in selecting the most appropriate PD pump technology for various applications within the scope of this study.

Table 2.1: Comparison of Positive Displacement pump technologies (Hall, 2023)

Decision Criteria	Lobe	Progressive Cavity	Air-Operated Diaphragm	Timed Two-Screw	Gear
Low shear (speed-dependent)	Excellent	Excellent	Excellent	Excellent	Excellent
Efficiency	Excellent	Excellent	Poor	Excellent	Excellent
Reversible direction of flow	Yes	Model dependent	No	Model dependent	Yes
Run dry capability	Excellent	Poor	Excellent	Excellent	Good (material dependent)
Handling of thin to thick liquids	Excellent	Excellent	Very good	Excellent	Excellent
Cleanability	Excellent	Very good	Good	Good	Good
Pressure capabilities	To 27.5 bar	To >69 bar (multistages for higher pressure)	Limited to plant air pressure, usually 7 bar	To >69 bar psi	Internal gear to 19 bar External gear to >69 bar
Abrasive liquid handling	Good	Very good	Very good	Good	Very good
Metering capability	Excellent	Excellent	Poor	Excellent	Excellent

Analysis of Table 2.1 reveals that lobe pumps, progressive cavity, timed two-screw and gear pumps emerge as possible technologies as they may include reversibility, making them suitable for use as turbines. Moreover, all those types exhibit excellent efficiency levels and operate within the pressure range required for low-head pumped hydro storage applications. In the specific context of the ALPHEUS project, where saltwater is the working fluid, cleanability and abrasive liquid handling are desirable, and all those four PD pumps have good to excellent evaluation.

In low-head pumped hydro storage, the PD pump necessitates a size ten times that of traditional counterparts to accommodate the required mass flow. Nevertheless, the advantageous characteristics of hydrostatic PD pumps persist even at this larger scale. Positive displacement pumps stand out for their ability to achieve high efficiencies across diverse pumping conditions, including variations in head. In contrast, dynamic and centrifugal pumps encounter challenges when operating outside their designed working points (RONAMIC, 2017).

In low-head seawater PHS, the presence of aquatic life, such as algae and fish, adds other needs in design to mitigate environmental impacts and protect the reversible machine. Moreover, rotary positive displacement devices have already been explored for application as micro hydro turbines in water supply pipelines, demonstrating efficiencies ranging from 60% to 80% under pressures up to 5 bar (equivalent to a hydraulic head of 51 meters) (Kurokawa et al., 2008; Sonawat et al., 2020). Compared to the other PD technologies, lobe pumps present a smoother design to handle aquatic life, so it was the chosen machine to be further evaluated in the ALPHEUS project. For a detailed review of positive displacement machines

in the context of low-head PHS, please refer to Chapter 3 of the review paper Hoffstaedt et al. (2022), included in Appendix B.1.

While lobe pumps may incur higher initial costs due to the mandatory inclusion of timing gears, coupled with the potential need for a gear reducer, gear motor, or a belt- or variable-speed drive (Hall, 2023), these upfront expenses are counterbalanced by their notable efficiency and low maintenance, resulting in overall reasonable life-cycle costs.

Lobe pumps, with their suitability for low-pressure differentials and handling large volumes, fall into hydrostatic pumps. Figure 2.3 illustrates that the fundamental principle of a lobe pump involves two counter-rotating rotors that exert positive torque, compelling water to displace against the pressure difference within the system. This pressure discrepancy, also referred to as head, arises from varying water levels in distinct reservoirs. Notably, when water moves from a higher-pressure to a lower-pressure reservoir, the rotors function as turbines, generating power.

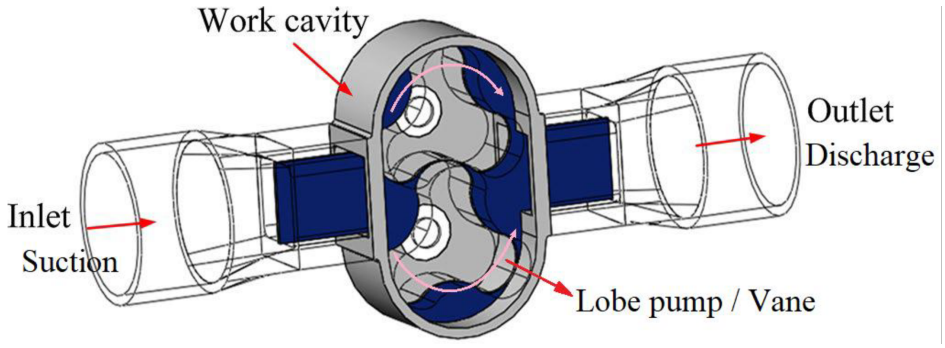

Figure 2.3: Basic design for lobe pump systems (Adapted from (Li et al., 2019))

Another intriguing aspect to consider is that, unlike a gear pump, the lobes of a lobe pump never actually touch. This unique feature allows rotors to be manufactured using highly corrosion-resistant materials (Hall, 2023). As the lobes rotate, they create a void on the suction side, facilitating fluid inflow into the chambers between the vanes and the casing. The fluid is then carried around the perimeter by each lobe's cavity. Upon the re-convergence of the lobes, the cavity shrinks, compelling the fluid to exit through the discharge port (Hall, 2023).

Rotors in lobe pumps manifest in various forms, ranging from two to six lobes or two wings (sharp-edged, scimitar-shaped lobes). Each configuration offers specific advantages and trade-offs concerning pump efficiency, solid handling, maintenance, and fluid pulsation. To minimize pulsation in a process, multi-lobe rotors or twisted lobes are preferred (Hall, 2023; Henn, 2012).

In conclusion, the lobe pump's distinctive design, coupled with its inherent

capability for solid handling, positions it as a promising candidate for deployment in maritime environments. With the capacity to handle challenges posed by saltwater and accommodate small particles such as sand, as well as potentially larger solid fragments, the lobe pump emerges as a viable solution. Importantly, its blade-free design enhances its compatibility with marine life, making it a potentially fish-friendlier option. Consequently, within the scope of Project ALPHEUS, the investigation extends to explore the lobe pump's potential as a fish-friendly design, acknowledging its unique attributes and suitability for applications in oceanic settings.

2.2 Lobe Pumps and Lobe Turbines Characterization

Defined by lobed rotors—commonly featuring two, three or four lobes per rotor—lobe pumps generate a smooth and consistent flow of fluids within their chambers. The lobes interlock seamlessly without direct contact, enabling a gentle yet robust transfer of liquids. The inherent symmetry of their lobed configuration induces controlled flow pulsations within the system. The magnitude of these pulsations may vary based on specific design elements; however, this characteristic renders lobe pumps particularly well-suited for applications demanding precision and controlled fluid handling.

Various aspects of PD RPT design can be examined to enhance efficiency. This section delves into existing literature on diverse parameters associated with lobe pumps or lobe turbines, elucidating their correlations with machine efficiency.

Within this realm, this section includes an analysis of how clearances influence efficiency, a comparison between the efficiency outcomes of cycloidal and circular rotor surface profiles, a determination of the optimal number of lobes for the rotor, assessing the viability of twisting rotors, and exploring the impact of different inlet and outlet channel shapes.

2.2.1 Rotor Surface Profile and Number of Lobes

In the pursuit of optimizing the positive displacement rotor design, a crucial consideration is the choice of rotor surface profile and the number of lobes, which can significantly impact performance.

Kang et al. (2012) shows that the unique geometry of this pump is usually characterized by alternating epicycloid and hypocycloid curves, and they delved into comparing circular and cycloidal profiles. Their study demonstrated that the cycloidal lobe induces less pressure drop, attributed to reduced vortex formation and lower speed. This advantageous combination prevents backward flow from the discharge to the suction area. Additionally, the cycloidal profile exhibited a characteristic curve with a higher slope ratio, enhancing pump efficiency by minimizing leakage levels in pump mode. The average pressure head of epicycloidal lobes was nearly 10% higher than that of circular pumps across all cases.

In evaluating multi-lobe pumps featuring up to 4 lobes, both tri- and four-lobe configurations demonstrated superior stability and capacity compared to the two-lobe design. However, there were no significant differences in performance efficiency between the tri- and four-lobe pumps. Consequently, while multi-lobe designs enhance stability and capacity, they do not notably improve pump efficiency.

2.2.2 Inlet and Outlet Channel Shapes and Sizes

The impact of varying cross-sectional shapes of inlet and outlet pipes on a four-lobe turbine with twisted rotors was explored by Sonawat et al. (2021). Their study, conducted through CFD simulations, compared circular, square, and rectangular pipe shapes that connected the lobe turbine to the system in order to identify the most efficient configuration.

The findings revealed that circular pipes generated stronger vortices and exhibited greater recirculation in the flow compared to rectangular pipes. Due to the improved alignment of the flow with the rotor area, a rectangular pipe shape yielded higher efficiencies by minimizing recirculation regions. In their study case and design, a rectangular pipe demonstrated a 0.824% higher hydraulic efficiency than its circular counterpart. Square pipes are pictured between circular and rectangular pipes in terms of performance.

Sonawat et al. (2021) also demonstrates that transitioning from a circular to a rectangular pipe cross-sectional shape is recommended to ensure higher efficiencies. Additionally, if the optimal shape aligns with the height of the rotor, it simplifies many optimization parameters into a 2D analysis. At the same time, for a fixed 2D design, increasing rotor height can enhance power generation. Maintaining an equivalent area between the rectangular and circular pipes is crucial to preserve the same flow rate and prevent increased pressure drop.

2.2.3 Clearance Size

In rotary lobe pumps and turbines, clearances exist between rotors and the casing, as well as between the rotors themselves. These spaces are crucial to prevent contact between the rotors or between the rotors and the casing during pump or turbine operation. Any contact can lead to changes in flow rate, pressure drop, leakages, and surface wear, impacting overall machine performance. Additionally, cavitation and unwanted vibrations may arise depending on clearance sizes. Therefore, determining the optimal clearance size is essential to ensure peak efficiency while mitigating potential operational issues.

Phommacchanh et al. (2006) introduced a design with spur gears around the curve shape of the rotors to enhance torque transmission. They focused on assessing PD turbine efficiency and the impact of leakage on efficiency. Their findings indicated that the PD turbine outperformed conventional turbines in terms of efficiency and maintained high efficiency across a broad range of operating conditions. The

study emphasized that reducing clearances between rotating and stationary parts significantly improved turbine efficiency by minimizing water leakage through these gaps. This aligns with fluid mechanics principles, precisely Couette flow, where velocity is proportional to the square of the gap size, implying that smaller gaps result in lower leakage.

Phommacchanh et al. (2006) observed a noticeable decrease in torque efficiency with small side clearances at low differential pressures. However, the improvement in volumetric efficiency with small side clearances far outweighed the reduction in torque efficiency. Furthermore, a PD turbine with smaller side clearances demonstrated higher output power and overall efficiency than a case with larger clearances at the same head and flow rate.

Consistent with these findings, Kang et al. (2012) confirmed that smaller clearances between the rotor and casing walls contributed to significantly higher efficiencies. In conclusion, the optimal design for the reversible lobe pump turbine requires minimizing tip gaps and side gaps, with final sizes defined by manufacturing and assembling constraints. Further investigation and testing are necessary to determine the best size for the rotor-rotor gap.

2.2.4 Twisted Rotors

To mitigate pressure pulsations in turbines, Kurokawa et al. (2008) suggest installing a small surge tank at the turbine's inlet and outlet, reducing pulsation amplitudes by 75%. However, they propose an alternative approach by studying a pair of four-lobe rotors twisted helically at an 11° angle, comparing it with a three-lobe rotor. In a straight three-lobe PD turbine, pressure pulsation significantly increases with higher rotational speed and differential pressure. Conversely, twisted rotors reduce pressure fluctuations to about 20% of those observed in the straight three-lobe rotor. Despite an anticipated increase in leakages through tip and center clearances due to the larger surface area of helical lobes, torque and leakage depend primarily on differential pressure, resulting in significantly higher torque efficiency.

Sonawat et al. (2021) emphasize the detrimental effects of large pulsations in flow, leading to noise, vibration, fatigue, and potential structural damage or breakdown of the device. They advocate for the use of twisted rotors to dampen flow fluctuations. Sonawat et al. (2020) conducted multi-phase CFD simulations in a study on cavitation in PD turbines and demonstrated that a 45° twisted rotor could practically eliminate cavitation. This is attributed to the uniform contact area of the fluid for both rotors, regardless of lobe orientation or rotation, preventing abrupt changes in fluid properties. Although the 45° twisted rotor exhibited a 1.15% decrease in theoretical hydraulic efficiency compared to the straight lobe design due to increased leakage losses, the resulting vibration-free operation enhances machine longevity and reduces maintenance costs.

2.3 Parametric Equations for Lobe Pump

In order to pursue the best design for ALPHEUS PD RPT, lobe pumps with cycloidal were chosen as the optimal choice, as explained by Kang et al. (2012).

In lobe pumps with cycloidal-based profiles, epicycloidal and hypocycloidal curves alternate to form the rotor, and they are specific types of curves traced by a point on the circumference of a circle as it rolls along the outside (epi-) or inside (hypo-) of another fixed circle. Mathematicians have previously formulated the equations for epicycloidal and hypocycloidal curves, and these can be located, for instance, in Weisstein (2023a) and Weisstein (2023b).

Overall Parametric Equations For Any Number of Lobes

The parametric equations for the lobe pump are given by the following epi- and hypo-cycloid equations:

$$x_{\text{epi}}(t) = r((k+1)\cos(t) - \cos((k+1)t)) \tag{2.3}$$

$$y_{\text{epi}}(t) = r((k+1)\sin(t) - \sin((k+1)t)) \tag{2.4}$$

$$x_{\text{hyp}}(t) = r((k-1)\cos(t) + \cos((k-1)t)) \tag{2.5}$$

$$y_{\text{hyp}}(t) = r((k-1)\sin(t) - \sin((k-1)t)) \tag{2.6}$$

Where:

t is the parameter (angle of rotation),
$k = 2m$ is the number of cusps,
m is the number of lobes,
r is the radius of the rolling circle.

While $R = kr$, where R represents the radius of the fixed circle around which the smaller circle rolls, the enclosed areas for a hypocycloid and an epicycloid are given by:

$$A_{\text{epi}} = \frac{(k+1)(k+2)}{k^2}\pi R^2 = (k+1)(k+2)\pi r^2 \tag{2.7}$$

$$A_{\text{hyp}} = \frac{(k-1)(k-2)}{k^2}\pi R^2 = (k-1)(k-2)\pi r^2 \tag{2.8}$$

The cross-sectional area of a lobe pump with cycloidal profile is then calculated.

$$A_r = \frac{A_{\text{epi}} + A_{\text{hyp}}}{2} \tag{2.9}$$

2.3.1 Parametric Equations for a Three-Lobe Pump

A three-lobe pump, $m = 3$, therefore presents 6 cusps ($k = 6$), being three hypocycloidal cusps and three other epicycloidal cusps. Substituting k in the previous equations, we can obtain the parametric equations for a three-lobe pump with cycloidal profiles as follows:

$$x_{\text{epi}}(t) = r(7\cos(t) - \cos(7t)) \tag{2.10}$$

$$y_{\text{epi}}(t) = r(7\sin(t) - \sin(7t)) \tag{2.11}$$

$$x_{\text{hip}}(t) = r(5\cos(t) + \cos(5t)) \tag{2.12}$$

$$y_{\text{hip}}(t) = r(5\sin(t) - \sin(5t)) \tag{2.13}$$

Here:

t is the parameter (angle of rotation),
r is the radius of the rolling circle.

If we draw a circle whose diameter coincides with the farthest point of the epicycloid, we have that:

$$r = \frac{D}{2(k+2)} \tag{2.14}$$

Where:

D is the rotor diameter.

Finally, the cross-section area of a three-lobe pump, $A_{\text{three-lobe}}$, is:

$$A_{r_{\text{three-lobe}}} = \frac{19\pi}{128} D^2 \approx 0.466330 D^2 \tag{2.15}$$

In this design, shown in Figure 2.4, the pitch diameter is equivalent to 75% of the rotor diameter, and the lowest point of the valley, represented by the hypocycloidal curve, is equivalent to 50% of the rotor diameter.

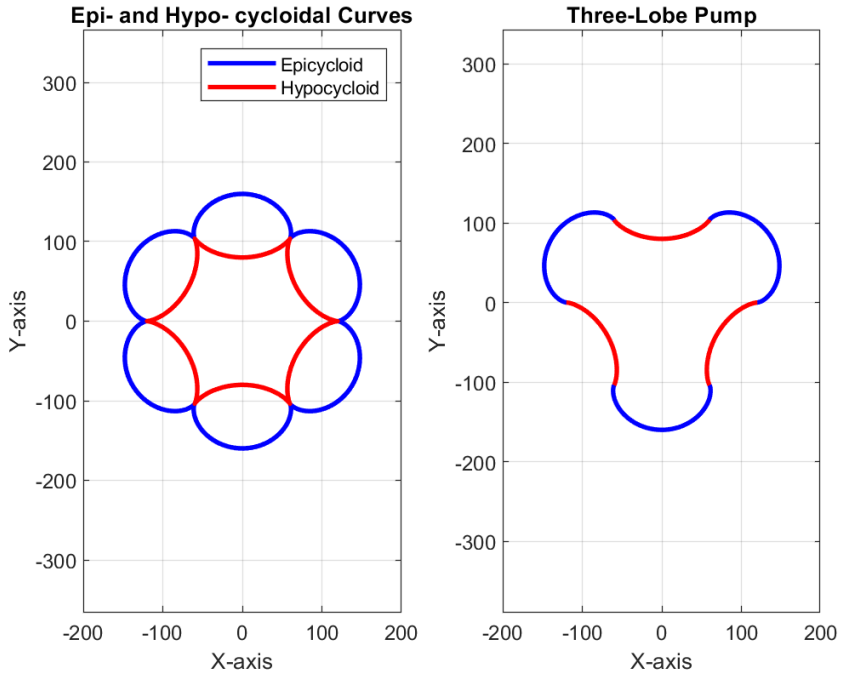

Figure 2.4: Cycloidal curves in a three-lobe pump

2.4 Operational Parameters Estimation in Lobe Pump and Turbine Systems

In hydraulic machines the fundamental formula for power (Eq. 2.1), can also be expressed as:

$$P = T\omega = \rho g H Q \eta = (\Delta p) Q \eta \tag{2.16}$$

Where, T is the torque, ω is the rotational speed, ρ is the fluid density, g is the gravity, H is the water head, Q is the volumetric flow rate, Δp is the pressure difference or net head, and η is the efficiency when the machine operates in turbine mode.

Therefore, the power required by a positive displacement unit is contingent solely upon the flow and the pressure difference. Notably, because of its intrinsic functioning where a fixed amount of fluid volume is subjected to displacement through its chambers, the flow rate in a PD pump is predominantly influenced by the rotational speed of the rotors (Macintyre, 1987).

In the context of a fixed design featuring two rotors with a diameter of D, a height of B, a head of H, and a rotational speed of n_s, we can estimate the maximum average flow rate, maximum average power, and maximum average torque for a

geometry with no gaps and efficiency of 100%. This estimation overlooks pulsation levels and neglects hydraulic losses attributed to the inherent presence of gaps. However, it offers valuable insights into the anticipated maximum values for a given set of parameters.

$$A_{rw} = \frac{\pi D^2}{4} - A_r \tag{2.17}$$

$$A_{rwc} = \frac{A_{rw}}{m} \tag{2.18}$$

$$Q = (A_{rwc} \cdot B) \cdot (m \cdot N_r) \cdot n_s \tag{2.19}$$

Here:

A_{rw} is the rotor total water area,
A_{rwc} is the area of one chamber,
B is the rotor height,
m is the number of lobes in a rotor,
N_r is the number of rotors,
n_s is the rotational speed in rps.

In Eq. 6, the terms inside parentheses correspond to the volume of fluid displaced by each rotor chamber, and the total number of cavities displaced in one turn. With this calculated Q, power can be deduced from Eq. 2.1, and the average torque T is calculated by:

$$T = \frac{P}{\omega} \tag{2.20}$$

CHAPTER

THREE

Experiments

The current section constitutes an integral part of a broader initiative to develop and scrutinize a positive displacement reversible pump-turbine. The primary objective of this work is to furnish validation data essential for the Computational Fluid Dynamics (CFD) analyses, forming the core of the task and fundamental for subsequent studies and design enhancements. Following validation, the CFD results complement and expand upon the experimental findings, enabling a comprehensive exploration of the entire flow field within the machine.

This experimental phase encompasses the design, fabrication, and assembly of the rig, inclusive of all experimental procedures, data preparation and cleanup, as well as post-processing and reporting activities. Notably, the experimental measurements were conducted by the Chalmers Laboratory of Fluid and Thermal Science as part of the ALPHEUS project to which the researcher belongs. While the design of the geometry and the rig were developed in collaboration between Chalmers and NTNU, Chalmers assumed responsibility for executing the experimental measurements and provided the researcher with the requisite data crucial for validating the CFD simulations.

The experimental measurements utilized the Particle Image Velocimetry (PIV) technique, involving a laser sheet illuminating particles within a specific flow plane. Velocity calculations were derived through consecutive high-resolution images capturing particle positions.

These measurements were carried out for three cases: two in pump mode, featuring different rotational speeds, and one in turbine mode. The PIV was synchronized with the lobe position, ensuring the acquisition of the instantaneous velocity distribution 100 times for a specific lobe position. Averaging these 100 samples produces the phase-averaged velocity distribution while calculating the standard deviation provides insight into areas where velocity components exhibit greater variation

from the average values. Following the completion of initial measurements for the full view, the entire procedure was replicated for more confined regions at the inlet and outlet of the machine, enhancing the resolution of experimental data in those specific areas.

The laser sheet's thinness is crucial for maintaining a clear measurement plane, typically capturing tangential velocity components. However, a stereo PIV methodology with two cameras was employed in one measured region, enabling the calculation of the velocity normal to the plane. While challenging and associated with increased uncertainty, these results are reported as supplementary data for CFD validation. Nevertheless, the flow within the examined PD RPT is predominantly two-dimensional, emphasizing velocity components in the designated PIV plane, making these components the most relevant.

The results discussed here relate to the mid-height section of the PD RPT. Although the researcher did not oversee the experimental rig's construction, requirements such as the velocity range the machine should operate were suggested to the decision-making process regarding the rig's specifications. Additionally, the researcher spent a week at Chalmers, gaining insights into the rig's operation. This detailed experimental dataset is pivotal in validating the CFD simulations integral to the ALPHEUS project.

3.1 Geometry and Experimental Set-Up

Figure 3.1 displays the CAD geometry of the measurement section, providing detailed dimensions. Cycloid parametric equations determine the lobe shape. Clearances between the rotor lobes and the top and bottom lids are approximately 0.5-1mm, established by a thin seal between these lids and the side walls. While the final design for PIV measurements shown in Figure 3.1 includes two diffusers in the design, the first set of experiments was carried out without those features, and measurements for flow rate and pressure difference were gathered. The design of the inlet and outlet diffusers aims to achieve a more uniform velocity distribution for PIV measurements. While ideally, the outlet diffuser should mirror the design of the inlet diffuser, the need for optical access for the PIV laser sheet influenced the current design.

The test rig operates as a closed-loop system, illustrated in Figure 3.2 and Figure 3.3. Water circulates from the bottom outlet of the test section, through an external pump, a control valve, a flow meter, and back to the test section's inlet. In turbine mode, the external pump propels the flow through the test section, while in pump mode, the pump is inactive. The control valve regulates the required head in pump mode and remains inactive in turbine mode. The runner lobes, driven by a motor and a gearbox connecting the rotation of the two rotors, rotate at precisely the same speed but in opposite directions. An RPM sensor monitors the rotational

speed. Due to the test rig's small size, losses in the gearbox and seals prevent the runner lobes from rotating in turbine mode, irrespective of head and flow rate. Consequently, the motor is used in turbine mode to overcome these losses, but with no impact on the PIV measurement results. The PIV outcomes provide velocity distributions under the experimental conditions established.

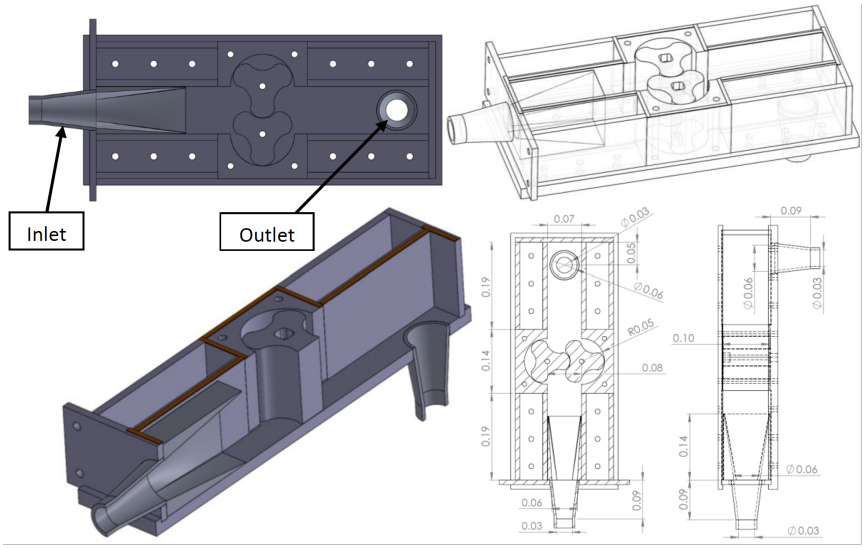

Figure 3.1: CAD geometry. Dimensions in meters. (Nilsson and Chernoray, 2023b)

Figure 3.4 displays the inlet and outlet diffusers, crafted to achieve a more uniform flow distribution. Additionally, it illustrates the hoses for static pressure measurements, facilitating the determination of static pressure differences across the test section.

Figure 3.5 illustrates the stereo Particle Image Velocimetry (PIV) setup with a horizontal laser sheet at the mid-height of the measurement section, entering through the PIV lens on the left side of the images (refer to Figure 3.2). One camera (right) is positioned perpendicular to the measurement plane, while another camera (left), set at a 30° angle to the vertical axis (for outlet measurements), allows for 2D-2C (two-dimensional, two-component) measurements. For outlet measurements, both cameras together enable 2D-3C (two-dimensional, three-component) measurements. The cameras are 14-bit Imager Pro X 4 M with a 2048 × 2048 pixel sensor and 7.4 μm pixel dimensions. Equipped with 105 mm f/2.8 Sigma lenses and 570 nm low-pass filters, these cameras separate fluorescent particle emission from laser illumination. The EverGreen 200 dual-cavity Nd-YAG laser with a 532 nm wavelength and light-sheet forming optics generates a horizontal light sheet with a thickness of 2-3 mm for planar illumination. Tap water, exhibiting suffi-

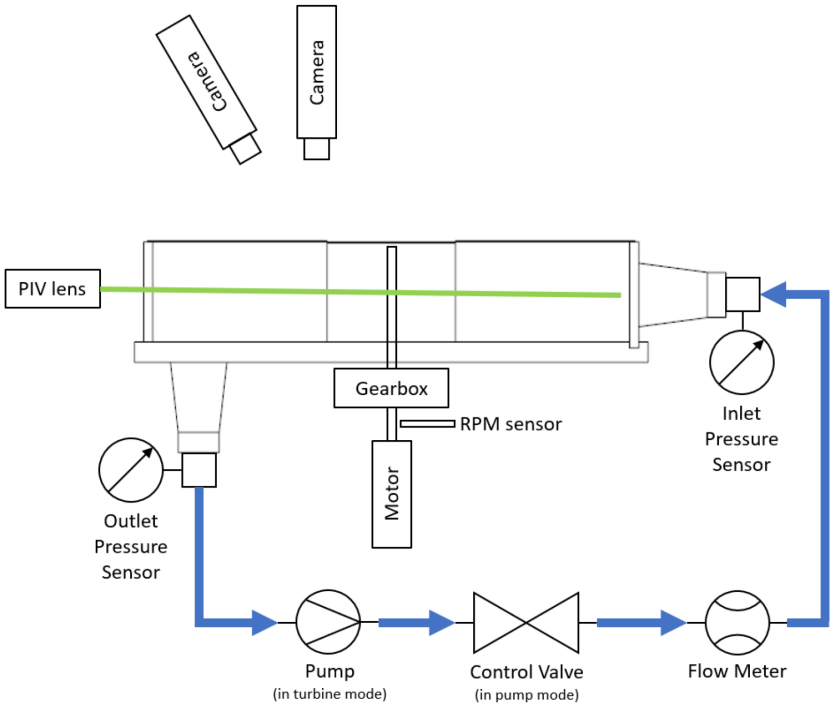

Figure 3.2: Sketch of rig components. Blue arrows show flow direction, same in both modes. PIV cameras set up for "Outlet" measurement. (Nilsson and Chernoray, 2023b)

cient index-matching with transparent polymethyl methacrylate (PMMA) materials, serves as the working fluid. The laser sheet penetrates the entire measurement section, including runner lobes, without refracting out of the measurement plane. Seeded with 20 μm fluorescent Rhodamine B-based polystyrene particles, the water facilitates fluorescent PIV, minimizing reflections from metallic rig components. In situ PIV calibration uses a 2-plane calibration target inside the water-filled rig.

The PIV system was synchronized with the rotor lobe rotation using a Hall effect sensor and a magnet on the motor shaft (see Figure 3.3. An illustration of a particle image from one of the cameras is provided in Figure 3.6. LaVision's Davis 10 PIV software facilitated the PIV processing, involving initial calibration with a calibration target, stereo self-calibration, stereoscopic reconstruction, cross-correlation, vector validation, vector statistics, and data masking. Velocity component statistics were obtained by phase-averaging 100 images. Cross-correlation utilized a multi-pass procedure with a decreasing window size. The initial window size was 64×64 pixels with 50% overlap, and the final pass used a 32×32 pixels area size with 75% overlap.

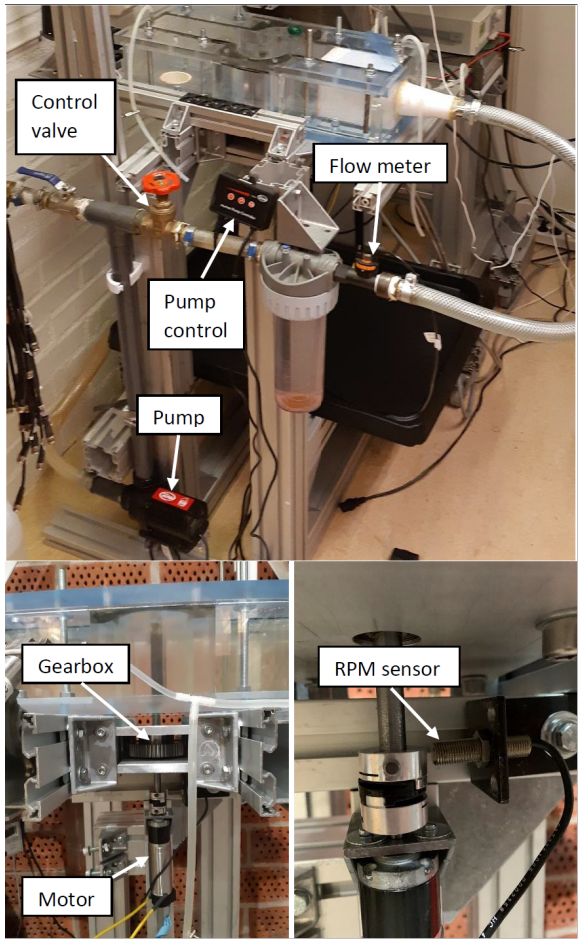

Figure 3.3: Photos of rig components. (Nilsson and Chernoray, 2023b)

Referring to Figure 3.5, it is essential to recognize that the perspective in the image may create the impression that the upper lobe extends beyond the channel, and parallax was calculated to provide accurate positioning comparison between PIV and CFD data, which is presented in Chapter 4. Also, PIV can only capture what is visible, and the lobes partially obstruct the flow, as evident in all the results, where portions of walls and rotors overlap each other. The upper lobe rotates clockwise, while the lower lobe rotates counterclockwise.

Table 3.1 provides overall details for the analyzed cases, including revolutions per minute (RPM), flow rate (in liters per minute (LPM) and m^3/s), and pressure difference. The total and static pressure differences are identical as the inlet and outlet pipes share the same cross-sectional area.

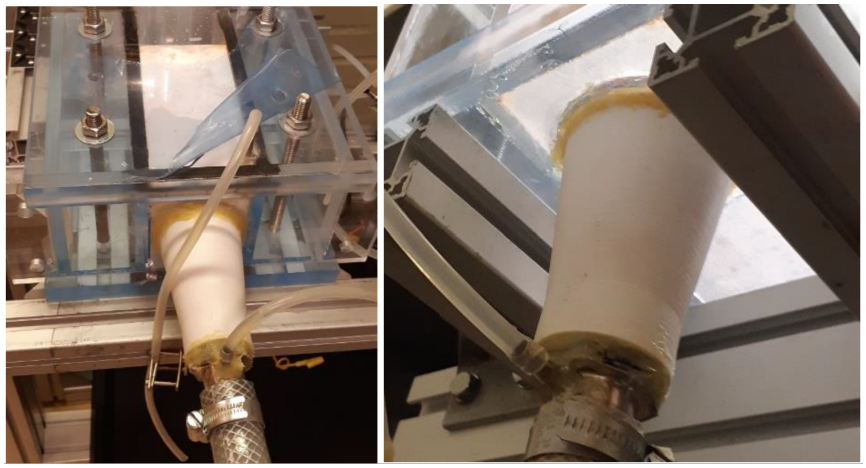

Figure 3.4: Inlet (left) and outlet (right) diffusers and static pressure measurement hoses. (Nilsson and Chernoray, 2023b)

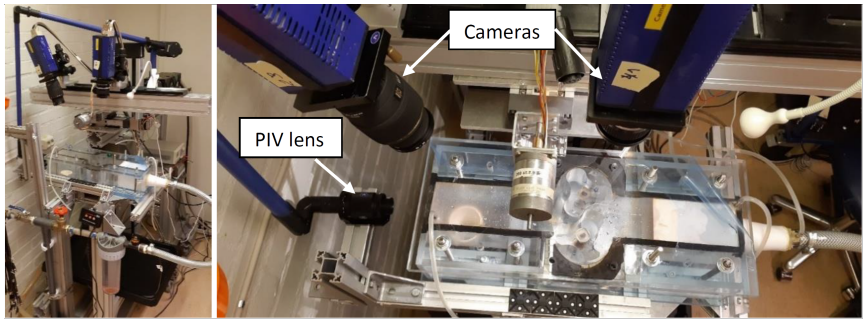

Figure 3.5: Two-camera stereo PIV set-up. (Nilsson and Chernoray, 2023b)

Table 3.1: Global details of investigated cases

Case	RPM	Flow (LPM)	Flow (m^3/s)	dP (Pa)	dP_{Total} (Pa)
Pump	45	11	1.83E-04	1058	1058
Pump	55	13	2.17E-04	1230	1230
Turbine	55	29.3	4.88E-04	-858	-858

To wrap up this section, pictures from PIV measurements will be shown alongside CFD results in Chapter 4 Section 4.3.

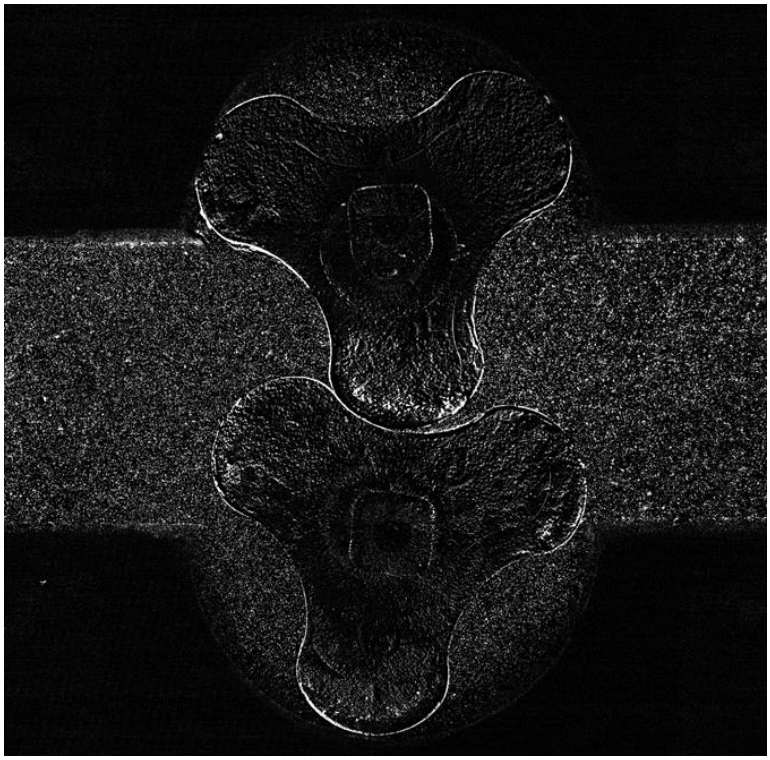

Figure 3.6: Example of particle image in PIV. (Nilsson and Chernoray, 2023b)

CHAPTER

FOUR

CFD Validation

Numerical models and computational fluid dynamic (CFD) simulations were developed based on the experimental scale model at Chalmers University of Technology.

The Immersed Boundary Method (IBM) was considered as a numerical approach to address the rotating components within the model. In IBM, a computational mesh overlays the domain, and the immersed boundaries (representing solid structures) are intentionally misaligned with the mesh. Instead, forces and effects from these boundaries are distributed onto the mesh through interpolation or other mathematical techniques (Roy et al., 2020).

IBM exhibits adaptability in managing moving and deforming boundaries, rendering it well-suited for simulations involving dynamic fluid-structure interactions. It excels in handling intricate geometries without the necessity for a conforming mesh, streamlining mesh generation by allowing immersed boundaries to be independently placed, potentially saving computational effort and time.

The flexibility of IBM in addressing complex geometries and dynamic boundary conditions proves advantageous in optimization studies where diverse shapes and variations must be considered. Its capability to accommodate changing geometries and moving boundaries is particularly beneficial for optimizing designs entailing fluid-structure interactions (Roy et al., 2020).

However, caution is warranted to address potential accuracy and stability issues, particularly in optimization studies where efficiency and precision are paramount. The interpolation or spreading techniques employed to transfer forces between immersed boundaries and the computational mesh can introduce errors, potentially impacting simulation accuracy. Additionally, IBM may incur additional computational costs due to interpolation requirements and the handling of non-conforming grids, making it computationally more demanding than methods utilizing structured

meshes. Achieving numerical stability can be challenging, especially when confronted with significant deformations or rapid changes in fluid-structure interactions.

To attain heightened accuracy and mitigate numerical instabilities, opting for controlled mesh deformation offers a viable alternative to the immersed boundary method. Such dynamic meshing involves continuously updating the mesh topology and grid resolution in response to changes in the position and shape of the structure, thereby accurately capturing the fluid-structure interactions (Kurokawa et al., 2008; Sonawat et al., 2020; Sonawat et al., 2021). This method is particularly useful for problems involving large structural deformations, such as in problems involving fluid-structure separation. However, generating a dynamic mesh can be computationally expensive and may require significant computational resources.

When addressing body rotation, it's noteworthy that mesh deformation introduces a grid velocity atop solved momentum equations, potentially escalating residuals and inducing simulation instability. Therefore, ensuring consistent and suitable cell skewness values for each time step is paramount to prevent solver crashes and maintain stability throughout the simulation. Hence, employing a user-defined function with external grids enables the necessary control over the mesh deformation process (Rane et al., 2017).

In conclusion, the choice between the two methods will depend on the specific fluid-structure interaction problem being modeled, and both methods have their own strengths and limitations. In general terms, dynamic mesh provides a higher accuracy to the CFD results, but the large mesh deformations can lead to the crash of the CFD solver more often, and the computational time might be higher than the IBM since the mesh needs to be generated for every time step of the transient simulation.

4.1 Immersed Boundary Method

In this study, the immersed boundary method may be sufficient, as it can effectively capture the fluid-structure interactions without needing a continuously updated mesh.

Within the recognized IBM implementations detailed by Verzicco (2023), ANSYS CFX, the chosen software for this work, employs the penalty method. This method treats the immersed body like a porous volume, generating a momentum loss inversely proportional to a solidity parameter. In other words, the penalty method is used to model the fluid-structure interaction by adding a penalty term to the fluid momentum equation, which penalizes the fluid velocity when it penetrates the structure.

As explained in *ANSYS CFX Reference Guide, Release 2020 R2, Fluid Structure Interaction*, the penalty term is proportional to the velocity of the fluid relative to the structure, and the proportionality constant is referred to as the penalty factor

(ANSYS, Inc., 2020).

Vande Voorde et al. (2004) describes the penalty method implementation as follows:

1. Discretization of the structure: The structure is represented by a set of Lagrangian markers, which are placed on the surface or inside the structure, depending on the desired level of detail.
2. Computation of relative velocity: The relative velocity between the fluid and the structure at each Lagrangian marker is computed as the difference between the fluid velocity and the velocity of the marker.
3. Application of the penalty force: The penalty force is added to the fluid momentum equation as a source term, proportional to the relative velocity and the penalty factor. This term enforces a no-slip boundary condition at the interface between the fluid and the structure.
4. Solution of the fluid equations: The fluid equations, including the penalty force, are solved using the finite volume method or another numerical scheme to obtain the fluid velocity, pressure, and other quantities of interest.
5. Update of the Lagrangian markers: The positions and velocities of the Lagrangian markers are updated based on the fluid velocity and the structural forces and moments, using a suitable coupling algorithm.

The choice of the penalty factor is a trade-off between accuracy and stability, and it depends on the specific problem and the desired level of detail. ANSYS CFX provides options for adjusting the penalty factor by applying a Momentum Source Scaling Factor (MSSF) to control the strength of the penalty force and for monitoring the solution behavior to ensure stability and accuracy. The MSSF value is typically chosen by trial and error based on the specific problem and the desired level of detail.

The equation for the penalty method in incompressible flows, which models the fluid-structure interaction by adding a penalty term to the fluid momentum equation, is given by:

$$\frac{\partial u}{\partial t} + u \cdot \nabla u = -\frac{\nabla p}{\rho} + \nu \nabla^2 u + f_{\text{penalty}} \tag{4.1}$$

Where ρ is the fluid density, u the fluid velocity, p the pressure, ν the fluid viscosity, and f_{penalty} the penalty term, which is proportional to the relative velocity between the fluid and the structure and the penalty factor, enforcing the no-slip boundary condition at the interface.

In ANSYS CFX, the penalty term can be written as:

$$f_{\text{penalty}} = -(MSSF \cdot C) \cdot (u_{\text{fluid}} - u_{\text{structure}}) \tag{4.2}$$

Where C comes from the coefficients in the momentum equation, $-(\text{MSSF} \cdot C)$ is the penalty factor, a constant determining the strength of the penalty force, u_{fluid} is the fluid velocity at the Lagrangian marker, and $u_{\text{structure}}$ is the velocity of the Lagrangian marker for the immersed body.

Numerical system can be stiff as the forcing term (and MSSF value) becomes large, and it is more likely for the solver to fail (ANSYS, Inc., 2020).

In lobe pumps, fine mesh is needed to resolve the leakage and the solid boundary paths. Schiffer (2012) have found that 6 or 7 prisms between rotors and casing are enough to achieve a good convergence level for leakages, although accurate leakage prediction is unlikely with IBM approach.

4.1.1 Numerical Results for Immersed Boundary Method

During the exploratory phase of the experimental setup, the IBM configuration aligned with the geometry lacking diffusers, as detailed in Section 3.1 and derived from Figure 3.1. The diameter of the rotors was set to 100 cm, with all gaps, including side gaps, tip gaps, and rotor-rotor gaps, uniformly configured at 0.5 mm.

CFD simulations were conducted using ANSYS 2020 R2 and the CFX Solver. As previously detailed, the Momentum Source Scaling Factor (MSSF) in CFX serves as a representation of the penalty method within the immersed boundary approach. A higher MSSF value is anticipated to result in a closer alignment between fluid and solid body velocities, reducing errors. However, it also raises the risk of solver failure as the forcing term increases, leading to a stiff numerical system. Thus an initial low MSSF value of 10 was chosen.

Transient simulations were conducted, simulating single-phase water flow in isothermal conditions over a full rotor revolution. This approach proved effective in achieving stable pulsation and accurate average values. Moreover, adopting time steps equivalent to 1° of rotor rotation ensured numerical convergence. Furthermore, reducing the time step by half did not substantially alter average values (less than a 1% difference), showing negligible numerical gain when compared to the associated computational cost.

Building upon the insights from Schiffer (2012) on leakage prediction, an inflation layer comprising 10 prisms was generated to fill the gap between the rotors and the casing. Following ANSYS guidelines for IBM implementation, mesh refinement for the immersed body (rotors) only needs to accurately depict the surface profile of the lobe. An unstructured mesh with inflation layers generated approximately 917 thousand nodes and 2.3 million elements. Overall, mesh dependency tests did not show significant changes in results. Figure 4.1 shows the applied meshes.

The boundary conditions at the inlet and outlet were configured as 'Opening Pressure and Direction' in ANSYS CFX. The experimental pressure difference measurements were applied to the higher pressure side and added to the atmospheric pressure, serving as the reference pressure. The rotational speed of the

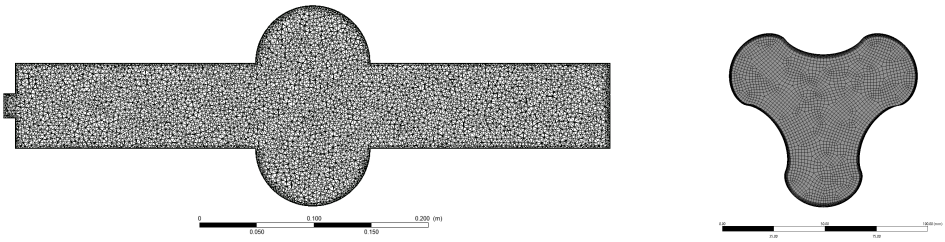

(a) Mesh for Fluid domain. **(b)** Solid domain

Figure 4.1: Meshes for (a) Fluid domain (stationary) and (b) Immersed solid domain (rotating). Cut view on the mid-plane.

rotors initiated at 30 rpm and increased in increments of 5 rpm up to 60 rpm. The walls were modeled with no-slip conditions, and the turbulence model was set to k-ω Shear Stress Transport (SST).

Figure 4.2 compares experimental data and numerical results with IBM configuration.

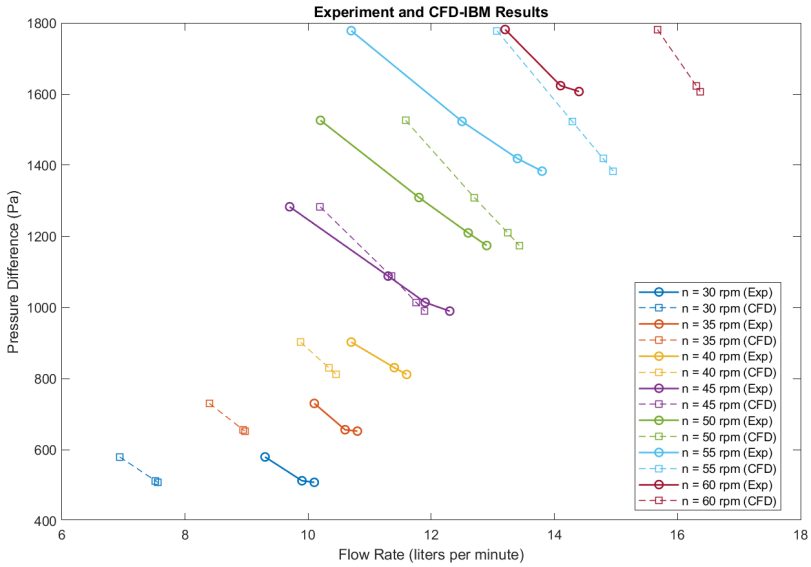

Figure 4.2: Comparison between experiment and CFD-IBM results.

In Figure 4.2, all data points remained within a 5% error margin at a rotation speed of 45 rpm. However, at 30 and 60 rpm, errors increased to around -25% and 25% respectively. Notably, the leakages, represented by the slopes of the experimental and numerical curves (also known as slip), within the same set exhibit

consistency, but the numerical slope is slightly higher, suggesting an underestimation of real leakages in the numerical simulations.

Several factors may contribute to the observed results. Increasing the Momentum Source Scaling Factor (MSSF) could potentially alleviate errors, as the Immersed Boundary Method may introduce unrealistic numerical leakage through immersed solid bodies. Additionally, implementing a more refined mesh along the rotor-rotor gap path can improve accuracy in capturing leakage between lobes. Another aspect to consider is the uncertainty surrounding the actual side gap value, which depends on a sensitivity study. The small scale of the experimental model is very sensitive to variations in geometry or operation conditions, even small ones like the change in the gap sizes due to assembly and manufacturing reasons. Kang et al. (2012) addressed the same difficulties in measuring data with smaller errors.

Despite various attempts to address the apparent lack of pattern in the numerical results, numerous efforts involving increased MSSF values, more refined meshes along the rotor-rotor gap path, and adjusted values for the side gaps still resulted in significant numerical instabilities, frequent solver crashes, and considerable uncertainties regarding leakage values. To better address the refinement level around the rotor-rotor gap, a mesh with 10 times more elements has been generated, but the computational cost was not justified when compared to a deformable mesh approach. Particularly at low rotation speeds, where leakage values constitute a substantial fraction of the total flow rate, this poses a significant challenge to any numerical validation endeavor.

In response to these challenges, a shift towards a deformable mesh approach has been introduced to replace the IBM approach.

Finally, attempts to operate the system in turbine mode involved using an external pump to induce a flow rate in the closed-loop rig (see Figure 3.2). However, due to the compact size of the test setup, mechanical losses in the gearbox and seals prevented the runner from rotating in turbine mode, regardless of the head and flow rate. Consequently, the motor had to be employed in turbine mode to overcome these losses, enabling the estimation of net hydraulic torque from the resultant pressure difference and flow rates. It is worth noting that adjustments were implemented only in the second set of experiments, coinciding with the introduction of diffusers and the PIV implementation.

This section resulted in a published paper, found in Appendix B.2.

4.2 Deformable Mesh

To mitigate numerical instabilities arising from mesh deformation and prevent solver crashes, as well as to achieve more precise leakage values through a deformable mesh approach — an aspect not feasible with the immersed boundary method — the commercial software TwinMesh emerged as a specialized solution tailored

for positive displacement machines and was seamlessly integrated into this study.

As documented by CFX Berlin (2024), TwinMesh is an advanced tool designed for the automated generation of high-quality hexahedral grids tailored for the moving components within rotary positive displacement machines. It facilitates structured mesh generation and CFD analysis setup for these machines. The resulting structured grids exhibit a balanced trade-off between reasonable transient CFD model size and optimal numerical quality.

The tool employs a fully automated interface for mesh generation, encompassing both 2D and 3D meshing processes. Input parameters, such as rotor and casing contours, are imported in a 2D cross-sectional format via IGES or CSV files. The contours can be conveniently scaled, enabling modifications, such as clearance adjustments between rotors and casing, with additional flexibility in adapting rotor positions. TwinMesh also automates the generation of interfaces between rotor meshes when required.

Following contour import, TwinMesh generates hexahedral meshes for user-defined rotation angles. Utilizing specialized smoothing algorithms, the software ensures adequate gap resolution, seamless transitions between varying gap sizes and chambers, and a homogeneous distribution of elements. After a quality check, especially for skewness values, the generated grids can be exported in 3D or 2D models.

Importantly, TwinMesh addresses the dynamic nature of rotating positive displacement machines by implementing mesh movement. Chambers and gaps within these machines undergo positional and shape changes during operation, impacting fluid flow. TwinMesh pre-generates numerical meshes for each rotational position, exporting node positions in a set of files. Using structured meshes, particularly hexahedral block-structured O-grid meshes, TwinMesh ensures consistent topology across rotational positions, eliminating the need for interpolation during transient simulations.

During runtime, the CFD solver, such as Ansys CFX, reads in these mesh files using special routines provided by TwinMesh. The deforming mesh approach incorporates the movement of mesh nodes as an additional term in the Navier-Stokes equations and other relevant partial differential equations. This approach avoids interpolation, significantly reducing numerical errors and simulation time. Ultimately, TwinMesh streamlines the CFD simulation process for rotary positive displacement machines, offering an efficient and accurate solution for complex fluid dynamics analyses.

4.2.1 Numerical Results and Validation with Deformable Meshing

New simulations were prepared to investigate and compare results for three operating conditions in the design with diffusers, depicted in Section 3 Figure 3.1. The primary design parameters encompassed the rotor diameter, established at

100 cm, tip gaps and rotor-rotor gaps were set to 0.5 mm, and side gaps were set to 1.0 mm. A subsequent sensitivity analysis focusing on the side gap size is recommended since it is expected to be between 0.5 and 1.0 mm.

Operating points are elaborated in Section 3 Table 3.1, with simulations adopting identical boundary conditions as those employed in the IBM simulations. These conditions encompass prescribed rotation speed and pressure difference values, employment of the same turbulence model (k-ω SST), and the application of no-slip walls. Transient simulations were prepared utilizing time steps corresponding to a rotation of 1° from the rotors. Time steps equivalent to 0.5° of rotation did not bring significant improvement in results.

The mesh was independently generated for the stator and rotating components, resulting in 2.2 million and 3.5 million elements, respectively. These components were then interconnected along their respective interfaces within ANSYS CFX. With TwinMesh, mesh quality indicators for the rotating parts outside the side gap region assessed minimum angle>30°, aspect ratio<10 for regions far from the gaps, and aspect ratio<120 for elements close to the gaps. For the side gap region, the mesh quality indicator had a minimum angle>16°, an aspect ratio<10 far from the shaft, and an aspect ratio<100 very close to the shaft. Mesh Inflation layer parameters for the stator walls were initially estimated and calculated using equations derived from the boundary layer theory. Figure 4.3 shows the generated meshes. The Y+ values were subsequently verified to ensure numerical quality indicators in the viscous sublayer.

The CFD results exhibited converged average values and a commendable numerical accuracy even before the rotor completed a full turn. In Figure 4.4, numerical stabilization is evident shortly after 50 iterations (equivalent to 50º of rotation in this simulation), revealing the characteristic periodic pulsation behavior typical of positive displacement machines. To ensure a valid comparison with PIV measurements and an accurate depiction of flow structures, the entering fluid needed to develop until it reached the rotor's position, which, in this case, occurred after approximately one full rotation of the rotors. Due to the periodic geometry, key average values such as flow rate are computed for every 120° of rotation for a three-lobe pump turbine.

From Figure 4.4, it is interesting to observe that a full turn of a three-lobe machine results in 6 strokes, with flow wave pulsations occurring every 60º of rotation. Both power and the maximum and minimum pressure curves also exhibit pulsations every 60º. In contrast, the torque curves require 120º of rotation to repeat the wave signal pattern.

The maximum flow rate occurs when a lobe aligns with the direction of the channel, while the minimum flow value occurs when it is phased by 30º from that position. Notably, the total power peaks slightly before the flow rate achieves its

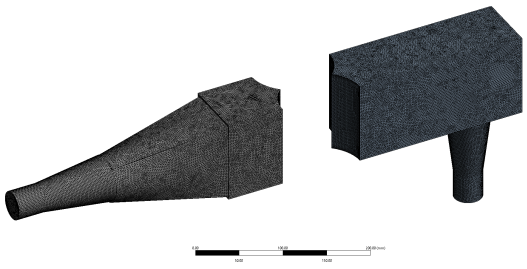

(a) Full view of stators mesh.

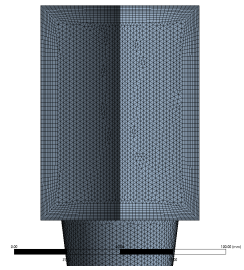

(b) Meshing on the interface.

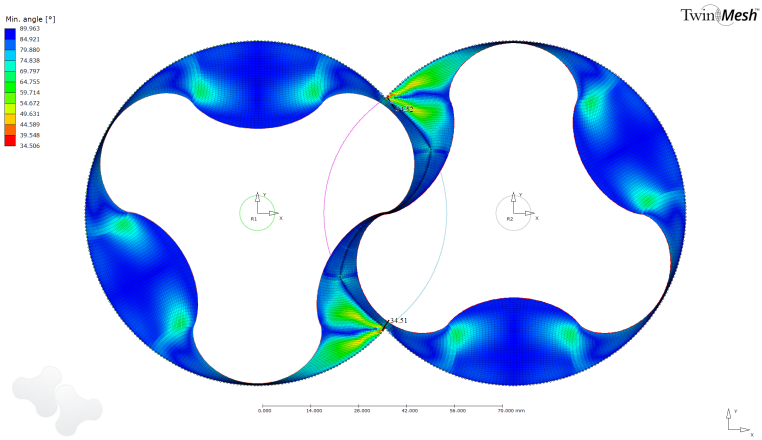

(c) Rotating domain with mesh quality index for skewness.

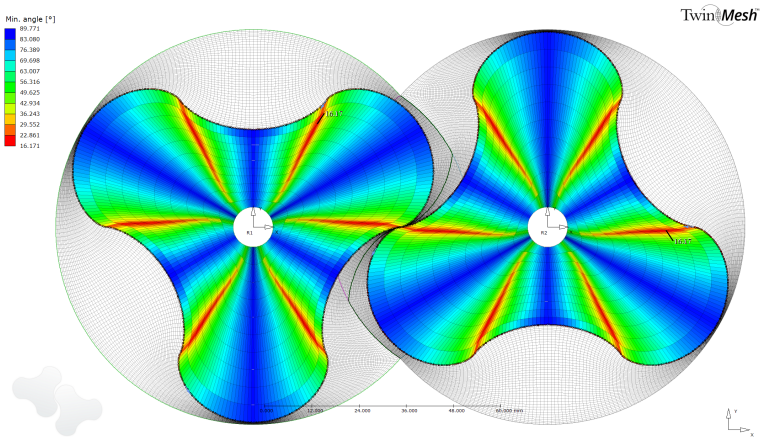

(d) Rotating domain in the side gaps with mesh quality index for skewness.

Figure 4.3: Meshes for stator domains (a and b) and rotating domains (c and d), created in ANSYS Meshing and TwinMesh, respectively.

maximum value. This peak coincides with when the pressures around the rotor-rotor gap reach their maximum and minimum values.

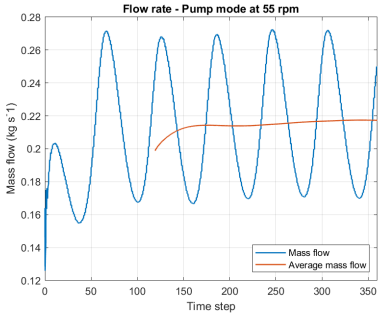

(a) Flow rate

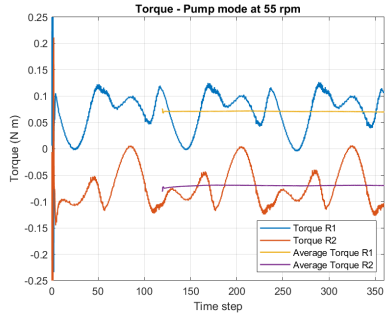

(b) Torques

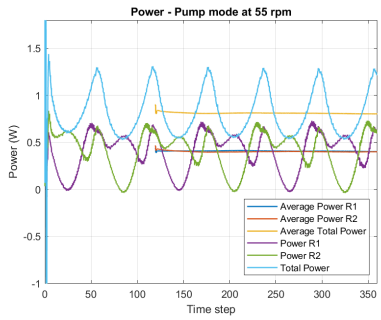

(c) Power

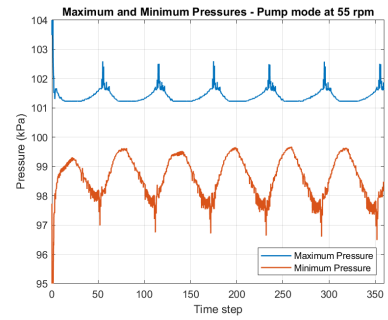

(d) Maximum and minimum pressures

Figure 4.4: Characteristic curves and pulsation behavior from 3D CFD simulations of a three-lobe pump running at 55 rpm and respectively average values.

Table 4.1 displays average flow rate values for the three examined cases. The CFD results diverge significantly from experimental values, exhibiting high errors. As previously mentioned, flow rate, among other parameters, is highly sensitive to small gap size variations, prompting the need for a sensitivity analysis.

In response, an additional model was generated for the pump mode case at 55 rpm, incorporating side gaps reduced to 0.5mm. In this iteration, the CFD results yielded a flow rate of 18.8 liters per minute, approximately 45% higher than the experimental value. Armed with the PD theory, which posits a linear relationship between flow rate and pressure difference with the slope representing leakages, a linear interpolation between flow rate values for 0.5 and 1.0 mm inferred an estimated actual side gap of 0.85 mm.

News simulations took place with the new side gap value for all three operating conditions and results are shown in Table 4.2.

Table 4.1: Comparison between flow rates in experiments and CFD with TwinMesh. Side gaps = 1.0 mm.

Mode	N (rpm)	$Q_{Exp}(LPM)$	$Q_{CFD}(LPM)$	Error
Pump	55	13	10.13	-22.1%
Pump	45	11	6.12	-44.4%
Turbine	45	29.3	41.66	+42.2%

Table 4.2: Comparison between flow rates in experiments and CFD with TwinMesh. Side gaps = 0.85 mm.

Mode	N (rpm)	$Q_{Exp}(LPM)$	$Q_{CFD}(LPM)$	Error
Pump	55	13	13.04	+0.3%
Pump	45	11	8.52	-22.6%
Turbine	45	29.3	40.35	+37.7%

Table 4.2 reveals a nearly negligible discrepancy between the CFD and experimental results in pump mode at 55 rpm. However, when the pump operates at 45 rpm, a significant error of approximately -22.6% is observed. This discrepancy suggests that an optimal side gap size might be around 0.70 mm. Notably, for both pump modes and rotational speeds, there is a noteworthy 21.8% improvement in both errors, supporting the idea of a linear relationship between flow rates and varying side gap values. Despite a subtle yet consequential deviation of 0.15 mm between the simulated pump mode with 0.85 mm side gaps and this alternative estimation, fine-tuning tip gaps and rotor-rotor gaps could potentially minimize errors towards zero. However, the turbine mode still exhibits a substantial error of 37.7%, showing only a marginal improvement of 4.5% compared to the previous case with a 1 mm side gap. Currently, a question mark hovers over the use of a motor to induce rotation speed, similar to pump mode but with torque dampened by the external pump used to simulate a turbine flow condition (see Chapter 3, Figure 3.2). Unknown deviations may have arisen from this combination, but a priori, the rotors should not discern whether the flow results from imposed torque or fluid forcing it to rotate. It may potentially be caused by imperfections in the experiments. There may for instance be a tiny difference in clearances for the two lobes, causing the flow to prefer a particular side, a concern raised by Nilsson and Chernoray (2023a). Even minor differences become critical when dealing with tiny gaps, especially in such a low rotation speed rig, potentially causing lobes from different rotors to touch and triggering widespread instabilities. These instabilities could adversely impact pressure readings, rotation speed control, and flow rate averaging values.

An intriguing comparison involves assessing experimental or numerical data against theoretical values for the maximum flow rate (Equations 6), maximum power output in turbine mode (Equations 2.16), and the maximum imposed torque in turbine mode (Equations 2.20). In the absence of gaps, machines operating at 45 rpm and 55 rpm would yield maximum flow rates of 28.72 and 35.10 liters per second, respectively, irrespective of being in pump or turbine mode. Contrasting with the values in Table 4.2, experimental values in pump mode at 45 rpm, pump mode at 55 rpm and turbine mode at 45 rpm represented 38.3%, 37.0% and 102.0% of the theoretical values. While the anticipated discrepancy arises from water being pushed back or upwards through the clearances in pump and turbine modes, the variations in magnitude compared to the theoretical value of 100% are notable. At 45 rpm, leakage values for pump mode constituted 63.0% of the theoretical value, whereas turbine mode contributed only an additional 2.0% to the flow rate. Given the more accurate and consistent assessment of pump mode through CFD results, the discrepancy arising from leakage direction, despite similar pressure difference levels albeit in opposite directions, raises concerns about the reliability of measured values in turbine mode. The significant discrepancy for turbine mode remains unexplained, and further PIV-CFD comparisons may shed light on the underlying factors.

These apparent tiny variations in gaps and adjustments arise from manufacturing tolerances and assembly processes, underscoring the heightened sensitivity of reversible lobe pumps at very low rotation speeds. In such cases, leakage values can constitute a significant fraction of the resulting flow rate. It is also crucial to emphasize that some uncertainties associated with the measured data remain unknown, as warned by Nilsson and Chernoray (2023a). Thus, inadvertent modifications in the experimental setup, such as possible lid adjustments, alignment of rotors and gearbox timing, tilting of the rig at varying degrees, or even occasional bubbles, might contribute to the measured discrepancies. Therefore, various unforeseen factors could influence the average flow rate and pressure difference values in the experiment, aspects that were not accounted for in the CFD simulations.

CFD simulations conducted under identical operating conditions but with two varying side gap values reveal distinct localized leakages near the side gaps. Despite this, the geometric projection remains precisely the same at the plane intersecting the middle height of the rotors. Consequently, the flow pattern and velocity profiles should closely resemble each other in the proximity of the rotating components and the mid-plane. The variations in leakage levels might only become influential and result in different flow velocity ranges when the volumes are considerably distant from the rotors. Therefore, comparisons between PIV data and CFD are deemed appropriate when examining regions near the mid-plane and the rotors. Such comparisons may even offer a reliable benchmark for assessing turbine mode.

4.3 PIV and CFD Velocity Field Comparison

Figures 4.5 to 4.13 depict the standard deviations in U- and V-velocity fields derived from PIV measurements (Nilsson and Chernoray, 2023b) along with a comparison between PIV and CFD velocity fields in the mid-plane. In all images, a positive U-component signifies a flow from left to right in all images, while a positive V-component indicates a flow from bottom to top. The sign of the velocity components, especially the V component, clearly indicates that the upper lobe rotates clockwise, and the lower lobe rotates counterclockwise. CFD data from the deformable meshing technique and side gaps of 0.85 mm have been exported and processed using MATLAB to match the PIV image format, and the corresponding code is available for verification in Appendix A.1. These visual representations allow for the examination and analysis of flow structures. As outlined in Chapter 3, the PIV process involved capturing 100 images to phase-average the velocity components, potentially incorporating some averaging effects from the 2-3 mm thickness of the horizontal light sheet. Moreover, PIV encounters challenges in achieving optimal resolution when two solid bodies are close. Consequently, there is an observable overlap between rotating and stator parts in the PIV images. Finally, the standard deviation figures for U- and V-velocity fields reveal significantly high deviations in velocities near the gaps due to the inherent jet structures that naturally occur in these narrow clearances.

Given the limited space available for the free flow of upstream current in the lobe machine, wherein it has minimal opportunity to bypass the rotors without interaction, the fluid is compelled to engage with the rotors or seep through the gaps. Particularly in pump mode, where the flow is driven by the imposed rotation speed of the rotors, the significance of the velocity field differs between the inlet and outlet.

In pump mode, the outlet velocity field holds greater importance due to its high dependence on the behavior of the rotors. In contrast, the inlet velocity field is less critical, as any unknown effects entering the system can be relatively overlooked at this stage. In our closed-loop rig, where an external motor had to impart additional torque for the turbine mode to function, the same analysis regarding inlet flow is applicable.

Hence, we have chosen to focus on the comparison between PIV and CFD results specifically close to the rotors' inlet, extending our analysis to trace the flow field to the farthest possible point in the outlet. The subsequent images of the standard deviation velocity field showcase a more expansive area around the inlet, highlighting the increased uncertainties in that region as compared to the outlet, particularly noticeable in turbine mode.

Figure 4.5 displays the U-velocity standard deviation for PIV measurements at three distinct rotational positions phased by 15°. It is evident that all gaps,

including tip and rotor-rotor gaps, exhibit substantial deviations for both U- and V-velocities, equaling or surpassing 0.25 m/s. Within the chambers, velocity fields also demonstrate notable deviation values, featuring extensive areas in light blue and green, representing deviations ranging from 0.1 m/s to 0.15 m/s.

An intriguing area appears at the inlet portion of the bottom lobe, characterized by a significant turquoise to green, and occasionally orange, zone with deviations commencing at 0.1 to 0.2 m/s. Deviations of at least 0.05 m/s permeate the entire studied domain, with smaller variations observed in the outlet. Notably, a subtle deviation in the streamline is discernible in the outlet, following the mid-height line. However this effect diminishes as it extends away from the rotors, often registering only 0.05 m/s, with specific areas occasionally exhibiting deviations around 0.1 m/s. These observations are crucial for the PIV-CFD comparison.

Figure 4.6 illustrates the U-velocity field at three distinct rotor positions, each with a 15° difference. Initially, the CFD results exhibit more vivid colors across all regions, yet upon careful evaluation, this aligns with the findings from the velocity field standard deviation analysis.

At the inlet (left side), higher velocity fields are evident in the upper part of both PIV and CFD images. This phenomenon results from the low-pressure zone generated by the rotors as the lobes move apart, directing the flow toward the rotor chambers. The red zone dominates the upper rotor chamber, indicative of this effect.

Moving to the upper rotor outlet, water continues to be expelled from the chambers, displaying positive velocity values. Notably, a blue area is observable slightly above the lower lobe in both PIV and CFD upper rotor images, denoting the lobe surface moving towards the inlet and exhibiting negative velocity values.

The outlet exhibits a wave pattern, indicative of the fluid being propelled upstream and the pulsating behavior evident in the CFD images. In the PIV images, a diagonal yellow trace overlays corresponding regions in the CFD results. Examining the standard deviations reveals comparable color patterns between the two sets of images.

Between the rotors, around the rotor-rotor gap, a light and dark blue areas signify backward leakage from the high-pressure side (outlet) to the lower-pressure side (inlet) in both PIV and CFD.

Tip gap leakages, visible only in the CFD due to resolution levels and no solid overlapping issues from PIV, also depict leakage from outlet to inlet. In the inlet side of the bottom rotor, PIV indicates a sizable near-zero velocity or backflow area before water is confined by the lower chamber. In contrast, CFD shows a smaller backflow area in the same region, with the mainstream positively advancing towards the rotor chamber. This discrepancy is attributed to the U-velocity deviation field, which demonstrates high uncertainty between 0.1 and 0.15 m/s in that area.

Observing the bottom CFD image, a larger green area forms as the lobe ap-

proaches the sharp edge. In the upper rotor of the upper image, a soft blue point signifies backflow in that mirrored position, representing the vestige of the backflow before the rotor chambers fully envelop water.

Finally, the velocities within the closed chamber in the lower rotor follow a consistent pattern in both PIV and CFD. A significant red portion indicates the flow continues to be propelled towards the outlet, and overlapping the U-velocity deviation field from PIV with its mean values reveals similar U-velocity magnitudes in the CFD images.

Figure 4.7 serves as a complement to Figure 4.6, displaying the V-velocity field. In regions distant from the rotating components, both PIV and CFD depict predominantly green areas, indicating near-zero velocities in the y-axis direction, while along the mid-line alternating red and blue zones depict the water strokes and pulsating pattern. Inside the chambers, the presence of red and blue areas is consistent, aligning with the rotational direction of the rotor in each zone of interest, where water is influenced to move upward or downward by the rotor's motion. The color representation within the gaps follows the same rationale explained in Figure 4.6, with all leakages directed from the high-pressure side (outlet) toward the low-pressure side (inlet). Again, the overlapping of PIV standard deviation values with its mean values reveals similar V-velocity magnitudes in the CFD images.

Moving on to the results for the pump mode at 45 rpm, Figure 4.9 and Figure 4.10 display U- and V-velocity patterns similar to those observed in the pump mode at 55 rpm, as shown in Figure 4.6 and Figure 4.7. Despite originating from different rotation speed scenarios, the only adjustment made is to the velocity magnitudes. The standard deviations of velocities for the pump mode at 45 rpm, illustrated in Figure 4.8, closely resemble the deviations observed in the pump mode at 55 rpm. Therefore, comparable conclusions can be drawn from all PIV and CFD figures for the pump mode at 45 rpm, and some superimposition with the standard deviation fields could provide insights into the variations in coloring.

Figures 4.11, 4.12, and 4.13 showcase the PIV and CFD velocity fields along with the standard deviation fields for the turbine mode at 45 rpm. Intriguingly, given that the experimental setup employed the same reference for flow direction (from left to right), many flow patterns closely resemble those observed in the other two pump modes in the preceding images.

Figure 4.11 displays the standard deviation fields, revealing a clear cyan-to-green zone along the top walls in the inlet. This signifies velocity deviations of up to 0.15 m/s, indicating a notably high level of uncertainty in that region. While the lower part of the image in the inlet is less pronounced than the upper section, it still exhibits significant deviations, reaching around 0.08 m/s. Within the chambers, light blue and cyan areas are visible, representing deviations ranging from 0.05 to 0.10 m/s. An important deviation is also observed around the rotor-rotor gap. In

the outlet, deviations reach up to approximately 0.08 m/s in U-velocities and up to 0.10 m/s in V-velocities. A distinctive cyan trace appears in the V-velocity field, originating from one of the lobes.

A notable distinction between turbine and pump modes lies in the opposite signs of pressure differences. In turbine mode, leakage in the tip gaps occurs downstream rather than upstream, and the flow passing through the tip gaps is observable from the left (inlet) to the right (outlet) side of the U-velocity images (Figure 4.12). In contrast, for this specific turbine case with very low-pressure difference (around 900 Pa), as lobes from different rotors converge in the outlet and move apart in the inlet, a sufficient high-pressure zone forms in the outlet, and a lower-pressure zone develops in the inlet near the rotor-rotor gap. This configuration leads to leakage against the flow in the upstream direction, evident in the blue and red zones surrounding that gap. Simulations further in this work showing much higher heads did not show such upstream leakage in turbine mode, but they also follow the downstream flow in the rotor-rotor gap.

A distinctive flow pattern in turbine mode is the wake formed along the central axis of all images in Figure 4.12, emerging just after the rotors on the outlet side and originating from the bottom lobe of the upper rotor. Both images illustrate a similar undulating red region surrounded by a thin yellow layer. However, the CFD image displays a larger area, possibly owing to the influence of the Reynolds-Averaged Navier–Stokes (RANS) turbulent model, which averages much of the numerical flow, thereby obscuring intricate structures in higher resolution, such as the Von Kármán vortex. Although RANS turbulent models provide quicker numerical solutions, crucial for future design optimization studies, they may lack intricate insights into flow structures.

It is noteworthy from the CFD results for U-velocities that this wake distinctly exhibits stronger velocities in the center and gradually smoothens out in the Y-direction. While a similar pattern is evident in the PIV images, the coloring is lighter. However, the deviation field in PIV also indicates a higher velocity deviation along the mid-line (light blue trace), potentially explaining the less pronounced wake observed in the averaged PIV images. We can also spot two dark blue areas along the outlet walls in the U-velocity CFD images, showing a stronger resistance for the faster flow rate provide by the turbine mode. Such areas are not easily visible from PIV, but a cyan coloring in those areas also shows the same negative U-velocity values.

U-velocities within the chambers exhibit similarities, but the CFD results display more vibrant colors, mirroring the observation made for simulated pump modes. Inlet velocities, however, are not comparable due to exceptionally high standard deviations in this region.

Finally, Figure 4.13 demonstrates the same behavior observed in other V-

velocity fields, where red and blue areas signify the direction of each rotor's rotation, though the CFD colors are slightly more pronounced and could be explained by the velocity deviation field. In the inlet, it's intriguing to observe the gradual reduction of the red area near the lobe from the upper rotor from the top to bottom images, indicating a shift in the generated wake direction. This shift has just produced a positive V-velocity phase (depicted by the red area) and will subsequently give way to a negative V-velocity pulse in the upcoming degrees of rotation. This phenomenon is evident in both PIV and CFD images, but the magnitude shown in the PIV is considerably smaller, resulting in much smaller pulse areas compared to the CFD, where a substantial red contour is visible.

In contrast to the average flow rate value obtained in the simulated turbine case with side gaps of 0.85 mm, which still exhibited a significant error of +37.7% and a discrepancy of 11 liters per minute in flow rate, the comparison of PIV and CFD velocity fields for turbine mode yielded comparable velocity levels. Beyond potential unknown factors that may have affected the experimental measurements, the higher U-velocities observed in the mid-line of the outlet, representing the wake after the rotors, could account for part of the discrepancy. Reasonably, small variations in volumetric flow are distributed along the z-axis of the rotor, making the differences less explicitly noticeable in the PIV-CFD comparison on the mid-height plane.

In conclusion, overall, CFD successfully replicated similar flow structures for both pump and turbine modes, suggesting the potential for further studies on design optimization and system characterization. However, considering that a genuine turbine mode could not function without the assistance of an external motor in a closed-loop rig, the development of an alternative rig with distinct water head levels in two separate reservoirs is essential to verify turbine mode operation.

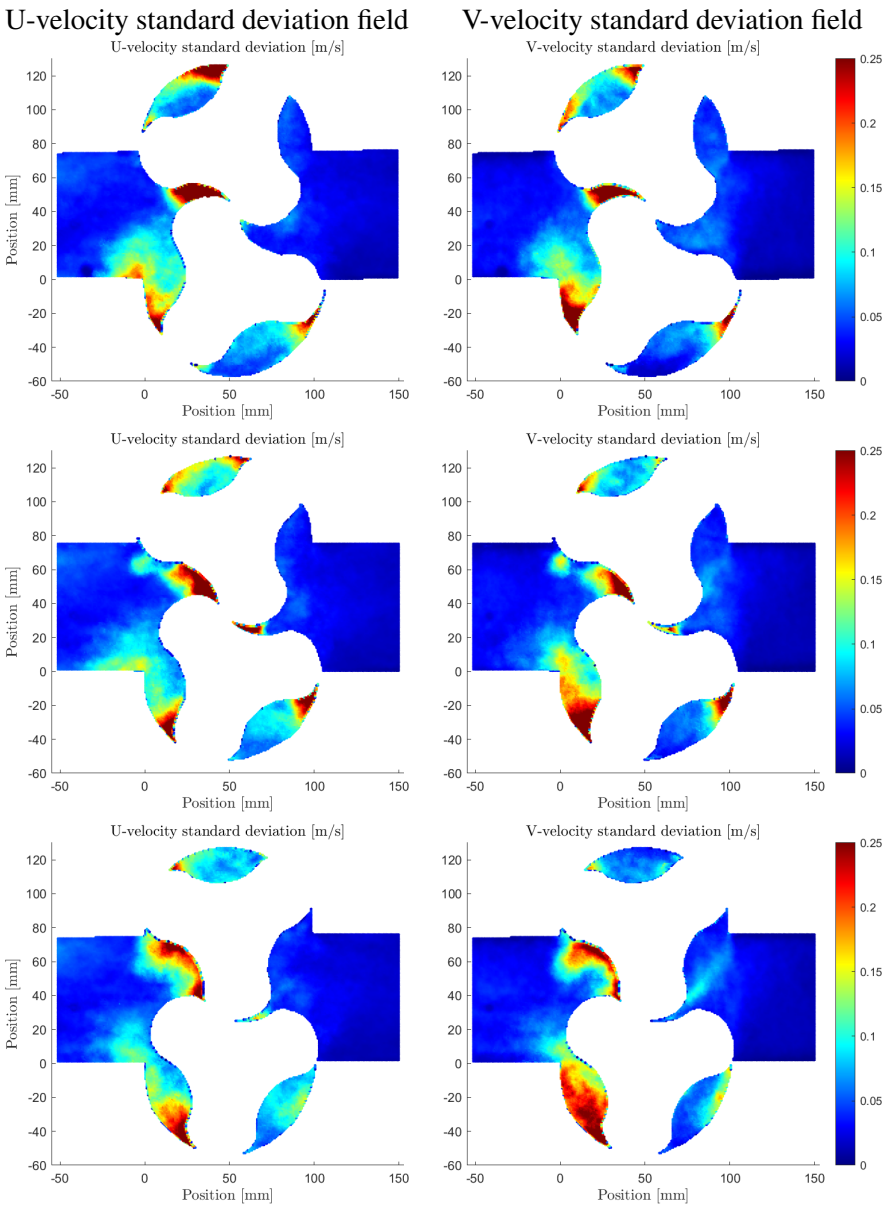

Figure 4.5: U and V-velocity standard deviation fields for PIV measurements in pump mode at 55 rpm. The rotor's position is depicted with a rotation phase of 15°, progressing from the top to the bottom figures.

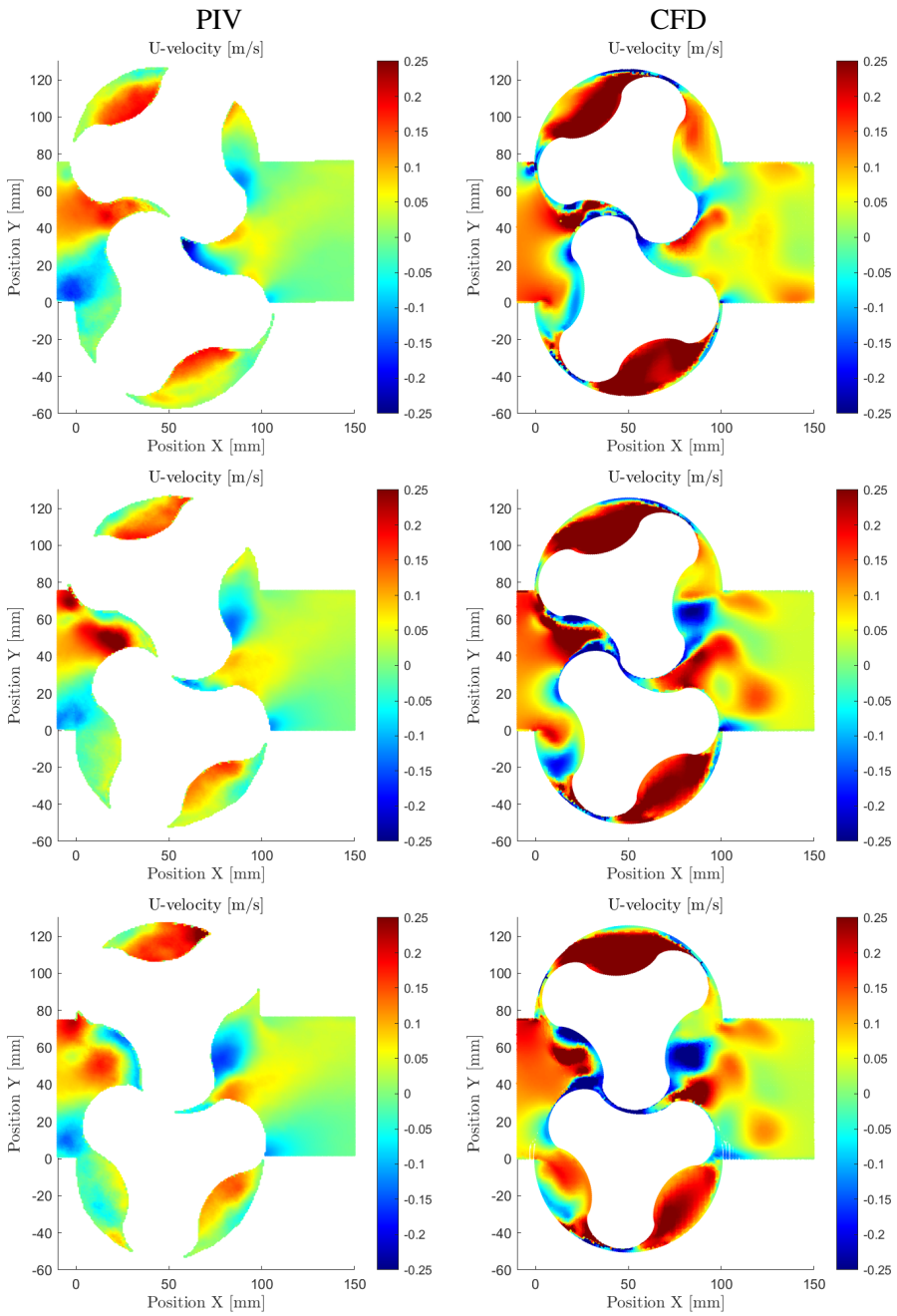

Figure 4.6: PIV and CFD U-velocities field for pump mode at 55 rpm. The rotor's position is depicted with a rotation phase of 15°, progressing from the top to the bottom figures.

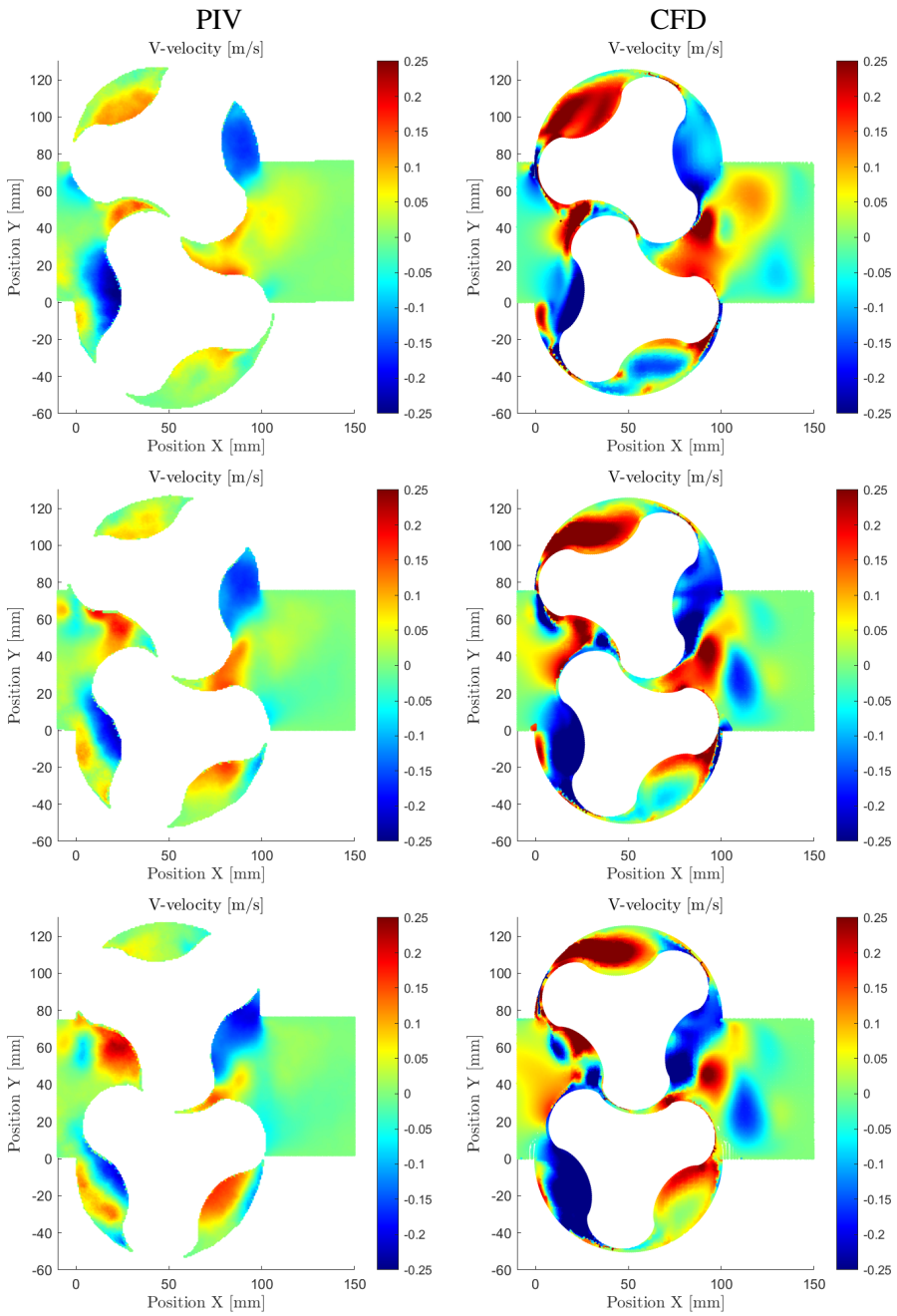

Figure 4.7: PIV and CFD V-velocities field for pump mode at 55 rpm. The rotor's position is depicted with a rotation phase of 15°, progressing from the top to the bottom figures.

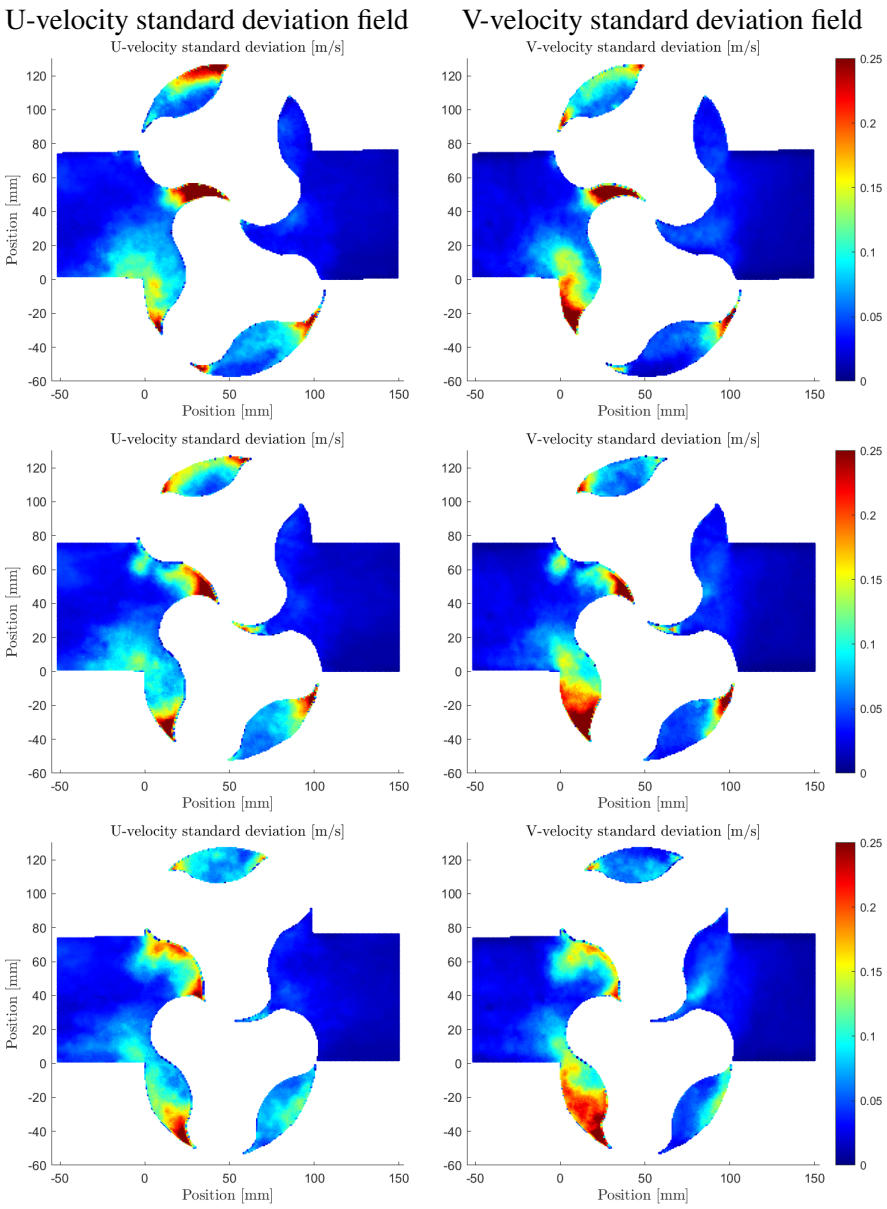

Figure 4.8: U and V-velocity standard deviation fields for PIV measurements in pump mode at 45 rpm. The rotor's position is depicted with a rotation phase of 15°, progressing from the top to the bottom figures.

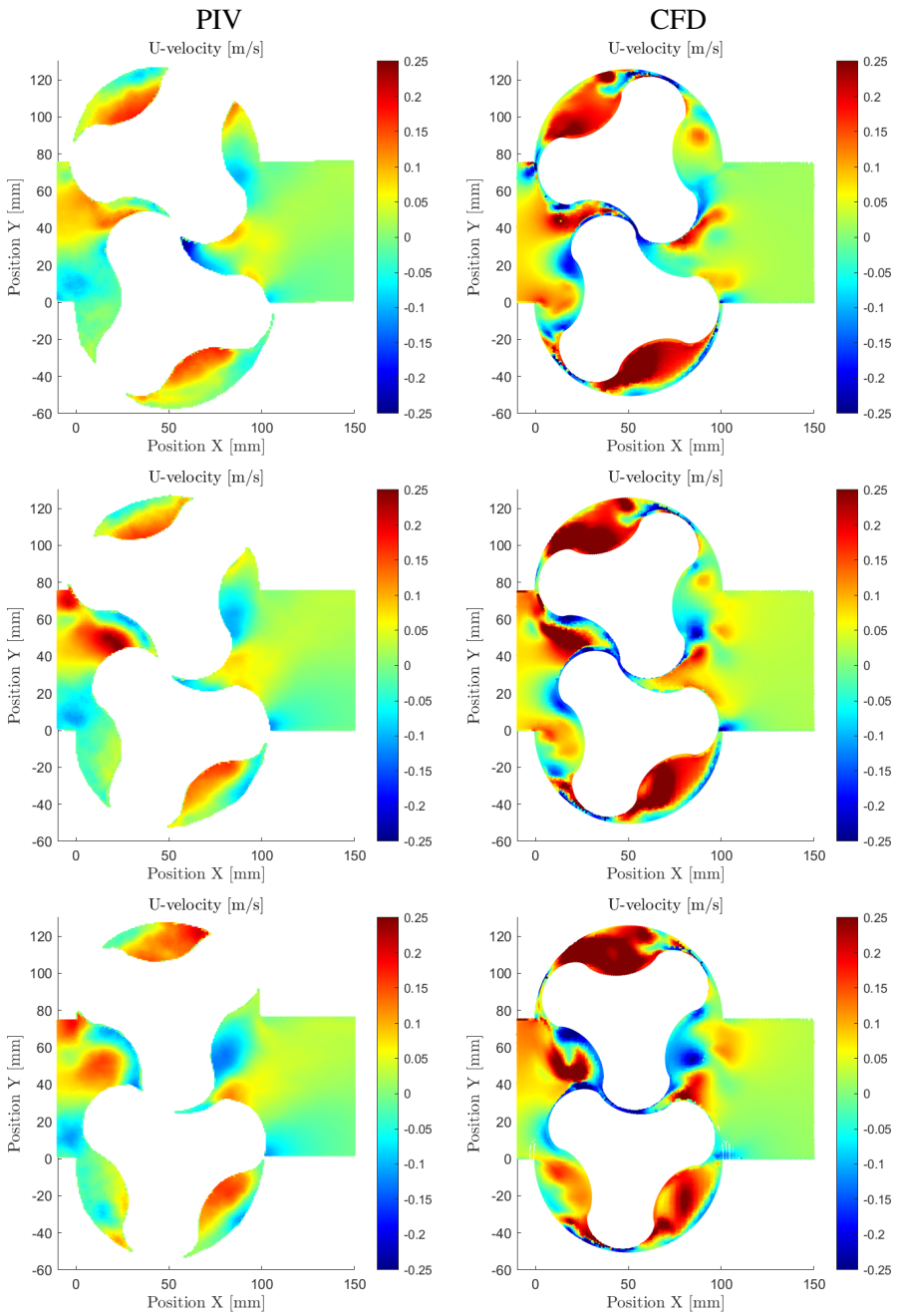

Figure 4.9: PIV and CFD U-velocities field for pump mode at 45 rpm. The rotor's position is depicted with a rotation phase of 15°, progressing from the top to the bottom figures.

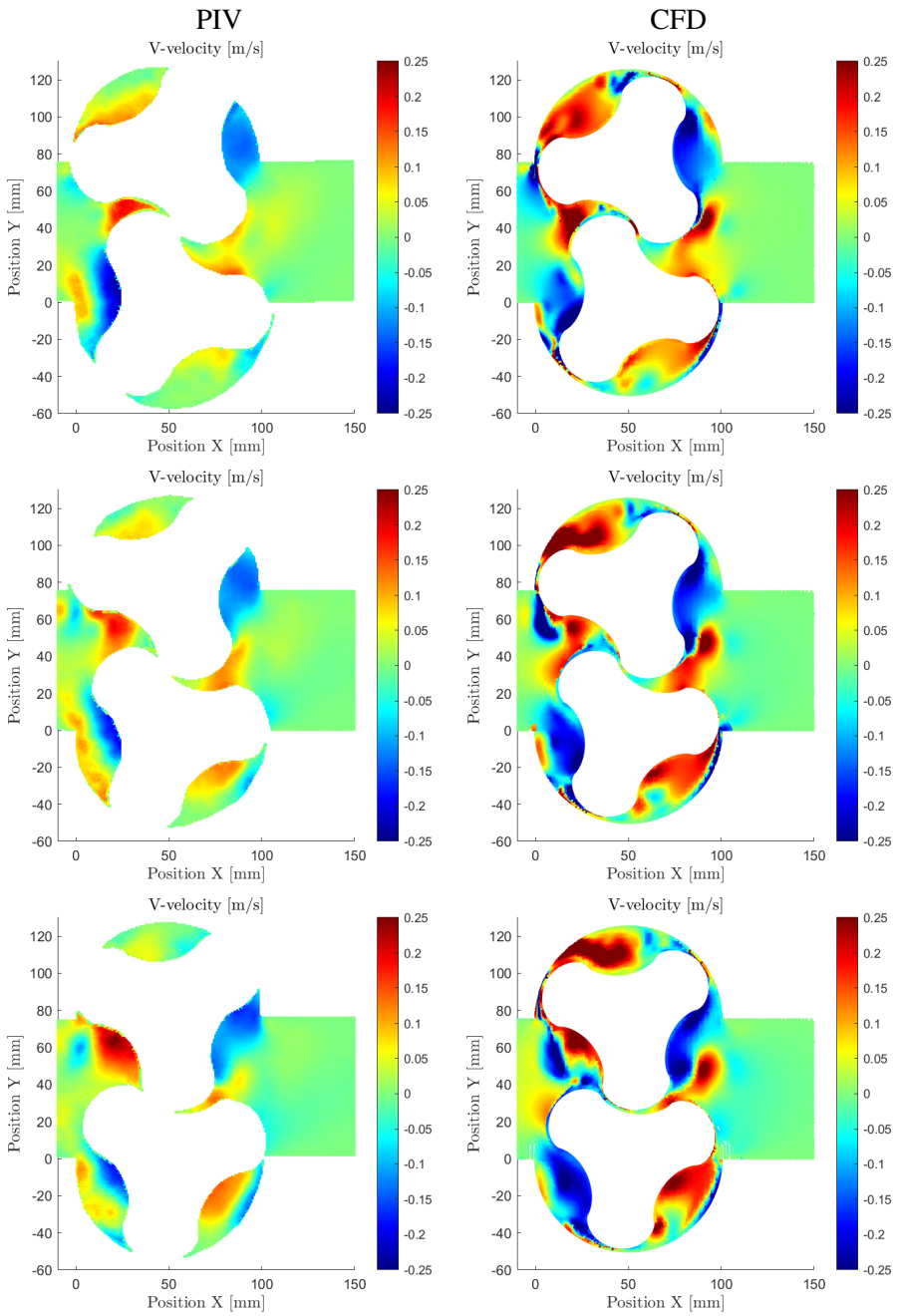

Figure 4.10: PIV and CFD V-velocities field for pump mode at 45 rpm. The rotor's position is depicted with a rotation phase of 15°, progressing from the top to the bottom figures.

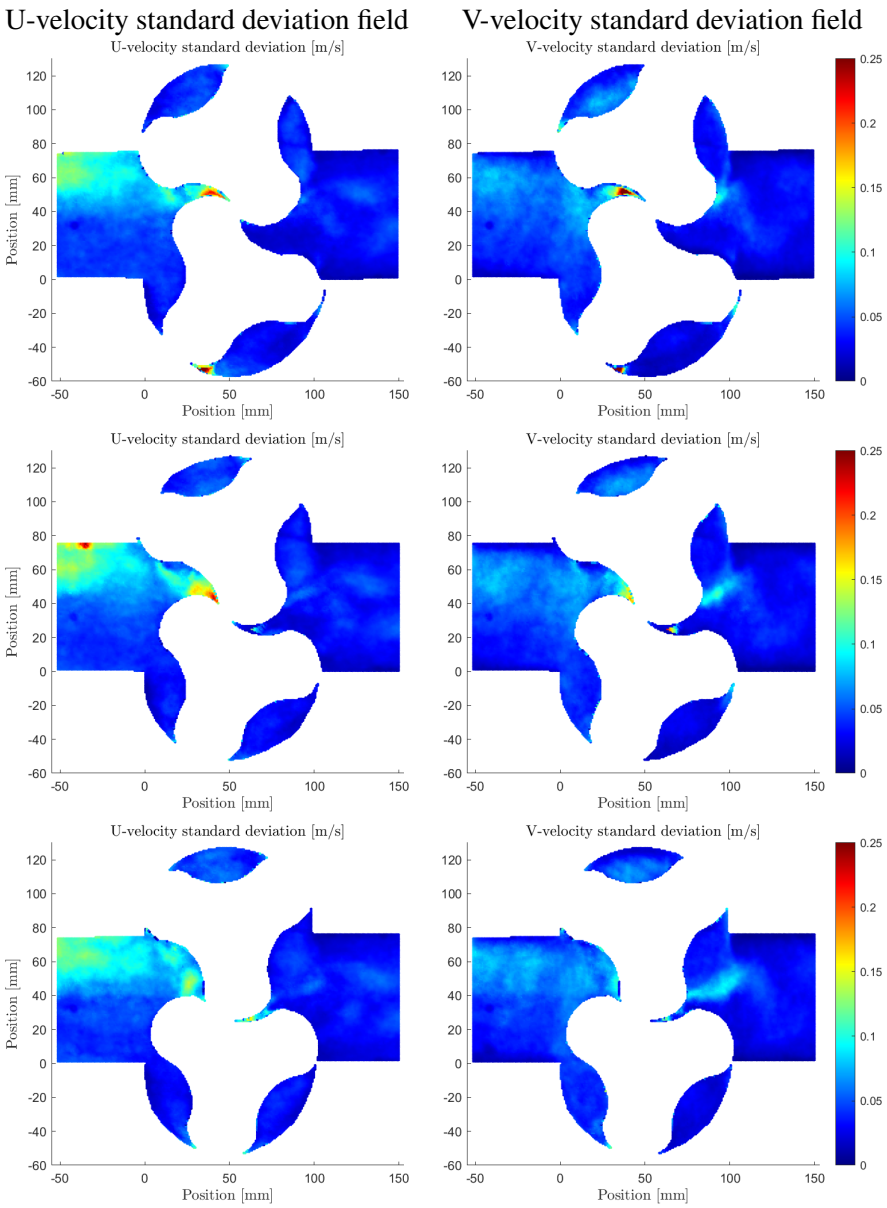

Figure 4.11: U and V-velocity standard deviation fields for PIV measurements in turbine mode at 45 rpm. The rotor's position is depicted with a rotation phase of 15°, progressing from the top to the bottom figures.

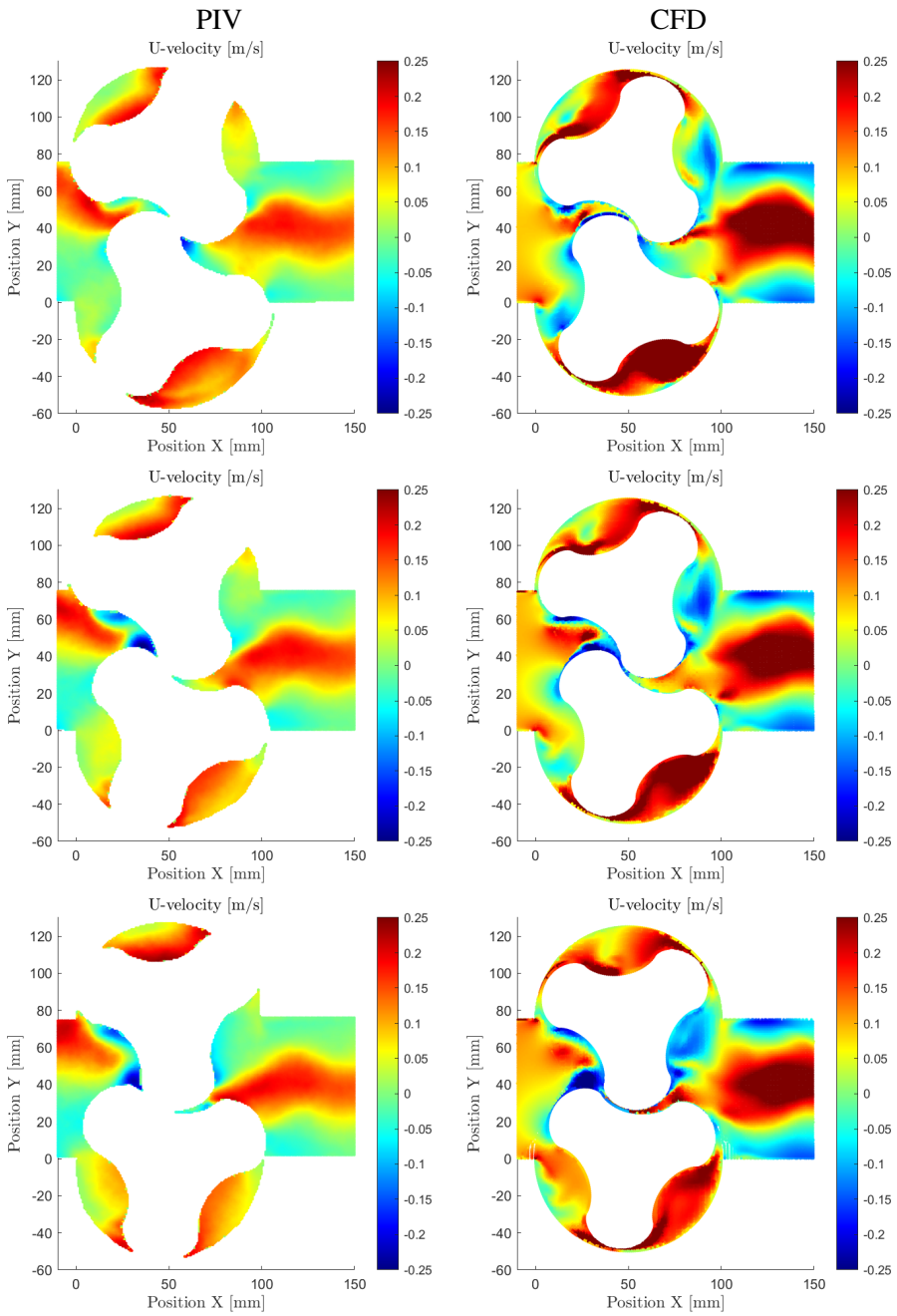

Figure 4.12: PIV and CFD U-velocities field for turbine mode at 45 rpm. The rotor's position is depicted with a rotation phase of 15°, progressing from the top to the bottom figures.

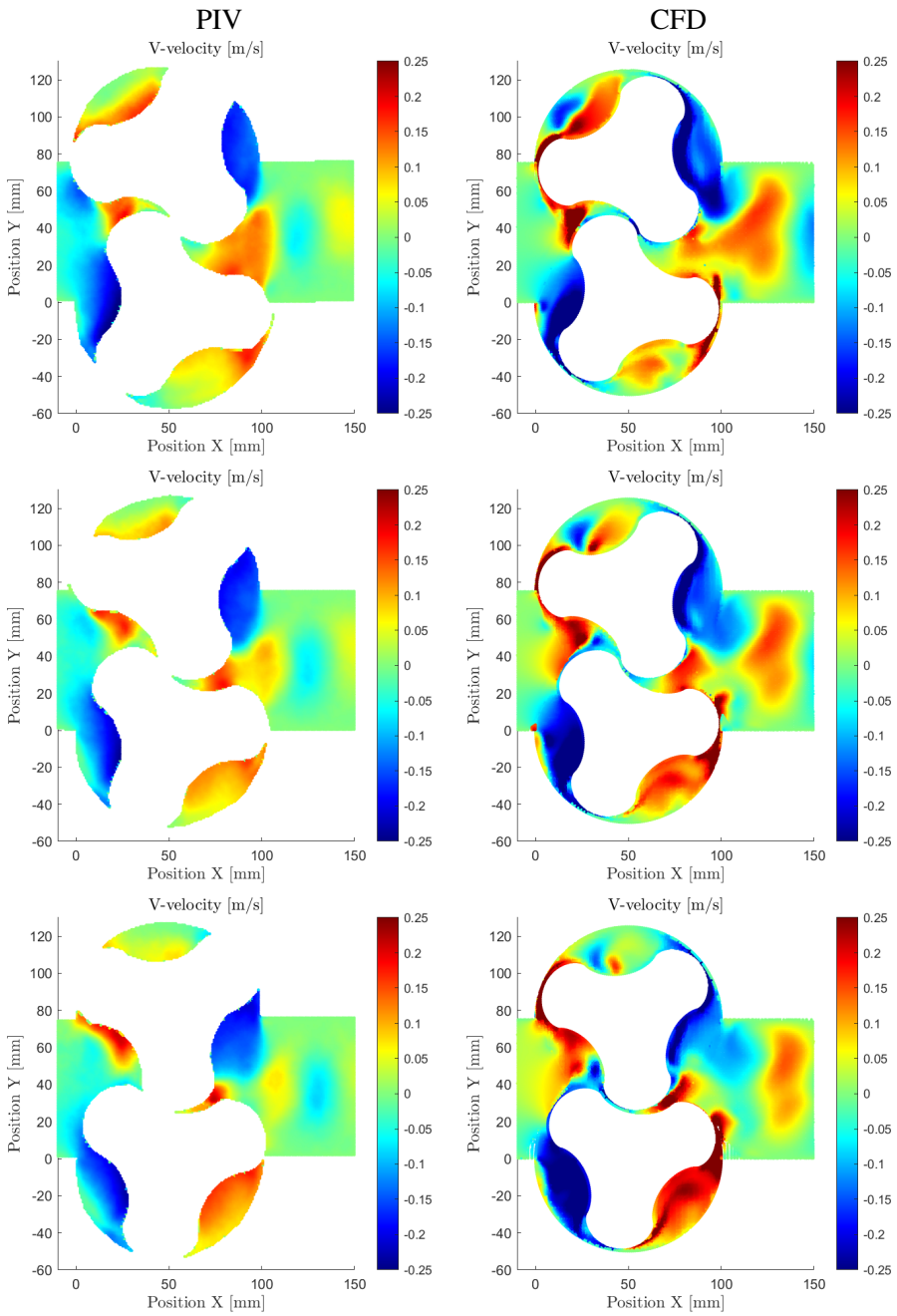

Figure 4.13: PIV and CFD V-velocities field for turbine mode at 45 rpm. The rotor's position is depicted with a rotation phase of 15°, progressing from the top to the bottom figures.

CHAPTER

FIVE

Parametric Design Optimization and Structural Analysis

This chapter delves into the intricate aspects of enhancing the efficiency of lobe pumps and lobe turbines by manipulating various design parameters. Employing parametric design optimization, we aim to unravel insights into elevating the efficiency of three-lobe pumps and turbines, thus complementing the discoveries presented in Section 2.2.

Recalling the noteworthy findings from Section 2.2, prior research has underscored the superiority of rotors with a cycloidal profile over their circular counterparts. Additionally, the consensus among researchers emphasizes the comparable performance of pumps or turbines featuring 3 or 4 lobes, both surpassing the efficiency in 2-lobe machines. Further nuances include the optimal rectangular shape for the inlet and outlet in lobe pumps, matching the rotors' height and mirroring the cross-sectional area equivalence to the preceding pipes. Minimizing clearances between rotating components and casings emerges as a crucial factor in promoting efficiency. While twisted rotors contribute to increased lifespan and mitigate cavitation and noise issues, they may entail a marginal sacrifice in efficiency.

Within this chapter, our focus extends to exploring specific parameters, such as the impact of clearances between rotors on efficiency and the relationship between efficiency and the width-rotor diameter ratio in different inlet and outlet channels. The discussion further encompasses additional design features considered potential avenues for augmenting performance. Integral to our analysis are fluid-structure interaction simulations, providing additional understanding of the intricate dynamics at play in these systems.

5.1 Inlet and Outlet Pipe Sizes Relative to Rotor Diameter

One lingering question persists beyond the scope of previously published work: Is there an optimal relationship between the sizes of the inlet and outlet pipes

when compared to the rotor diameter? In this investigation, we scrutinize the inlet width-rotor diameter ratio under the constraints of a fixed head and rotor rotation speed. Gaps are kept at a constant value. Figure 5.1 shows the studied parameters.

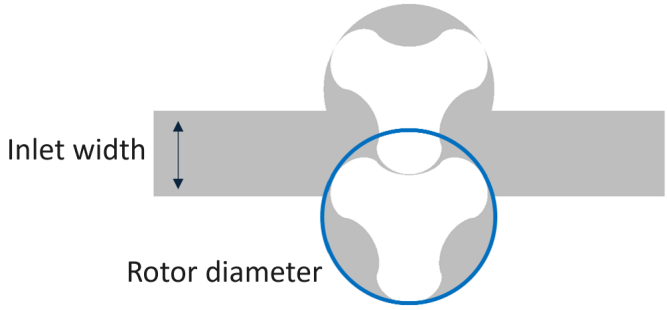

Figure 5.1: Inlet width – rotor diameter ratio scheme

As explored in Chapter 2, when considering straight rotors and a seamless transition of the pipe to the inlet or outlet, lobe machines can be analyzed bidimensionally, with the only notable exceptions being leakages occurring at the side gaps. This permits the simplification of fluid dynamics to a 2.5D simulation in ANSYS CFX, where the entire model is characterized by the height of a single finite volume, and symmetry may apply. Adopting this configuration, CFD simulations were prepared with a similar mesh strategy from Chapter 4 in turbine mode, a rotor diameter of 240 mm, a rotation speed of 400 rpm, and a pressure difference of 1 bar (equivalent to a 10.2 m water head), falling comfortably within the low-head range applied in the ALPHEUS project. The outcome of this optimization study is illustrated in Figure 5.2, depicting the resulting efficiency curve.

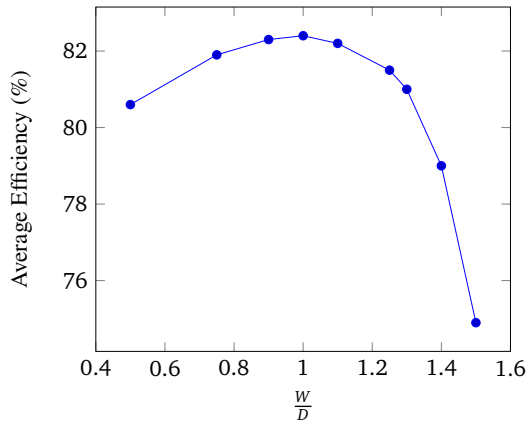

Figure 5.2: Turbine efficiency vs. Inlet width-rotor diameter ratio

Figure 5.2 illustrates that the optimal efficiency is achieved when the ratio of inlet length to rotor diameter equals 1. Additionally, the graph indicates that for ratio values below 1, the efficiency undergoes gradual changes, whereas, beyond this threshold, the efficiency experiences a substantial and more rapid decline. Beyond this threshold, the chambers no longer sustain the same level of sealing observed previously. Referring to the hydraulic power Equation 2.16, it can be deduced that the distribution of inlet pressure within these chambers leads to a reduction in the maximum torque generated, resulting in an overall decrease in efficiency.

We can observe this phenomenon in Figure 5.3, which illustrates the pressure distribution at the instant when the machine exhibits maximum efficiency. The inlet pressure, coming from the top, occupies all available open spaces, particularly within the chamber of the design with a W/D ratio of 1.25. In contrast, this phenomenon is not observed in the other two cases with W/D ratios of 0.5 and 1.0. In these cases, the upper chamber of the left rotor appears green, not red, as in the 1.25 design.

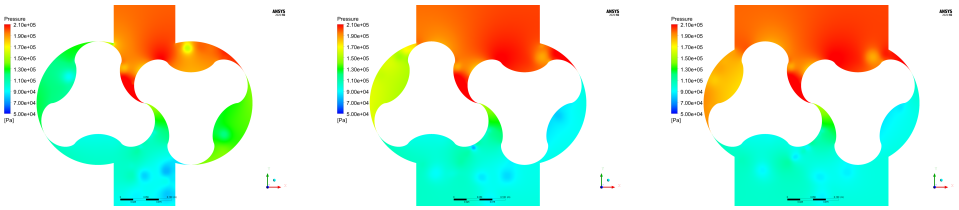

(a) W/D = 0.5 **(b)** W/D = 1.0 **(c)** W/D = 1.25

Figure 5.3: Pressure distribution near rotors across various designs with different W/D ratios.

In the design with a W/D ratio of 1.25, the pressure distribution implies a lower torque generation in turbine mode. This is evident in the upper lobe of the left rotor experiencing nearly equal pressure from both sides, leading to a diminished resulting force. In contrast, the other two cases, where the ratio modulates the pressure distribution, generate slightly different total torques without inducing a comparable equalizing effect on the upper lobe of the left rotor.

5.2 Clearance Sizes

Explored by Kang et al. (2012) and Phommacchanh et al. (2006), existing literature underscores the importance of minimizing gaps between rotors and casing (tip and side gaps) to optimize efficiency in lobe machines. However, an apparent gap in prior research pertains to the size of the rotor-rotor gap (g_{rr}). Does this particular gap align with the same conclusions drawn for other gaps, or do varying surface profiles and rotation speeds yield distinct outcomes?

Within the ALPHEUS project, our project advisor RONAMIC provided simulation data on a prototype scale with a rotor diameter of 2.4 m, assessing the impact of varying gap sizes between rotors on turbine efficiency. These CFD simulations, presented by van de Nes (2016), were conducted under the conditions of a 2 m water head and rotation speeds lower than 60 rpm. The gap sizes were manipulated by employing different lobe sizes derived from a circular profile, thereby altering the rotor diameter while maintaining a fixed center-to-center distance. Table 5.1 reveals that the prototype achieved a higher efficiency with a 20 mm gap. This suggested that an efficiency peak corresponds to an optimal rotor-rotor gap, and increasing the gap up to a particular value enhances turbine efficiency. However, it is crucial to emphasize that the design in question featured a rotor surface profile different from the one decided upon for this particular project. Therefore, further investigation is warranted to determine whether the observed efficiency peak with an increased rotor-rotor gap holds true for rotors based on a cycloidal profile.

Table 5.1: Effect of the gap size between rotors in turbine mode. Circular-based profile in prototype scale (van de Nes, 2016).

Gap size between rotors	Torque (Nm/m)	Power (W/m)	Mass Flow (kg/s/m)	Efficiency (%)
5	7,915	13,262	1,359	49.7
10	10,304	17,265	1,337	65.8
20	11,277	18,895	1,430	67.4

To confirm an optimal value for the rotor-rotor gap, 2.5D simulations were prepared for pump and turbine modes with a fixed pressure difference of 1 bar, rotors with a cycloidal profile, and an outer diameter of 240 mm, with tip gaps of 0.1 mm. Results for rotation speed of 400 rpm are presented in Figure 5.4.

Figure 5.4 shows that the smaller the rotor-rotor gap, the higher the retrieved efficiency in both pump and turbine modes.

The results presented by van de Nes (2016) differ from the simulation outcomes in this study, primarily due to variations in the applied methodologies. Firstly, distinct rotor profiles were employed: a cycloidal profile in this work instead of a circular design in van de Nes (2016). Secondly, this study kept the rotor diameter constant while van de Nes (2016) maintained a constant center-center distance as the fixed parameter.

Since a new machine will be built at TU Braunschweig to test turbine mode and check for overall efficiencies, another study should be implemented to analyze how big the rotor-rotor gap should be for the new rig. Figure 5.5 shows the efficiency curve for turbine mode when a cycloidal profile is used, rotor-rotor distance and tip gap are fixed, while rotor diameter and rotor-rotor distance vary.

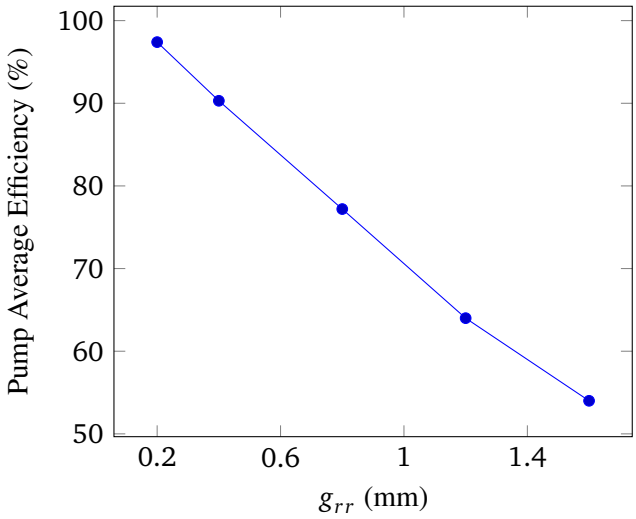

(a) Pump Efficiency vs. Rotor-Rotor Gap

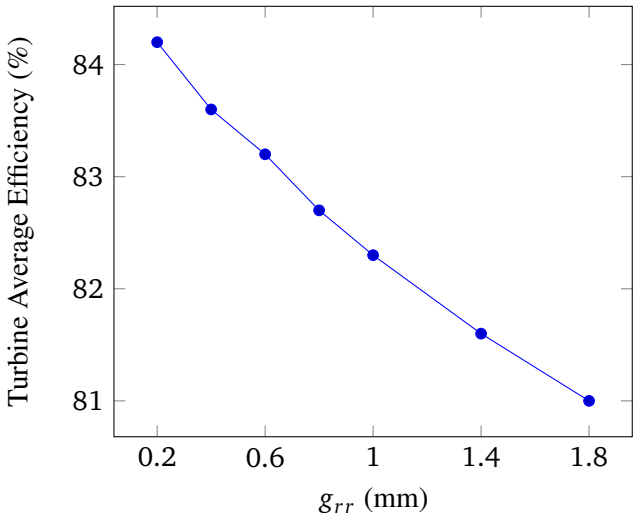

(b) Turbine Efficiency vs. Rotor-Rotor Gap

Figure 5.4: Average Efficiency curves for pump and turbine modes with constant tip gaps and rotor diameters, and varying rotor-rotor gaps.

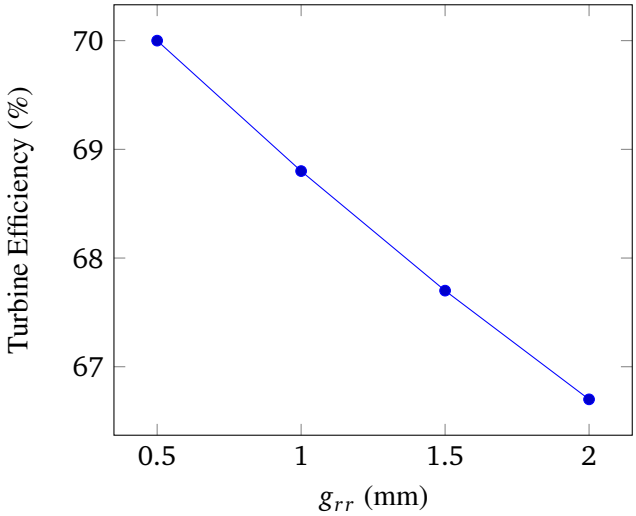

Figure 5.5: Turbine Efficiency vs. Rotor-Rotor Gap (mm) for rotors designed with cycloidal profile, constant tip gap and rotor-rotor distance, while varying the rotor diameter and rotor-rotor gap.

As shown in Figure 5.5, we can see that a smaller rotor-rotor gap also generates better efficiencies. Therefore, the differences between van de Nes (2016) and the recent findings should probably rely on the use of different rotor profiles. Here, rotors' cycloidal curves present a fixed rotor-rotor gap distance for every position in the rotation, while the circular-based profile presents a varying g_{rr} value, therefore producing jets with varying magnitudes that might affect the final efficiency.

5.3 Optimal Design for TU Braunschweig Rig

As explained in Chapter 3, turbine mode could not be run in our first model scale rig. Therefore, another PD RPT will be built at TU Braunschweig to establish a proof of concept regarding the conditions under which this machine could operate in turbine mode. The design process involved various construction decisions and design optimizations, guided by the conclusions from the previous topics in this section and the earlier sections.

The new design will feature two rotors with cycloidal surfaces, each having a diameter of 348.67 mm, a rotor height of 300 mm, tip and side gaps equal to 0.15 mm, and a rotor-rotor distance of 262.5 mm. A circular pipe with a diameter of 300 mm will transition in shape to a rectangular profile to match the rotors' height, and the inlet length is 235.62 mm.

Figure 5.6 below illustrates the designed concept.

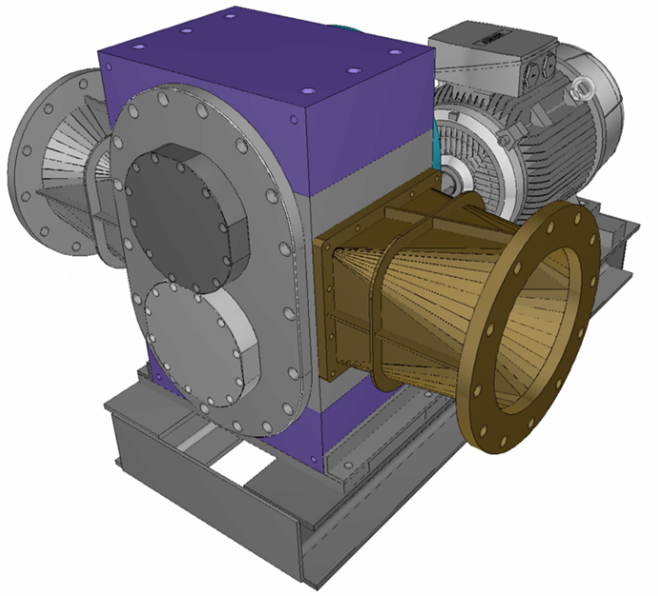

Figure 5.6: Designed concept for the new PD RPT in TU Braunschweig. [Image provided by DEMO and DELFT University of Technology, both project partners]

5.3.1 Mechanical Loads

By utilizing the designed PD RPT device for TU Braunschweig, a simplified one-way fluid-structure interaction (FSI) simulation was conducted to estimate the stresses and deformation magnitudes on the rotor. An aluminum alloy was chosen as the material reference.

Firstly, the pressure contour on the rotor's surface was obtained for the angular position that provided the maximum torque available (and therefore, the maximum applied force) in a complete turn of the rotors running in turbine mode when subjected to a net head of 7.8 m. This head represents the maximum physical head at TU Braunschweig, and it does not account for pressure drops regarding different velocity speeds in the pipelines. Thus, simulated mechanical loads would show overestimated values compared to the real case. Subsequently, a static structural analysis was prepared, including the rotational velocity and cylindrical support as constraints. The surface pressure calculated through Computational Fluid Dynamics was then assigned to the rotor's surface.

Figure 5.7 depicts Von-Mises stresses at 300 rpm with a water head of 7.8m, while Figure 5.8 shows total deformation for the same case. The maximum stress is near the shaft, and the highest deformation occurs at the lobe tips. Notably, the maximum stress is below 1 MPa, and the maximum deformation is under 1 μm. These values alleviate structural safety concerns, also ensuring that lobes from

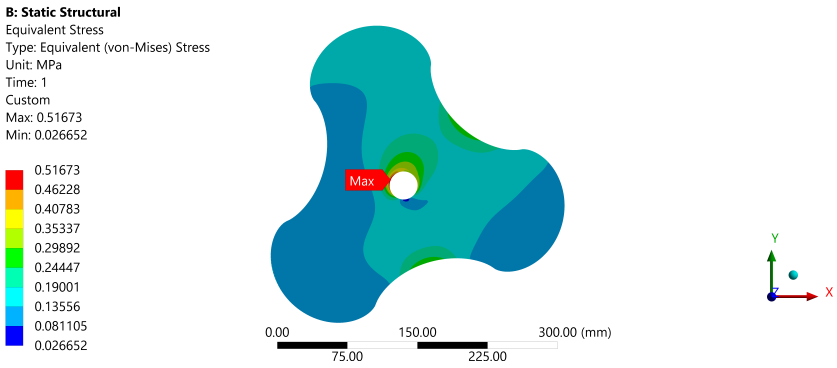

Figure 5.7: Maximum Von-Mises stresses presented in a full turn of a rotor running at 300 rpm in turbine mode, head of 7.8m.

different rotors do not come into contact during rotation. However, phenomena like cavitation and vibration loads, not considered in this study, warrant further investigation for a comprehensive assessment of the machine's lifespan.

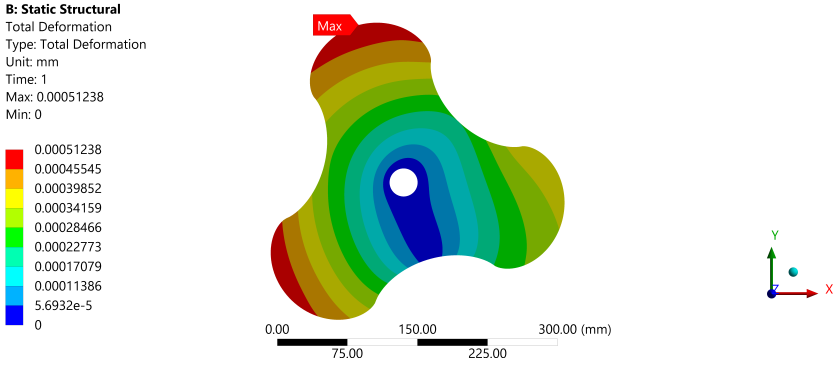

Figure 5.8: Maximum Total Deformation presented in a full turn of a rotor running at 300 rpm in turbine mode, head of 7.8m.

CHAPTER

SIX

Experiment Design of a Reversible Three-Lobe Pump

A new PD RPT is designed to feature two rotors with cycloidal surfaces, each having a diameter of 348.67 mm, a rotor height of 300 mm, tip and side gaps equal to 0.15 mm, gap between rotors g_{rr} of 0.5 mm, and a rotor-rotor distance of 262.5 mm. Although twisted rotors would induce fewer pulsations, straight lobes are promised to show a slightly bigger efficiency, as explained in Chapter 2 Section 2.2. Thus, straight rotors were chosen for this model. A circular pipe with a diameter of 300 mm will transition in shape to a rectangular profile to match the rotors' height and the inlet length of 235.62 mm. Figure 6.1 shows the schematic rig at TUB's facilities where the PD RPT will be installed.

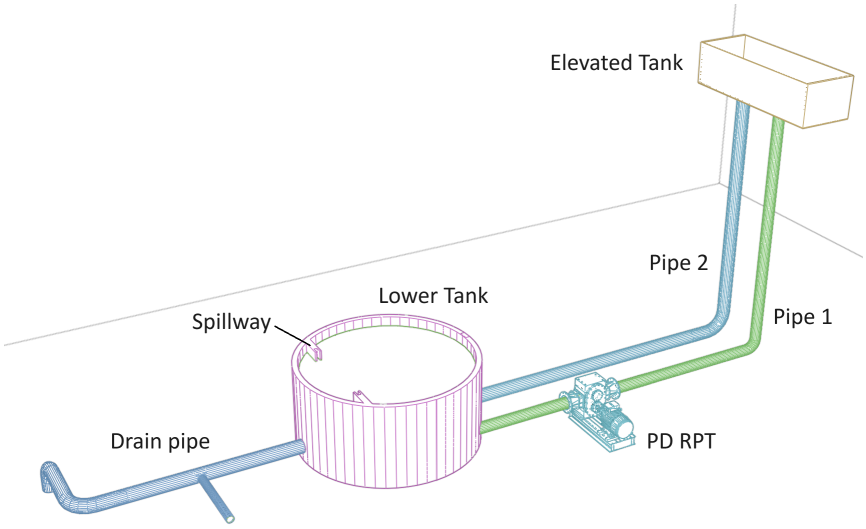

Figure 6.1: 3D representation of TUB's laboratory setup for the PD RPT tests.

Table 6.1 provides the available net head in each turbine and pump conditions after distributed and localized pressure drops from the pipeline and system are taken into account. linear interpolations may provide intermediate values.

Table 6.1: Available net head at TUB facilities for different gross water head and flow rates.

Q (l/s) or (kg/s)	25	50	100	200
Turbine H_n (m), for H_g = 8.45m	8.39	8.23	7.56	4.88
Turbine H_n (m), for H_g = 7.95m	7.89	7.73	7.06	4.38
Turbine H_n (m), for H_g = 7.45m	7.39	7.23	6.56	3.88
Pump H_n (m), for H_g = 8.45m	8.51	8.67	9.34	12.02
Pump H_n (m), for H_g = 7.95m	8.01	8.17	8.84	11.52
Pump H_n (m), for H_g = 7.45m	7.51	7.67	8.34	11.02

As detailed in Chapter 5, the model described allows for the simplification of CFD simulations into a 2.5D model using ANSYS CFX. Subsequent discussions reveal that leakages in the side gaps would have a negligible impact on this model—particularly at higher rotation speeds. Therefore, computationally expensive 3D simulations would not show a significant impact on the characterization of this PD RPT. On the other hand, models with twisted rotors might benefit from such complete modeling, especially to address cavitation issues.

Simulations were conducted for each pump and turbine case, considering the prescribed net head and flow rate conditions outlined in Table 6.1. The net head was applied to the appropriate inlet or outlet boundaries (in turbine and pump modes, respectively). Simultaneously, the rotation speed for the rotors was established as the additional simulation condition to align with the flow rates specified in Table 6.1. Initially estimated using theoretical values, the rotation speed was fine-tuned once, based on simulated results, to accommodate for potential leakages.

As anticipated, in line with the characteristics of a positive displacement machine, Figure 6.2 displays remarkably similar flow rate values between turbine and pump mode (depicted by the blue and red lines). This observation holds true, except for a small difference corresponding to a variation in leakage values attributed to the direction of the main flow. Moreover, it unmistakably reveals a linear relationship, showcasing an increase with rotation speeds. The solid zones visually represent the pulsation levels around the mean values in both turbine and pump modes. Specifically, pulsation values for turbine mode commence at 8.4% for the lowest plotted speed at 46.6 rpm, gradually decreasing linearly to 7.8% at 520 rpm. In the case of pump mode, the pulsations initiate at around 11.3% at 46.6 rpm, following a linear decline to 8.2% at 520 rpm.

Moreover, it is of paramount importance to note that the theoretical flow rate

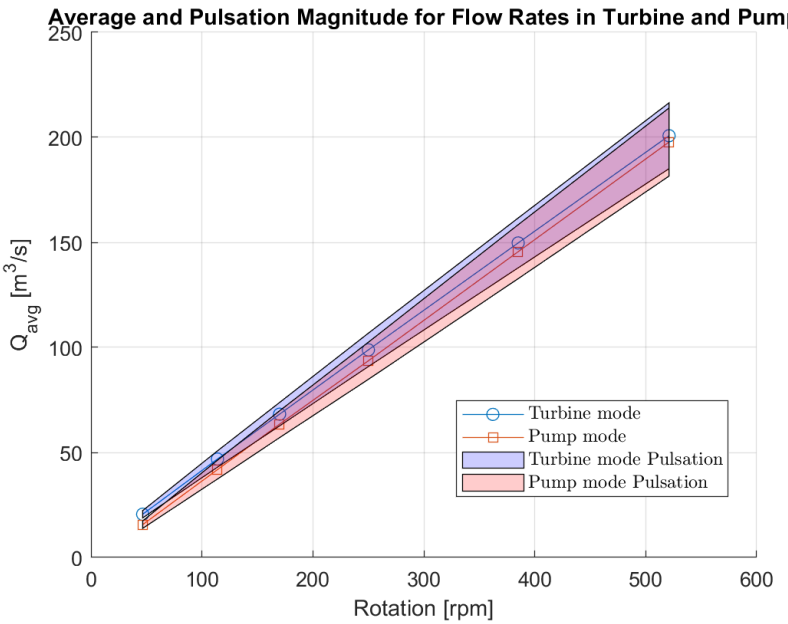

Figure 6.2: Average and pulsation magnitude for flow rates in turbine and pump. Curves for different gross heads are overlapped.

obtained from Equation exhibits a noteworthy alignment with the average values observed in pump and turbine modes. This alignment can be visualized as if a new line were drawn between the red and blue lines in Figure 6.2, although this additional line was intentionally omitted to maintain a clear and uncluttered image. Leakage values from simulated turbine and pump mode could be calculated from the theoretical values, and exhibited approximately the same difference in absolute values, commencing at approximately 13.2% at 46.6 rpm and gradually diminishing in a linear fashion to -1.4% at 520 rpm. This consistent trend in CFD simulations underscore the reliability of the calculated leakage values across a range of rotational speeds.

In Figure 6.3, the turbine generates maximum power at approximately 6350 W around 320 rpm. Upon closer, it suggests that the actual peak power should occur slightly before reaching 320 rpm. Along with Figure 6.5, the maximum turbine power coincides with a turbine efficiency of 72.5%.

Figure 6.4 illustrates an increasing power trend with the rotation speed, indicative of a power relation.

Figures 6.5 and 6.6 depict turbine and pump efficiencies as a function of rotor rotation speed. At 140 rpm, both turbine and pump modes exhibit their maximum efficiencies, reaching 91.6%. Despite this common peak value, the efficiency curves

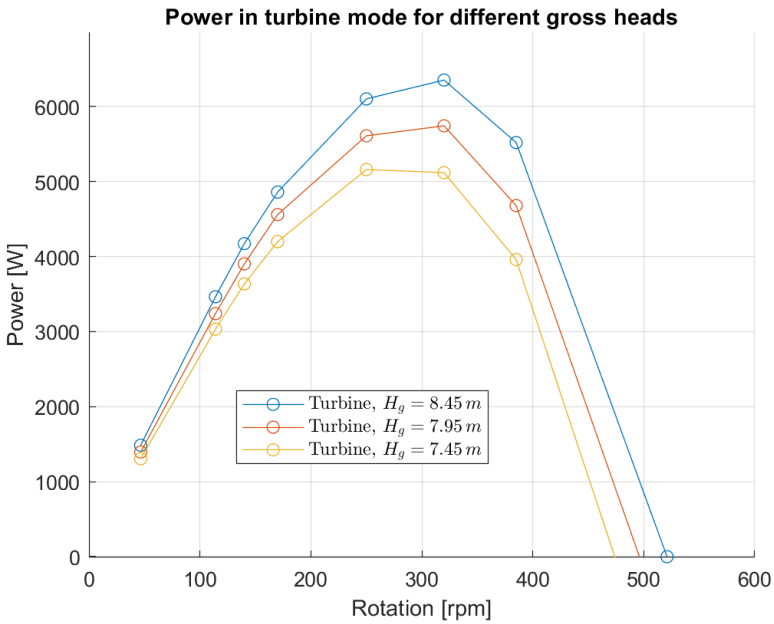

Figure 6.3: Average generated power in turbine mode for different gross heads.

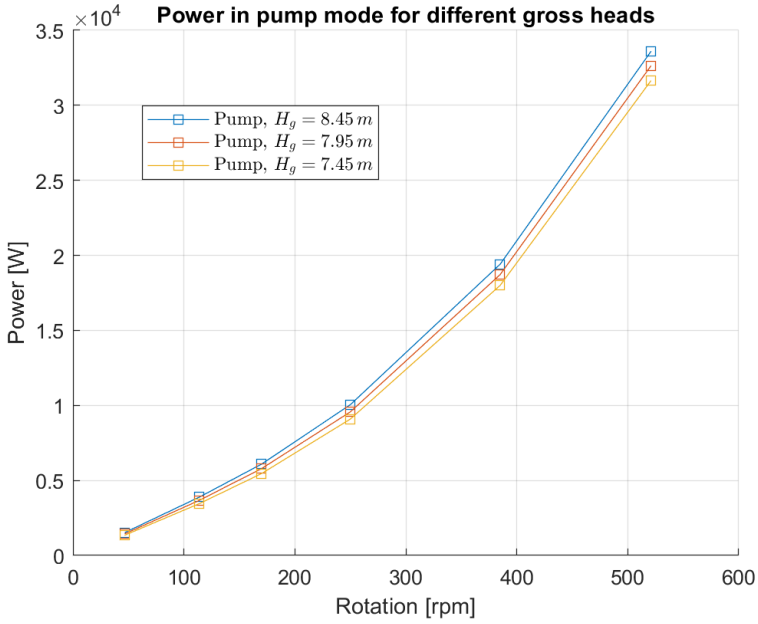

Figure 6.4: Average required power in pump mode for different gross heads.

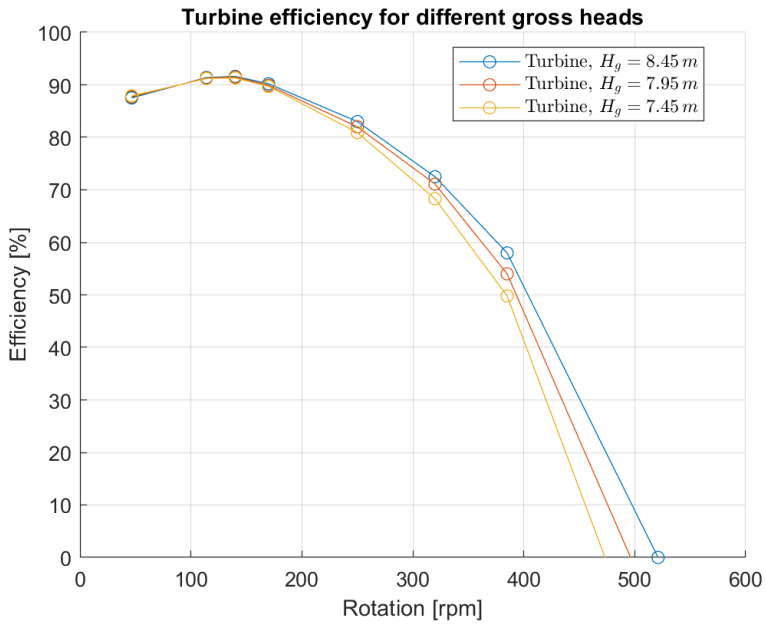

Figure 6.5: Average efficiency in turbine mode for different gross heads.

display distinct behaviors.

In turbine mode, efficiency experiences a sharp decline, dropping below zero for the highest rotation speeds. Conversely, in pump mode, efficiencies remain above 70% even at higher rotation speeds. The contrasting efficiency trends highlight the distinct operational characteristics between turbine and pump modes.

Therefore, disregarding losses attributed to mechanical inefficiencies, the round-trip efficiency for the designed lobe RPT reaches a value of 83.9%.

Understanding both the average and maximum torque that the PD RPT is subjected to is crucial for maintaining control and ensuring the safety of both the machine and operators during its operation. Similar to the significance of flow rate, pulsation serves as a critical parameter, where elevated values can significantly impact the machine's operational efficiency and performance. Consequently, thoroughly comprehending these torque and pulsation factors is indispensable for optimal machine functioning and safety assurance.

Figure 6.7 illustrates a decrease in both average and maximum torques in turbine mode as the rotation speed increases. Despite the possibility of average torques reaching negative values for speeds exceeding 500 rpm (case-dependent), signifying insufficient power generation at that synchronous speed, the escalation in torque pulsation results in a significant increase in the maximum torque applied to the rotor.

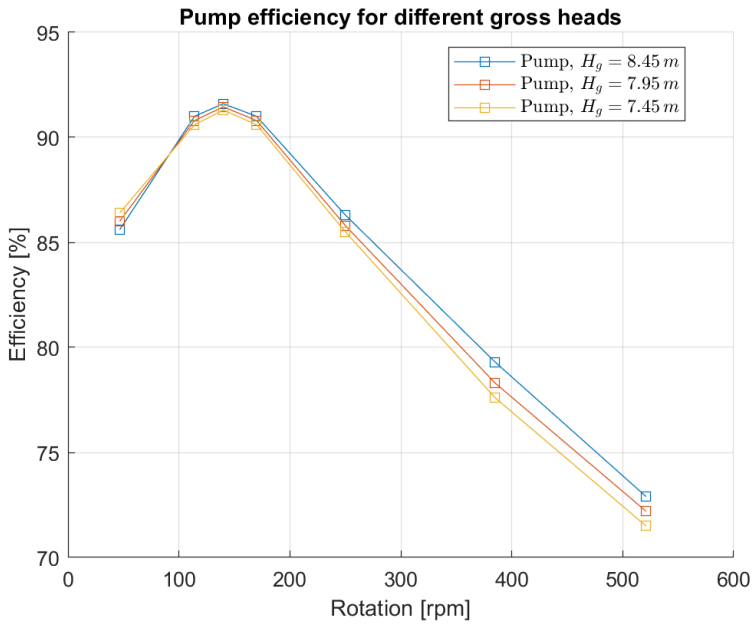

Figure 6.6: Average efficiency in pump mode for different gross heads.

In pump mode, Figure 6.8 reveals a rising trend in both average and maximum torques with increasing rotation speed. Torque pulsation initiates at approximately 11.8% for 46.6 rpm and intensifies to 38.4-40.0% at 520 rpm, depending on the gross head.

In conclusion, as depicted in Figure 6.7 and Figure 6.8, the turbine mode exhibits a decreasing trend in torque values with increasing rotations, implying fewer restrictions on motor selection. However, in pump mode, the feasibility is constrained by the equivalent rotation speed matching the available torque provided by the selected motor to be installed on the PD RPT shaft. In practical terms, consider the scenario where the maximum allowable torque provided by the motor is 360 N.m, as illustrated in Figure 5.4a. This implies that the pump mode remains feasible only up to a rotation speed of 170 rpm.

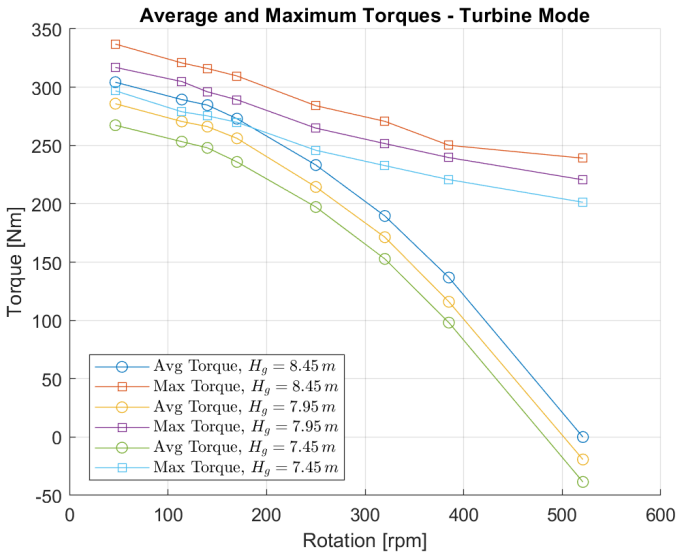

Figure 6.7: Average and maximum torques for different gross heads in turbine mode.

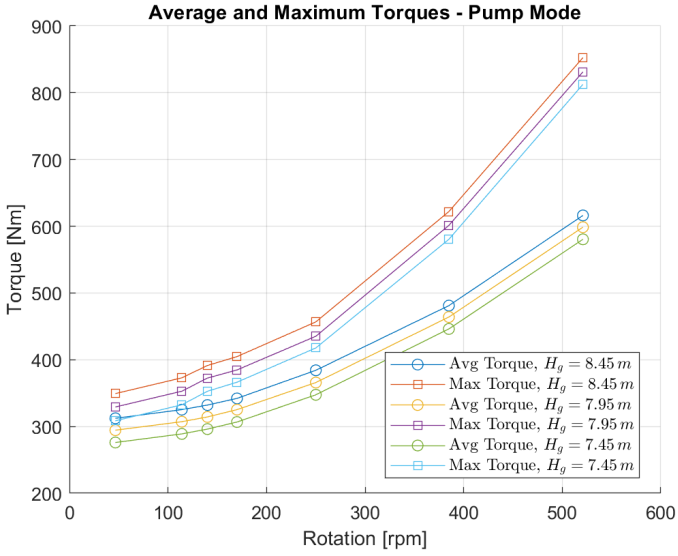

Figure 6.8: Average and maximum torques for different gross heads in pump mode.

CHAPTER
SEVEN

Conclusion

This thesis delved into reversible pump turbine machines, ultimately focusing on the potential of positive displacement lobe pumps as an innovative and unexplored alternative for energy storage. The emphasis was on their suitability for low-head pumped hydro storage in shallow seas and coastal environments with flat topography, where water heads are anticipated to be less than 30 meters.

We initiated our exploration with a comprehensive literature review of current low-head pumped hydro storage applications and an overview of machines designed to operate seamlessly in both pump and turbine modes. This system is crafted to store energy by harnessing excess generated power from renewable sources, such as solar and wind power, and subsequently reintegrate that stored energy into the electric grid during periods when these sources are unable to meet the grid's power demands. This approach could offer grid stability for the increasing share of intermittent renewable energy sources in the energy mix.

Having identified the lobe pump as a promising candidate capable of functioning in turbine mode and potentially offering fish-friendly operating conditions due to its intrinsic design, we proceeded to characterize the machine. This involved providing design parametrization, offering initial insights into an optimal design for efficiency, and furnishing theoretical equations for power, torque, and flow rate delivery.

The experiments serving as the foundation for this Thesis' numerical studies and validation were delineated. Two operational conditions in pump mode and one in turbine mode were specified for numerical comparison. The immersed boundary method was initially used as a meshing technique for numerical validation. However, challenging numerical instabilities and the need to address uncertain yet crucial leakage values prompted a shift in the numerical technique toward a deformable mesh approach.

The deformable mesh technique, implemented using TwinMesh and ANSYS

CFX, demonstrated its reliability. A sensitivity study on the actual gap sizes yielded comparable values between experimental and CFD results for both pump mode operating points. However, average flow rate values in turbine mode could not be validated, and comparisons with theoretical values, coupled with uncertainties highlighted by experimentalists, underscored the necessity of constructing a new rig to verify the rig's operation in turbine mode.

Particle image velocimetry (PIV) data provided compelling evidence of successfully implementing the numerical model for both pump and turbine modes. Despite the impossibility of matching average values for turbine mode, similar fluid flow structures between CFD and PIV data could be observed.

In addition to enhancing our understanding of efficiency optimization, parametric design optimization studies were conducted. These studies revealed efficiency peaks when the rotor diameter and channel width are equal. Additionally, it was substantiated that minimizing gaps in the design, particularly when rotor surfaces adhere to a cycloidal profile, is paramount. This should be pursued to the fullest extent possible during assembly and manufacturing. Finally, fluid-structure interaction simulations were employed to assess the mechanical loads on the machine, and the results indicated safe levels of operation.

Aligned with the design criteria aimed at optimizing a reversible lobe pump turbine, a novel experiment was conceived. A model-scale rig featuring a reversible three-lobe pump turbine with straight rotors was crafted for a system with a maximum physical head of 8.45 meters. Simulation results for a machine with a rotor diameter of 348.67 mm and rotor height of 300 mm showcased a peak power output of 6350 W at approximately 320 rpm, achieving a turbine efficiency of 72.5%. Moreover, it achieved a commendable maximum round-trip efficiency of 83.9% when operating at 140 rpm, aligning with the primary objective of this thesis to attain round-trip efficiency values surpassing 70%. Finally, while pulsations did not represent important issues in turbine mode, they emerged as a pivotal factor in selecting the appropriate motor for pump mode, introducing higher maximum torques that may constrain the choice of motors to be procured and coupled with the system.

In summary, within the uncharted domain of low-head seawater pumped hydro storage applications, this thesis sheds light on the positive displacement reversible pump-turbine as a machine capable of delivering high efficiencies in both pump and generating modes. Although there is currently a lack of prototype scale and experimental data to validate its feasibility, especially concerning its fish-friendly attributes, the inherent characteristics of this technology hint at its potential as a viable option.

CHAPTER
EIGHT

Outlook

The insights derived from this thesis lay the foundation for ongoing research in the realm of reversible lobe pump turbines for low-head pumped hydro storage applications.

While it has been demonstrated that Positive Displacement Reversible Pump Turbines can yield high round-trip efficiency values, there remains a need for further comparisons and numerical validations utilizing new experimental data.

Exploration into cavitation studies is imperative, with potential benefits from both experimental investigations and numerical simulations focusing on twisted rotor configurations. Such configurations not only hold promise for neutralizing potential cavitation issues but also offer noise reduction.

Future endeavors should extend to the investigation of larger machines capable of providing increased flow rates and power generation. These studies are vital for evaluating leakage and efficiency values at the prototype scale.

Continued development could shed light on pertinent dimensionless numbers and establish correlations between model and prototype scale. While a preliminary similarity study was conducted in this work, the size effect could not be adequately addressed without empirical correction factors.

The fish-friendliness aspect also warrants attention. Despite the absence of bladed elements and the ability of rotors to operate at lower rotational speeds, which are favorable for aquatic life, the varying pressure within enclosed chambers during rotor rotation may pose risks of rapid decompression for fish. Further exploration is needed to understand the impact of pressure changes on aquatic life, considering factors such as shear stress, turbulence, cavitation, impact with walls and components, and grinding and abrasion.

An intriguing avenue for investigation is the transition speed between pump and turbine modes and its implications for new stresses and machine lifespan.

Moreover, economic studies are essential to determine the levelized cost of energy per unit, as well as the possible advantages of parallelization and serial unit implementation.

The author expresses optimism for additional testing to provide a more definitive understanding of the practical applicability of the studied concept in the field of pumped hydro storage.

Bibliography

Ak, M., Kentel, E., & Kucukali, S. (2017). A fuzzy logic tool to evaluate low-head hydropower technologies at the outlet of wastewater treatment plants. *Renewable and Sustainable Energy Reviews*, *68*, 727–737. https://doi.org/https://doi.org/10.1016/j.rser.2016.10.010

ALPHEUS. (2023). *Alpheus: Augmenting grid stability through low head pumped hydro energy utilization and storage*. Retrieved December 12, 2023, from https://alpheus-h2020.eu/about/

ANSYS, Inc. (2020). *Ansys cfx reference guide, release 2020 r2, fluid structure interaction* [Release 2020 R2]. ANSYS, Inc. Canonsburg, PA, USA.

Ardizzon, G., Cavazzini, G., & Pavesi, G. (2014). A new generation of small hydro and pumped-hydro power plants: Advances and future challenges. *Renewable and Sustainable Energy Reviews*, *31*, 746–761. https://doi.org/https://doi.org/10.1016/j.rser.2013.12.043

Barbour, E., Wilson, I. G., Radcliffe, J., Ding, Y., & Li, Y. (2016). A review of pumped hydro energy storage development in significant international electricity markets. *Renewable and Sustainable Energy Reviews*, *61*, 421–432. https://doi.org/https://doi.org/10.1016/j.rser.2016.04.019

Barnhart, C. J., & Benson, S. M. (2013). On the importance of reducing the energetic and material demands of electrical energy storage. *Energy Environ. Sci.*, *6*, 1083–1092. https://doi.org/10.1039/C3EE24040A

Bocquel, A., & Janning, J. (2005). Analysis of a 300 mw variable speed drive for pump-storage plant applications. https://ieeexplore.ieee.org/document/1665624/authors#authors

Breeze, P. (2018). Chapter 8 - pumped storage hydropower. In P. Breeze (Ed.), *Hydropower* (pp. 73–78). Academic Press. https://doi.org/https://doi.org/10.1016/B978-0-12-812906-7.00008-9

CFX Berlin. (2024). *Twinmesh features* [Accessed: 03/01/2024]. https://www.twinmesh.com/twinmesh-features/

Dixon, S. L., & Hall, C. A. (2014). *Fluid mechanics and thermodynamics of turbomachinery* (Seventh edition). Butterworth-Heinemann is an imprint of Elsevier.

Fahlbeck, J., Nilsson, H., & Salehi, S. (2021). Flow characteristics of preliminary shutdown and startup sequences for a model counter-rotating pump-turbine. *Energies*, *14*(12). https://doi.org/10.3390/en14123593

Furukawa, A., Shigemitsu, T., & Watanabe, S. (2007). Performance test and flow measurement of contra-rotating axial flow pump. *Journal of Thermal Science*, *16*, 7–13. https://doi.org/https://doi.org/10.1007/s11630-007-0007-4

Hall, J. (2023). *Pump practices: Keep lobes in mind.* Retrieved December 12, 2023, from https://www.chemicalprocessing.com/articles/2006/002/

Henn, E. A. L. (2012). *Máquinas de fluido* (3rd). UFSM.

Hoffstaedt, J., Truijen, D., Fahlbeck, J., Gans, L., Qudaih, M., Laguna, A., De Kooning, J., Stockman, K., Nilsson, H., Storli, P.-T., Engel, B., Marence, M., & Bricker, J. (2022). Low-head pumped hydro storage: A review of applicable technologies for design, grid integration, control and modelling. *Renewable and Sustainable Energy Reviews*, *158*, 112119. https://doi.org/https://doi.org/10.1016/j.rser.2022.112119

Hunt, J. D., Zakeri, B., Lopes, R., Barbosa, P. S. F., Nascimento, A., de Castro, N. J., Brandão, R., Schneider, P. S., & Wada, Y. (2020). Existing and new arrangements of pumped-hydro storage plants. *Renewable and Sustainable Energy Reviews*, *129*, 109914. https://doi.org/https://doi.org/10.1016/j.rser.2020.109914

IEA. (2021). *Global energy review 2021*. International Energy Agency.

IPCC. (2013). *Climate Change 2013: The Physical Science Basis. Contribution of Working Group I to the Fifth Assessment Report of the Intergovernmental Panel on Climate Change* (T. Stocker, D. Qin, G.-K. Plattner, M. Tignor, S. Allen, J. Boschung, A. Nauels, Y. Xia, V. Bex & P. Midgley, Eds.). Cambridge University Press.

IPCC. (2023). Summary for Policymakers. In *Climate Change 2023: Synthesis Report. Contribution of Working Groups I, II and III to the Sixth Assessment Report of the Intergovernmental Panel on Climate Change [Core Writing Team, H. Lee and J. Romero (eds.)]* (pp. 1–34). Intergovernmental Panel on Climate Change. Geneva, Switzerland. https://doi.org/10.59327/IPCC/AR6-9789291691647

Javed, M. S., Ma, T., Jurasz, J., & Amin, M. Y. (2020). Solar and wind power generation systems with pumped hydro storage: Review and future perspectives.

Renewable Energy, *148*, 176–192. https://doi.org/https://doi.org/10.1016/j.renene.2019.11.157

Joseph, A., Chelliah, T. R., Lee, S. S., & Lee, K.-B. (2018). Reliability of variable speed pumped-storage plant. *Electronics*, *7*(10). https://doi.org/10.3390/electronics7100265

Jülch, V. (2016). Comparison of electricity storage options using levelized cost of storage (lcos) method. *Applied Energy*, *183*, 1594–1606. https://doi.org/https://doi.org/10.1016/j.apenergy.2016.08.165

Kang, Y.-H., Vu, H.-H., & Hsu, C.-H. (2012). Factors impacting on performance of lobe pumps: A numerical evaluation. *Journal of Mechanics*, *28*(2), 229–238. https://doi.org/10.1017/jmech.2012.26

Karassik, I. J. (2001). *Pump handbook*.

Karassik, I. (2008). *Pump handbook*. McGraw-Hill. https://books.google.no/books?id=MNq-mAEACAAJ

Kim, J.-W., Suh, J.-W., Choi, Y.-S., Lee, K.-Y., Kanemoto, T., & Kim, J.-H. (2018). Optimized blade design of counter-rotating-type pump-turbine unit operating in pump and turbine modes. *International Journal of Rotating Machinery*, *2018*, 1–12.

Kougias, I., Aggidis, G., Avellan, F., Deniz, S., Lundin, U., Moro, A., Muntean, S., Novara, D., Pérez-Díaz, J. I., Quaranta, E., Schild, P., & Theodossiou, N. (2019). Analysis of emerging technologies in the hydropower sector. *Renewable and Sustainable Energy Reviews*, *113*, 109257. https://doi.org/https://doi.org/10.1016/j.rser.2019.109257

Krampe, P., & Ørke, P. (2012). Four-quadrant operation of rotary lobe pumps and regenerative throttling.

Kurokawa, J., Matsui, J., & Choi, Y.-D. (2008). Flow analysis in positive displacement micro-hydro turbine and development of low pulsation turbine. *International Journal of Fluid Machinery and Systems*, *1*, 76–85. https://doi.org/https://doi.org/10.5293/ijfms.2008.1.1.076

Li, Y.-b., Du, J., & Guo, D.-S. (2019). Numerical research on viscous oil flow characteristics inside the rotor cavity of rotary lobe pump. *Journal of the Brazilian Society of Mechanical Sciences and Engineering*, *41*, 274. https://doi.org/https://doi.org/10.1007/s40430-019-1781-0

Loots, I., van Dijk, M., Barta, B., van Vuuren, S., & Bhagwan, J. (2015). A review of low head hydropower technologies and applications in a south african context. *Renewable and Sustainable Energy Reviews*, *50*, 1254–1268. https://doi.org/https://doi.org/10.1016/j.rser.2015.05.064

Macintyre, A. (1987). *Bombas e instalações de bombeamento*. Ed. Guanabara. https://books.google.no/books?id=FApRkgEACAAJ

McLean, E., & Kearney, D. (2014). An evaluation of seawater pumped hydro storage for regulating the export of renewable energy to the national grid [8th International Renewable Energy Storage Conference and Exhibition (IRES 2013)]. *Energy Procedia*, *46*, 152–160. https://doi.org/https://doi.org/10.1016/j.egypro.2014.01.168

Nilsson, H., & Chernoray, V. (2023a). *Data files: Experimental data from model tests of pd design*. Retrieved December 12, 2023, from https://alpheus-h2020.eu/deliverables/

Nilsson, H., & Chernoray, V. (2023b). Experimental data from model tests of the small-scale positive-displacement pump-turbine design of the alpheus project (deliverable 2.5). https://doi.org/10.4121/370f4182-827c-4e45-9781-94c61cfd6509.v1

Phommacchanh, D., Kurokawa, J., Choi, Y.-D., & Nakajima, N. (2006). Development of a positive displacement micro-hydro turbine. *JSME International Journal*, *49*(2), 482–489. https://doi.org/doi:10.1299/jsmeb.49.482

Pump School. (2023). http://www.pumpschool.com/

Qudaih, M., Engel, B., Truijen, D. P. K., De Kooning, J. D. M., Stockman, K., Hoffstaedt, J., Jarquin-Laguna, A., Ruiz, R. A., Goseberg, N., de Vilder, L., Bricker, J. D., Joseph, M., Zangeneh, M., & Terheiden, K. (2023). The contribution of low-head pumped hydro storage to grid stability in future power systems. *IET Renewable Power Generation*, *17*(14), 3594–3608. https://doi.org/https://doi.org/10.1049/rpg2.12668

Rane, S., Kovačević, A., Stošić, N., & Smith, I. (2017). Highly deforming computational meshes for cfd analysis of twin-screw positive displacement machines. In A. Ionescu (Ed.), *Computational fluid dynamics*. IntechOpen. https://doi.org/10.5772/intechopen.71885

Rehman, S., Al-Hadhrami, L. M., & Alam, M. M. (2015). Pumped hydro energy storage system: A technological review. *Renewable and Sustainable Energy Reviews*, *44*, 586–598. https://doi.org/https://doi.org/10.1016/j.rser.2014.12.040

Renewables 2021 global status report. (2021). REN21.

RONAMIC. (2017). *Ronamic pump*. RONAMIC.

Roy, S., De, A., & Balaras, E. (2020). *Immersed boundary method: Development and applications*. Springer Nature Singapore. https://books.google.no/books?id=udXkDwAAQBAJ

Schiffer, J. (2012). A comparison of cfd-calculations and measurements of the fluid flow in rotating displacement pumps.

Sonawat, A., Choi, Y.-S., Kim, K. M., & Kim, J.-H. (2021). Parametric study on the effect of inlet and outlet pipe shape on the flow fluctuation characteristics associated with a positive displacement hydraulic turbine. *Renewable Energy*, *163*, 1046–1062. https://doi.org/https://doi.org/10.1016/j.renene.2020.09.025

Sonawat, A., Kim, S.-J., Yang, H.-M., Choi, Y.-S., Kim, K.-M., Lee, Y.-K., & Kim, J.-H. (2020). Positive displacement turbine - a novel solution to the pressure differential control valve failure problem and energy utilization. *Energy*, *190*, 116400. https://doi.org/https://doi.org/10.1016/j.energy.2019.116400

van de Nes, R. (2016). *Cfd simulations turbine performance*. ONE Simulations BV.

Vande Voorde, J., Vierendeels, J., & Dick, E. (2004). Flow simulations in rotary volumetric pumps and compressors with the fictitious domain method [Selected Papers from the Second International Conference on Advanced Computational Methods in Engineering (ACOMEN 2002)]. *Journal of Computational and Applied Mathematics*, *168*(1), 491–499. https://doi.org/https://doi.org/10.1016/j.cam.2003.04.007

Verzicco, R. (2023). Immersed boundary methods: Historical perspective and future outlook. *Annual Review of Fluid Mechanics*, *55*(1), 129–155. https://doi.org/10.1146/annurev-fluid-120720-022129

Weisstein, E. W. (2023a). *"epicycloid." from mathworld–a wolfram web resource.* [Accessed: 12/12/2023]. https://mathworld.wolfram.com/Epicycloid.html

Weisstein, E. W. (2023b). *"hypocycloid." from mathworld–a wolfram web resource.* [Accessed: 12/12/2023]. https://mathworld.wolfram.com/Hypocycloid.html

White, F., & Chul, R. (2016). *Fluid mechanics*. McGraw-Hill Education. https://books.google.no/books?id=7AEzjwEACAAJ

YoosefDoost, A., & Lubitz, W. D. (2020). Archimedes screw turbines: A sustainable development solution for green and renewable energy generation—a review of potential and design procedures. *Sustainability*, *12*(18). https://doi.org/10.3390/su12187352

Appendix A
MATLAB Codes

A.1 MATLAB code for preparing CFD velocities fields.

Listing A.1: CFD velocity fields with mesh interpolation.

```
clear all
close all

% view = 'Pump_55rpm_085mm_Velocity_u_v_-7degrees';
% view = 'Pump_55rpm_085mm_Velocity_u_v_+8degrees';
% view = 'Pump_55rpm_085mm_Velocity_u_v_+23degrees';
% view = 'Pump_45rpm_085mm_Velocity_u_v_-7degrees';
% view = 'Pump_45rpm_085mm_Velocity_u_v_+8degrees';
% view = 'Pump_45rpm_085mm_Velocity_u_v_+23degrees';
% view = 'Turbine_45rpm_085mm_Velocity_u_v_-7degrees';
% view = 'Turbine_45rpm_085mm_Velocity_u_v_+8degrees';
view = 'Turbine_45rpm_085mm_Velocity_u_v_+23degrees';

%%% Phase of Rotation that match PIV perspective angles
% rotation = -7;
% rotation = +8;
rotation = +23;

titleText = 'Turbine45rpm'+"_"+rotation; %Pump45rpm,
    Pump55rpm, Turbine45rpm
%%%%%%%%%%%%%%%%%%%%%%%%%%%%%%%%%%%%%%%%%%%%%%%%%%%%%%%%

% Specify the path to the CSV file
mainDirectory = 'CFD-to-MATLAB';
file_path = fullfile(mainDirectory, [view, '.csv']);

% Read the data from the CSV file
data = readmatrix(file_path, 'HeaderLines', 6);

% Extract position and velocity components. U and V are
    adjusted to align with coordinates with PIV
```

```
X = data(:, 1);
Y = data(:, 2);
u = data(:, 5);
v = data(:, 4) * (-1);

% Rotate all points (X, Y) by 270 degrees around (0,0) to
    align coordinates
theta = deg2rad(270);
X_rotated = X * cos(theta) - Y * sin(theta) + 0.05; % +0.05
    to match PIV (0,0)
Y_rotated = X * sin(theta) + Y * cos(theta) + 0.075; % +0.075
     to match PIV (0,0)

% Convert positions to millimeters
X_mm = X_rotated * 1000;
Y_mm = Y_rotated * 1000;

%REGION MASKS for each degree of rotation
if rotation == -7
    polygon_vertices_1 = [-15, -5.48, 17.05, 1, -15; 75.02,
        75.02, 38.2, 0, 0];
    polygon_mask_1 = inpolygon(X_mm, Y_mm, polygon_vertices_1
        (1, :), polygon_vertices_1(2, :));
    triangle1_mask = inpolygon(X_mm, Y_mm, [-8.1, -0.12,
        0.79], [75.02, 75.02, 65.5]);
    polygon_vertices_2 = [155, 100.1, 83.52, 100.1, 155;
        75.02, 75.02, 36.97, 0.2, 0.2];
    polygon_mask_2 = inpolygon(X_mm, Y_mm, polygon_vertices_2
        (1, :), polygon_vertices_2(2, :));
    triangle2_mask = inpolygon(X_mm, Y_mm, [95, 81, 99], [60,
         38.1, 18.2]); %it's ignored in the end. Polygon gets
         it all.
elseif rotation == 8
    polygon_vertices_1 = [-15, -0.125, 16.9, -2.57, -15;
        75.5, 75.5, 38.62, 0, 0];
    polygon_mask_1 = inpolygon(X_mm, Y_mm, polygon_vertices_1
        (1, :), polygon_vertices_1(2, :));
    triangle1_mask = inpolygon(X_mm, Y_mm, [-4.2, 0, 0.28],
        [0, 4.3, 0]); %it's ignored in the end. Polygon gets
        it all.
    polygon_vertices_2 = [155, 99, 83.36, 105.45, 155; 75.5,
        75.5, 37.6, 0, 0];
    polygon_mask_2 = inpolygon(X_mm, Y_mm, polygon_vertices_2
        (1, :), polygon_vertices_2(2, :));
    triangle2_mask = inpolygon(X_mm, Y_mm, [99.7, 99.97,
        106], [11, 0, 0]); %it's ignored in the end. Polygon
        gets it all.
elseif rotation == 23
    polygon_vertices_1 = [-15, -0.12, 17, -7.52, -15; 75.02,
        75.02, 41.87, 0, 0];
    polygon_mask_1 = inpolygon(X_mm, Y_mm, polygon_vertices_1
        (1, :), polygon_vertices_1(2, :));
    triangle1_mask = inpolygon(X_mm, Y_mm, [-1.76, 2.2, -9],
        [12.52, 1.1, 1.1]);
```

```
    polygon_vertices_2 = [155, 100.12, 83.52, 110.65, 155;
        75.02, 75.02, 38.23, 0, 0];
    polygon_mask_2 = inpolygon(X_mm, Y_mm, polygon_vertices_2
        (1, :), polygon_vertices_2(2, :));
    triangle2_mask = inpolygon(X_mm, Y_mm, [99.33, 98.37,
        107.6], [17.25, 1.1, 1.1]);
end

% Interpolate u and v values for the new points inside the
    regions
method = 'cubic'; %linear, cubic, nearest, v4, natural

x_polygon_1 = linspace(min(X_mm(polygon_mask_1)), max(X_mm(
    polygon_mask_1)), 80);
y_polygon_1 = linspace(min(Y_mm(polygon_mask_1)), max(Y_mm(
    polygon_mask_1)), 80);
[X_polygon_1, Y_polygon_1] = meshgrid(x_polygon_1,
    y_polygon_1);
u_polygon_1 = griddata(X_mm(polygon_mask_1), Y_mm(
    polygon_mask_1), u(polygon_mask_1), X_polygon_1,
    Y_polygon_1, method);
v_polygon_1 = griddata(X_mm(polygon_mask_1), Y_mm(
    polygon_mask_1), v(polygon_mask_1), X_polygon_1,
    Y_polygon_1, method);

x_triangle1 = linspace(min(X_mm(triangle1_mask)), max(X_mm(
    triangle1_mask)), 50);
y_triangle1 = linspace(min(Y_mm(triangle1_mask)), max(Y_mm(
    triangle1_mask)), 50);
[X_triangle1, Y_triangle1] = meshgrid(x_triangle1,
    y_triangle1);
u_triangle1 = griddata(X_mm(triangle1_mask), Y_mm(
    triangle1_mask), u(triangle1_mask), X_triangle1,
    Y_triangle1, method);
v_triangle1 = griddata(X_mm(triangle1_mask), Y_mm(
    triangle1_mask), v(triangle1_mask), X_triangle1,
    Y_triangle1, method);

x_polygon_2 = linspace(min(X_mm(polygon_mask_2)), max(X_mm(
    polygon_mask_2)), 80);
y_polygon_2 = linspace(min(Y_mm(polygon_mask_2)), max(Y_mm(
    polygon_mask_2)), 80);
[X_polygon_2, Y_polygon_2] = meshgrid(x_polygon_2,
    y_polygon_2);
u_polygon_2 = griddata(X_mm(polygon_mask_2), Y_mm(
    polygon_mask_2), u(polygon_mask_2), X_polygon_2,
    Y_polygon_2, method);
v_polygon_2 = griddata(X_mm(polygon_mask_2), Y_mm(
    polygon_mask_2), v(polygon_mask_2), X_polygon_2,
    Y_polygon_2, method);

x_triangle2 = linspace(min(X_mm(triangle2_mask)), max(X_mm(
    triangle2_mask)), 50);
y_triangle2 = linspace(min(Y_mm(triangle2_mask)), max(Y_mm(
    triangle2_mask)), 50);
```

```
[X_triangle2, Y_triangle2] = meshgrid(x_triangle2,
    y_triangle2);
u_triangle2 = griddata(X_mm(triangle2_mask), Y_mm(
    triangle2_mask), u(triangle2_mask), X_triangle2,
    Y_triangle2, method);
v_triangle2 = griddata(X_mm(triangle2_mask), Y_mm(
    triangle2_mask), v(triangle2_mask), X_triangle2,
    Y_triangle2, method);

% Plot for Velocity u with interpolation
figure
scatter(X_mm, Y_mm, 5, u, 'filled');
colormap(jet);
caxis([-0.25 0.25])
colorbar;
title('U-velocity␣[m/s]','FontSize',12,'interpreter','latex')
xlabel('Position␣X␣[mm]','FontSize',12,'interpreter','latex')
ylabel('Position␣Y␣[mm]','FontSize',12,'interpreter','latex')
axis equal;
xlim([-10, 150]); % Set x-axis limits
ylim([-60, 130]); % Set y-axis limits
hold on;
scatter(X_polygon_1(:), Y_polygon_1(:), 3, u_polygon_1(:), '
    filled');
scatter(X_polygon_2(:), Y_polygon_2(:), 3, u_polygon_2(:), '
    filled');
if rotation == -7
    % scatter(X_triangle1(:), Y_triangle1(:), 3, u_triangle1
        (:), 'filled');
    % scatter(X_triangle2(:), Y_triangle2(:), 3, u_triangle2
        (:), 'filled');
elseif rotation == 8
    scatter(X_triangle1(:), Y_triangle1(:), 3, u_triangle1(:)
        , 'filled');
    scatter(X_triangle2(:), Y_triangle2(:), 3, u_triangle2(:)
        , 'filled');
elseif rotation == 23
    % scatter(X_triangle1(:), Y_triangle1(:), 3, u_triangle1
        (:), 'filled');
    % scatter(X_triangle2(:), Y_triangle2(:), 3, u_triangle2
        (:), 'filled');
end
hold off;
exportgraphics(gcf,"Figures/"+titleText+"_U"+".png")

% Plot for Velocity v with interpolation
figure
scatter(X_mm, Y_mm, 5, v, 'filled');
colormap(jet);
caxis([-0.25 0.25])
colorbar;
title('V-velocity␣[m/s]','FontSize',12,'interpreter','latex')
xlabel('Position␣X␣[mm]','FontSize',12,'interpreter','latex')
ylabel('Position␣Y␣[mm]','FontSize',12,'interpreter','latex')
axis equal;
```

```
xlim([-10, 150]); % Set x-axis limits
ylim([-60, 130]); % Set y-axis limits
hold on;
scatter(X_polygon_1(:), Y_polygon_1(:), 3, v_polygon_1(:), '
    filled');
scatter(X_polygon_2(:), Y_polygon_2(:), 3, v_polygon_2(:), '
    filled');
if rotation == -7
    % scatter(X_triangle1(:), Y_triangle1(:), 3, u_triangle1
        (:), 'filled');
    % scatter(X_triangle2(:), Y_triangle2(:), 3, u_triangle2
        (:), 'filled');
elseif rotation == 8
    scatter(X_triangle1(:), Y_triangle1(:), 3, u_triangle1(:)
        , 'filled');
    scatter(X_triangle2(:), Y_triangle2(:), 3, u_triangle2(:)
        , 'filled');
elseif rotation == 23
    % scatter(X_triangle1(:), Y_triangle1(:), 3, u_triangle1
        (:), 'filled');
    % scatter(X_triangle2(:), Y_triangle2(:), 3, u_triangle2
        (:), 'filled');
end
hold off;
exportgraphics(gcf,"Figures/"+titleText+"_V"+".png")
```

Appendix B
Scientific publications

Within this appendix, the author's contribution to scientific journal publications is presented. A differentiation is made between the different status regarding publication of each paper. In addition, the abstracts are added, the Thesis author's contribution is explained, and eventual overlaps with parts of this Thesis are discussed. For publications that are in preparation, the presented texts are subject to possible adjustments.

B.1 Published

Hoffstaedt, J.P., Truijen, D.P.K., Fahlbeck, J., **Gans, L.H.A.**, Qudaih, M., Laguna, A.J., De Kooning, J.D.M., Stockman, K., Nilsson, H., Storli, P.-T., Engel, B., Marence, M., & Bricker, J.D. (2022). Low-head pumped hydro storage: A review of applicable technologies for design, grid integration, control and modelling. *Renewable and Sustainable Energy Reviews, 158*, 112119. `https://doi.org/10.1016/j.rser.2022.112119`

Contribution In this collaborative effort for the review paper, I played the main responsibility in shaping Chapter 3, focusing on the intricate aspects of pump-turbine design and configuration for low-head pumped hydro storage (PHS). I took on the responsibility of delving into the critical considerations governing the selection of reversible pump-turbine (RPT) units and evaluating pump as turbine (PAT) configurations.

Additionally, I collaborated on incorporating vital information into Chapters 1 and 2, although I did not serve as the lead for these sections. My role involved contributing to the overall coherence and comprehensiveness of the paper by providing insights, data, and context that enhanced the quality of the review across multiple chapters. The publication covers parts of Chapter 2.

Renewable and Sustainable Energy Reviews 158 (2022) 112119

Contents lists available at ScienceDirect

Renewable and Sustainable Energy Reviews

journal homepage: www.elsevier.com/locate/rser

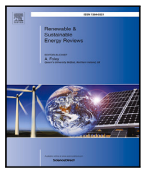

Low-head pumped hydro storage: A review of applicable technologies for design, grid integration, control and modelling

J.P. Hoffstaedt [a,*], D.P.K. Truijen [b], J. Fahlbeck [c], L.H.A. Gans [d], M. Qudaih [e], A.J. Laguna [a], J.D.M. De Kooning [b], K. Stockman [b], H. Nilsson [c], P.-T. Storli [d], B. Engel [e], M. Marence [f], J.D. Bricker [g,h]

[a] Faculty of Mechanical, Maritime and Materials Engineering, Department of Maritime and Transport Technology, Delft University of Technology, Mekelweg 2, 2628 CD Delft, The Netherlands
[b] Department of Electromechanical Systems & Metal Engineering, Ghent University & FlandersMake@UGent - Corelab EEDT-MP, Sint-Martens-Latemlaan 2B, 8500 Kortrijk, Belgium
[c] Department of Mechanics and Maritime Sciences, Division of Fluid Dynamics, Chalmers University of Technology, 412 96 Gothenburg, Sweden
[d] Department of Energy and Process Engineering, Waterpower Laboratory, Norwegian University of Science and Technology, NO-7491 Trondheim, Norway
[e] Elenia Institute for High Voltage Technology and Power Systems, Technische Universität Braunschweig, Schleinitzstraße 23, 38106 Braunschweig, Germany
[f] IHE Delft Institute for Water Education, Westvest 7, 2611 AX Delft, The Netherlands
[g] Department of Hydraulic Engineering, Hydraulic Structures and Flood Risk, Delft University of Technology, The Netherlands
[h] Department of Civil and Environmental Engineering, University of Michigan, 2350 Hayward, Ann Arbor, MI 48109-2125, USA

ARTICLE INFO

Keywords:
Low-head pumped hydro storage
Energy storage
Grid stability
Renewables integration
Energy transition
Reversible pump-turbine

ABSTRACT

To counteract a potential reduction in grid stability caused by a rapidly growing share of intermittent renewable energy sources within our electrical grids, large scale deployment of energy storage will become indispensable. Pumped hydro storage is widely regarded as the most cost-effective option for this. However, its application is traditionally limited to certain topographic features. Expanding its operating range to low-head scenarios could unlock the potential of widespread deployment in regions where so far it has not yet been feasible. This review aims at giving a multi-disciplinary insight on technologies that are applicable for low-head (2-30 m) pumped hydro storage, in terms of design, grid integration, control, and modelling. A general overview and the historical development of pumped hydro storage are presented and trends for further innovation and a shift towards application in low-head scenarios are identified. Key drivers for future deployment and the technological and economic challenges to do so are discussed. Based on these challenges, technologies in the field of pumped hydro storage are reviewed and specifically analysed regarding their fitness for low-head application. This is done for pump and turbine design and configuration, electric machines and control, as well as modelling. Further aspects regarding grid integration are discussed. Among conventional machines, it is found that, for high-flow low-head application, axial flow pump-turbines with variable speed drives are the most suitable. Machines such as Archimedes screws, counter-rotating and rotary positive displacement reversible pump-turbines have potential to emerge as innovative solutions. Coupled axial flux permanent magnet synchronous motor-generators are the most promising electric machines. To ensure grid stability, grid-forming control alongside bulk energy storage with capabilities of providing synthetic inertia next to other ancillary services are required.

Abbreviations: ADRC, Active Distribution Rejection Control; AF-PMSM, Axial Flux Permanent Magnet Synchronous Machine; ANN, Artificial Neural Network; AS, Ancillary Services; CAES, Compressed Air Energy Storage; CRPT, Counter-Rotating Pump-Turbine; DSO, Distribution System Operator; DSSR, Double-Stator Single-Rotor; DTC, Direct Torque Control; EIA, Energy Information Administration; ESHA, European Small Hydropower Association; ESOEI, Energy Storage On Energy Invested; ESS, Energy Storage System; FOC, Field Oriented Control; IRES, Intermittent Renewable Energy Source; LCOS, Levelised Cost Of Storage; MEPT, Maximum Efficiency Point Tracking; MMD, Modular Machine Drive; MPC, Model Predictive Control; MPPT, Maximum Power Point Tracking; MTPA, Maximum Torque Per Ampere; PAT, Pump As Turbine; PHS, Pumped Hydro Storage; PLL, Phase Locked Loop; PM, Permanent Magnet; PMSM, Permanent Magnet Synchronous Machine; PTO, Power Take-Off; PWM, Pulse-Width Modulation; RPT, Reversible Pump-Turbine; SSDR, Single-Stator Double-Rotor; SSSR, Single-Stator Single-Rotor; SVM, Space Vector Modulation; TSO, Transmission System Operator

* Corresponding author.
E-mail address: J.P.Hoffstaedt@tudelft.nl (J.P. Hoffstaedt).

https://doi.org/10.1016/j.rser.2022.112119
Received 8 September 2021; Received in revised form 17 December 2021; Accepted 9 January 2022

1. Introduction

In a global effort to reduce greenhouse gas emissions, renewables are now the second biggest contributor to the world-wide electricity mix, claiming a total share of 29% in 2020 [1]. Although hydropower takes the largest share within that mix of renewables, solar photovoltaics and wind generation experience steep average annual growth rates of 36.5% and 23%, respectively, since 1990 [2]. Both of these technologies, however, significantly differ in their generation characteristics when compared to traditional thermal power plants. This trend towards an increase in intermittent generation, coupled with a reduction in spinning reserves, could undermine grid stability. To counteract these effects, grid-scale deployment of energy storage is indispensable.

There are complementary approaches to balance demand and supply in an electricity grid, such as an increase in flexible generation, demand management, or exporting and importing electricity. Nonetheless, at certain penetration levels of renewables, to reduce the risk of grid instability, a heterogeneous pool of storage solutions is needed. A wide variety of such storage technologies – including capacitors, flywheels, electro-chemical batteries, compressed air energy storage (CAES), molten-salt or hydrogen storage – is available to balance the grid in the timescale from seconds up to seasonal variations. Crucial factors for large-scale balancing include energy and power capacity as well as fast response times while maintaining high efficiencies. Aside from fulfilling these criteria, the major driver towards commercial deployment is the levelised cost of storage (LCOS); leading in this are pumped hydro storage (PHS) and CAES [3]. An alternative approach is based on the so-called energy stored on energy invested (ESOEI), which gives an estimate of the relation between the stored energy during the lifetime of a system and the energy required to construct the system. Also for this metric, PHS and CAES are, by far, in the lead [4].

Pumped hydro storage is a mature and well-known technology that has been used since the beginning of the 20th century. In 2020, it contributed with 90.3% of the world's energy storage capacity [5]. However, while some regions reach the limits of economically viable PHS that can be implemented, others lack entirely the necessary topographic features. Traditional PHS relies on high heads to realise the expected power and storage capacity. Most of the plants produce in the order of 1000–1500 MW of power, with round-trip efficiencies which are commonly in the range of 70%–85% [6].

Aside from its use to store energy, hydropower is regarded as the foremost renewable generation method when it comes to flexibility and improving grid stability. Due to the proven advantages of hydroelectric power generation, wide-ranging research efforts have focused on conceptual adaptations and technological advancements utilising low- and ultra-low-head scenarios. Some of these technologies, such as wastewater, run-of-river hydropower, or tidal barrages have seen prototyping and commercial deployment. However, theoretical attention and practical implementation towards low-head PHS has been limited. Fig. 1 shows a conceptual drawing of what such a system may consist of when deploying a reversible pump-turbine coupled to a motor-generator that is connected to the grid via an AC-DC-AC converter for variable speed operation.

The lack of attention on low-head PHS can be partly explained through high levelised cost of storage (LCOS) caused by extensive civil structures, enlarged machinery, lower round-trip efficiencies, and limited flexibility to provide ancillary services (AS). The predicted increase in demand for energy balancing and AS in the upcoming decades will likely justify increased LCOS. Additionally, technological advancements could significantly contribute to a reduction in LCOS. Addressing the technological challenges and overcoming economic barriers of low-head PHS could unlock the potential of integrating large-scale energy storage into the grids of regions where it has not been feasible so far.

For the given reasons, research and development towards shifting the operating range of PHS to low heads is scarce. Using a multi-disciplinary approach, the main goal of this research is to review and analyse technologies based on their applicability for low-head utilisation. First, an overview of PHS and its historical development is given. Based on this, recent trends leading to further innovation in the field are identified, and the potential and necessity of storage technologies are discussed. Finally, technological and economic challenges are explored, and the key advancements that could contribute to economic and technical viability are isolated. Building on this, in the major technological fields – pump-turbine design and configuration, control and electric machinery, as well as modelling – the most promising technologies are compared and their fitness for low-head application is assessed. Additionally, implications of grid integration are discussed, including further elaboration on the significance of integrating large-scale energy storage, such as low-head PHS into world-wide grids.

2. Overview and historical development of pumped hydro storage

Pumped hydro storage is an amended concept to conventional hydropower as it cannot only extract, but also store energy. This is achieved by converting electrical to potential energy and vice versa in the form of pumping and releasing water between a lower and a higher reservoir. The energy conversion occurs by using pumps and turbines either combined in a reversible (binary set) or separate configuration (ternary and quaternary sets). The power of such a system, as well as the amount of energy that can be extracted or stored, is proportional to the product of head and water flow or volume, respectively. Hence, a higher head results in a reduced flow for a given desired power and smaller reservoirs for a given storage capacity. It does not, therefore just correlate with scaled-down reservoirs but also smaller remaining civil structures and machinery, historically leading to reduced cost and a significant economic advantage of utilising high-head differences [7].

Of today's bulk energy storage integrated into the world-wide grids, over 90% is comprised of PHS of which the vast majority are high-head applications. According to the International Hydropower Association, in 2019, the global installed capacity reached 158 GW with the biggest contributors being China making up 30.3 GW of the share, Japan 27.6 GW, and the United States 22.9 GW [8]. Fig. 2 shows the distribution of global storage capacity that is operational, under construction, planned, and announced as of 2021.

In comparison, the next largest contributors to bulk energy storage are electro-chemical battery storage – rapidly growing with a total capacity of 14.2 GW – and thermal storage with 2.9 GW in 2020 [5]. To explain the historic market dominance of PHS and understand recent trends, several factors have to be taken into account. Pumped hydro storage utilising reversible pump-turbines has been available as a mature and cost-effective solution for the better part of a century with an estimated energy based capital cost of 5–100 $/kWh [10]. Today, compressed air energy storage is considered mature and reliable, offering similarly low capital cost between 2–50 $/kWh, and electrochemical batteries offer high energy density with higher costs, and experience drastic growth while the impact of hydrogen-based storage in the energy transition is largely expected to be substantial [10].

However, PHS's dominance is not only due to its historic lead but can also be attributed to its technical, economic, and sustainability advantages. These include high efficiencies, large achievable capacities, and long lifetimes. Compared to rapidly expanding battery storage that can be used wherever it is most needed, one clear advantage is this durability. It is currently assumed that a battery system will last around 15–20 years, but on the other hand, the oldest hydropower plant in Norway has been operating for over 120 years [11,12]. Prolonged lifetimes are one factor improving the sustainability of PHS compared to other storage solutions. Others include maturity, low capital and operating cost, as well as low energy and carbon dioxide density. Based on these and other factors regarding economic, performance, technological, and environmental considerations, Ren et al. ranked PHS as the most sustainable storage technology [13].

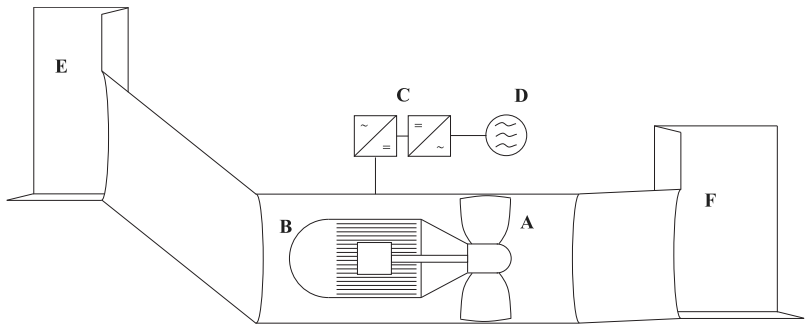

A Reversible Pump-Turbine
B Motor-Generator
C AC-DC-AC Converter
D Power Grid
E Upper Reservoir
F Lower Reservoir

Fig. 1. Schematic showing a low-Head PHS concept and its main components.

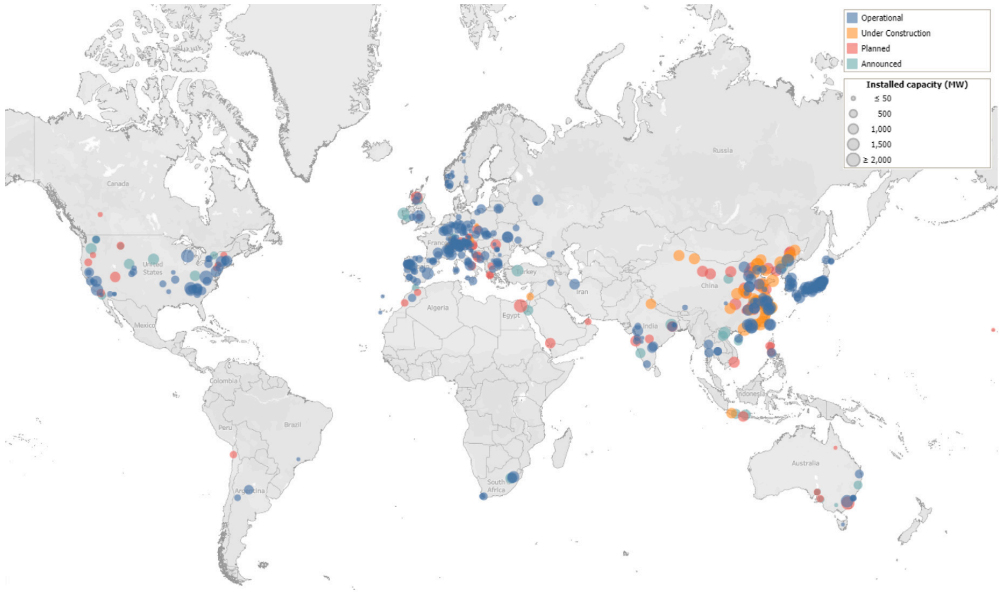

Fig. 2. Global PHS Capacity [9].

Further advantages of PHS include suitability for long-term storage – since hardly any storage losses occur other than seepage and evaporation – and quick availability due to short switch-on and switch-off times. With these factors ensuring a significant share within a heterogeneous pool of storage technologies, one major disadvantage of PHS has historically been its topographic constraints. A switch from river-based to closed-loop off-river systems could overcome some of the constraints and increase the potential for deployment [14,15]. Nonetheless, regions with flat topographies still do not offer viable sites.

2.1. Early deployment and progression in the **20***th century*

Not long after hydropower began to generate electricity, the first small-scale PHS plants were constructed in the mountainous regions of central Europe in the beginning of the 20th century. Initially using separate pumps and turbines, combined reversible pump-turbines have become the norm since the middle of the 20th century [6]. Experiencing a major boom in Europe, parts of Asia, and North America, a large portion of today's installed PHS capacity was constructed in the 1960s, 1970s, and 1980s; in most countries, this occurred alongside rapidly increasing nuclear power. The gained flexibility that PHS plants provided allowed them to match a varying demand with the baseload generation of nuclear power plants. An example where this was particularly relevant is Japan due to its lack of interconnections to other countries as well as their strong strategy towards nuclear energy.

In the United States, another reason for the growing capacity of PHS during that period was the energy crisis in the 1970s, leading to an increased cost of fossil fuels allowing PHS to grow as a substitute for peak balancing [16]. After that period, development slowed down in most regions with the major exception of China. Its rapidly growing economy and correlated energy demand largely satisfied by non-flexible coal plants required major energy storage.

90

Up until this point, pump-turbines were coupled to fixed speed motor-generators. The next significant development occurred in the 1990s when variable speed operation was introduced in Japan. The ability to adjust the angular velocity of the runners allowed for higher efficiencies under changing conditions, reduced the switching time between pump and turbine mode, and facilitated higher ramp rates and quicker response times [17].

2.2. Recent trends

After an initial reduction of PHS deployment around the turn of the millennium, the rapidly growing share of intermittent renewable energy sources (IRES) in the last couple of decades sparked new interest in sustainable flexible generation as well as large-scale energy storage solutions. This caused increasing attention towards the rehabilitation of old hydropower plants and an expansion of PHS [18]. While PHS experienced a much longer development process than competitive technologies and could hence be considered mature, two major trends can be identified pushing further innovation in the field.

The first one is derived from the change in grid characteristics caused by a reduction in spinning reserves. A growing number of converter coupled renewables raise the necessity for external provision of AS. To provide these using PHS, research efforts focus on developing improved control and machinery but also novel concepts, such as hybrid storage solutions. Examples of such concepts could be the coupling of conventional PHS with flywheels for frequency control or supercapacitors providing virtual inertia [19]. Hybrid storage solutions incorporating PHS, such as hybrid pumped and battery storage, are also particularly suited for off-grid applications [20].

The second major trend is expanding the operating range and application. One of the most limiting factors in the potential use of large-scale PHS has been the fact that not many locations could offer economically viable deployment. These were traditionally mountainous regions accessing water with enough space to construct extensive civil structures. There is a large potential in Europe to deploy further mini and small hydropower plants to counteract the effects of higher renewable penetration levels. However, this does not apply to countries with flat topographies, such as Denmark, the Netherlands, or Belgium [21]. Additionally, to achieve the balancing capabilities of pumped storage systems, larger plants typically provide better economies of scale. Suitable locations for such are rare in Europe and some countries like Japan are considered to have used nearly all available sites [22]. This limited availability of appropriate locations drives the development of new approaches. Examples for a promising change of approach are underwater PHS or gravity energy storage.

The former is a recently developed and tested concept based on submerging a hollow sphere offshore and using the static pressure difference for energy storage. The surrounding sea acts as the upper reservoir and the sphere as the lower which can be filled to generate electricity or emptied to store it. Initial model-scale tests have been successful; it is a freely scalable technology without issues regarding land use and considered cost competitive with PHS and compressed air storage [23]. Using seawater in general for PHS is so far an uncommon practice, but has been investigated as a solution for isolated grids [24]. If technical, environmental, and economic challenges are overcome, utilising seawater could be another promising expansion of PHS's potential deployment.

The latter similarly decouples the fundamental principle of PHS from its topographic restrictions. Storage is done via gravitational potential energy. However, energy is stored or extracted respectively by moving a piston of large mass up and down using water powered by a pump-turbine for conversion. While still under development, initial economic evaluations show it to have a potentially attractive LCOS compared to other storage technologies [25].

An alternative that is not less promising and will potentially suit both these trends is to extend the operating range of conventional PHS to low and ultra low-head applications, including the potential use of seawater, while improving its capability to provide AS. If technological advancements allow for economic viability, large-scale low-head PHS could be integrated in regions where PHS so far was not a feasible solution.

Later trends for PHS show the usage of ternary units. With ternary units, a separate pump and turbine are connected on a single shaft to an electric machine that can work either as a motor or a generator [26]. This configuration presents a very flexible and fast response range, shows higher efficiencies than reversible machines, and can utilise hydraulic short circuits for optimal power in- or outtake [27,28]. The major drawback with ternary units is that they requires higher investment and maintenance costs compared to a reversible unit [28]. In a low-head scenario, the increase in investment cost would be even greater since a high-power, low-head machine needs to be large in order to handle a high flow rate. Thus, it is suggested as a less attractive alternative for low-head PHS.

2.3. Potential of deployment and scalability in Europe

Resulting from the rapid transition that grids are experiencing worldwide, the need for energy storage is evident. However, there are a variety of factors influencing the actual storage demand and its expected progression during the coming decades. First and foremost, this is the growth in intermittent and converter coupled renewables. While a direct correlation between renewable penetration levels and storage demand can be assumed, mitigating factors such as improved generation forecasting and the continuous development of renewables able to provide AS will allow for later deployment of energy storage. Further factors to consider include the flexibility of remaining generators in the grids and the emerging need for additional operating reserves, improved demand management, as well as further grid expansion and interconnection.

Bearing these factors in mind, it becomes clear that storage demand will heavily depend on individual grid characteristics and may vary in different regions. Based on Germany as an example, additional short-term storage can be expected at renewable shares between 40% and 60% and long-term storage between 60% and 80%. Above 80% and towards a fully renewable generation, bulk energy storage on all timescales is not only required in order to avoid extensive renewable energy curtailing, ensure grid stability and power quality, but will be a cost-effective solution in the GW range [29]. In less flexible grids, for example utilising large-scale nuclear power to cover the base load, the need for extensive storage will be reached at much lower renewable levels.

An update to the European Green Deal has raised the ambition to reduce greenhouse gas emission by 55% until 2030 compared to the standard of 1990 paving the way for a carbon neutral energy supply by 2050. Consequently, the share of intermittent renewables will need to increase faster. Recent estimates see a growth towards 70% renewable power generation in 2030 [30].

Depending on the flexibility of this share of renewables in different regions, a rapid increase in demand for storage and the provision of AS can be expected with PHS being a promising candidate to fill the gap. For countries with a flat topography, economically viable low-head PHS could bear a huge potential to cover the growing demand. This is especially relevant if a large coastline is available, opening up the possibility for seawater application. Coastal applications also come with the additional benefit of proximity to large-scale IRES, such as offshore wind farms.

2.4. Technological and economic challenges

Low-head PHS has not yet seen deployment on a significant scale within our grids. This is largely due to the increased upfront cost required. While highly dependent on the individual project and site, the major contributor to the initial CAPEX of PHS projects in general are civil structures, including the reservoir, penstock, and lining [31]. Due to larger masses of water being stored in the reservoir and flowing through the penstock when it comes to low-head applications, their contribution to the overall economic viability can only be assumed to be significant. All aspects regarding civil components as well as detailed economic analyses of low-head PHS systems are, however, outside of the scope of this review.

Low-head PHS would be most competitive utilising a storage capacity able to provide balancing in the timescale of hours to days. This places it in the middle between lithium-ion batteries appropriate for shorter and hydrogen storage appropriate for longer periods. The LCOS of new high-head PHS systems ranges from 50 €/MWh to 80 €/MWh [32]. Initially low-head plants may not be able to compete with this. However, changing demand characteristics of the electricity markets, as well as further development and improvement of technological aspects, significantly influence economic viability and thereby the potential of large-scale deployment. The increase in renewables in world-wide grids will lead to rising demands, not just for short- and long-term balancing but also the provision of AS increasing the value of both. Additional revenue from the provision AS could hence increase economic viability.

Further drivers making PHS economically more attractive are growing interconnections to other grids opening up additional markets as well as technical advances such as higher efficiencies across a broader operating range [22]. Technological progression can help facilitate these drivers. A reduction of switching times between pump and turbine mode together with higher power ramp rates will allow for enhanced capabilities to provide AS as well as maximise balancing. Aside from regulatory changes, such as carbon taxation, electricity price margins have been identified as one of the major drivers towards PHS utilisation. Improved round-trip efficiencies directly correlate with higher revenues for the operator and therefore result in increased utilisation [33].

Based on these challenges, three main areas can be identified where significant progress could contribute to making low-head PHS technically and economically competitive. These are pump-turbine design and configuration, grid integration, and electrical machines and control. Research in these fields will be discussed in the chapters following. Additionally, modelling approaches that may aid the development are compared.

3. Pump-turbine design and configuration for low-head pumped hydro storage

The choices when selecting the type of reversible pump-turbine (RPT) unit, or evaluating using a pump as turbine (PAT), are governed by a number of factors. The first thing to evaluate is the power of the hydropower plant, which is a function of head and flow rate and the general formula is given by Eq. (1).

$$P = \rho g H Q \eta \tag{1}$$

Here, ρ is the density of water, g is the gravity acceleration, H is the head, Q is the volumetric flow rate, and η is the overall efficiency of the power plant. The gravity acceleration and water density can be regarded as constant. The equation shows that if the head is low, the flow rate must be large in order to produce high power [34]. With a large flow rate, the diameter of pipelines and the runner need to be large as well to limit the flow velocity, and thus hydraulic losses in the system. High-head conditions are usually preferable to build pump storage hydropower plants. However, low-head solutions with high volumetric flow rate are also regarded as having great potential to unleash new opportunities for pumped hydro storage [35].

The definition of low-head is not unanimous among different countries and researchers. For example, the U.S. Energy Information Administration (EIA) considers low-head when the head is less than 30 metre and Okot [36] classifies it as when $5 < H < 15$ metre. In this work, the European Small Hydropower Association (ESHA) classification defines low-head, and states that low-head hydropower plants have a head of 2-30 metre [37].

The overall efficiency of a low-head power plant is more sensitive to head losses than a high-head alternative, and low-head PHS requires that the pipelines are short to be economically feasible [38]. This is because head losses are proportional to the pipeline length and the flow velocity squared, which is a further incentive for not using ternary units in a low-head case since they require more pipelines and would thus decrease the plant's overall efficiency. With the higher flow rate of high-power low-head PHS, larger reservoirs are required to store the same amount of energy as a corresponding high-head application [34]. This is because the energy storage capacity is a function of the water mass and head. Apart from that, other conditions such as the type of machine (radial-, mixed-, or axial-flow), operation (variable or fixed speed), and reservoir configuration may apply when choosing the best reversible pump-turbine configuration [39]. Chapallaz et al. [40] stated that, in practice, almost any hydro pump can also be used as a turbine. The reverse is, however, not the case. As an example, impulse turbines (Pelton or Turgo) cannot be used as pumps.

The design and characteristics of any hydro pump and turbine are determined by its conditions of operation. In turbomachinery, the specific speed is one key parameter to select the most appropriate reversible pump-turbine or using a pump as turbine (PAT). In this paper, it is defined in accordance with Dixon and Hall [41] as Eq. (2), and Table 1 shows ranges of specific speeds for various machines.

$$\Omega_s = \frac{\Omega Q^{1/2}}{(gH)^{3/4}} \tag{2}$$

Here, Ω is the runner rotational speed in rad/s, Q is the volumetric flow rate in m^3/s, and H is the head in metre. Stepanoff [42] explained in 1948 that a higher specific speed results in a smaller, and thus cheaper, machine. With a higher flow rate, the blade design differs significantly, as illustrated in Fig. 3. On the other hand, machines with low rotational speeds and small shear forces (e.g. Archimedes screw and positive displacement machines) are more fish-friendly [43,44]. Radial- or mixed-flow machines are preferable for pumps with a specific speed of $\Omega_s < 2.7$, and as the specific speed increases ($2.6 < \Omega_s < 11.6$), an axial configuration is more suitable [45].

Carravetta et al. [46] postulate that axial-flow pumps can be used as PAT for heads between 1–5 m and flow rates up to 1000 l/s. They also claim that mixed-flow PATs can be used for heads in the region of 5–15 m and flow rates of 50–150 l/s. Bogenrieder [47] stated that radial pump-turbines are suitable to use for heads that are above 60 metre, with a power exceeding 50 MW. Typically, radial- or mixed-flow machines work best for high heads and low flow rates. For example, regular Francis-like pump-turbines (mixed-flow) are the common choice when it comes to mid- to high-head applications, but the head variations at low-head operation would greatly affect efficiency [48]. Mixed-flow machines can be used as low-head PHS if the flow rate is low. However, according to Eq. (1), this implies that the power will also be low. Multiple machines could be used in parallel to increase the total power. Breeze [48] suggests that a Deriaz, mixed-flow machine can be used for heads between 20–100 m. This is because its design is closer to an axial machine compared to a conventional Francis-like pump-turbine and the Deriaz design also presents adjustable blades [48,49]. Breeze further expresses the necessity of variable speed drives to extend the operational region at high efficiency.

The reason why an axial machine is preferable in a low-head application is that it allows for a higher flow rate, which is necessary

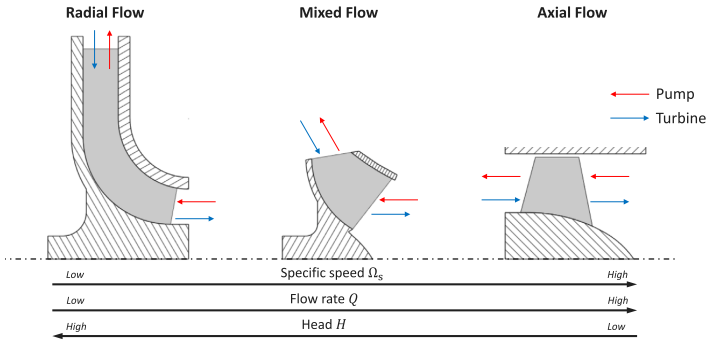

Fig. 3. Principle view of bladed pump-turbine configurations, note that the term "centrifugal" refers to both the radial- and mixed-flow. The drawing is based on principles shown in [40–42,46].

Table 1
Ranges of specific speed for various machines [45].

Technology	Specific speed Ω_s
Axial[a]	2.6–11.6
Mixed	0.6–2.7
Radial	0.1–0.8
Archimedes screw[b]	0.03–0.39
Positive displacement[b]	0.01–0.13

[a]CRPT is classified as an axial machine.
[b]Values should be regarded only as a reference number, since it is not common to indicate a specific speed for these machines.

for a machine with high power at low heads. An axial machine also allows for cheaper civil structures. In turbine mode, the runner rotates due to the torque that is generated by the flow-induced runner blade pressure and suction sides. The electric generator extracts power by a balancing counteracting torque at the particular rotational speed. In pump mode, an electric motor adds power to the runner in the form of torque at the particular rotational speed. A flow is developed due to the rotating runner blade pressure and suction sides, causing a balancing counteracting torque. The pressure change is in an axial machine primarily due to the change of relative flow velocity [45]. This is because the tangential velocity of the runner and the cross-sectional area are constant along a streamline in an axial machine. In a centrifugal machine, the flow must change direction from axial to radial (pump mode), or radial to axial (turbine mode), as shown in Fig. 3. The principles for the head rise in a centrifugal machine are here described in pump mode for brevity. As the flow goes through the machine, the cross-sectional area and the tangential velocity of the runner increase with the radius through the machine. The absolute flow velocity will decrease as the cross-sectional area increases, due to continuity. According to Bernoulli's principle, the static pressure will increase with the change of absolute velocity squared [50]. The main cause of the static pressure rise is, however, due to centrifugal effects caused by the increase of the runner's tangential velocity, and passage diffusion, due to a reduction in the relative flow velocity, through the machine [45]. The result is that the exit blade velocity needs to be small in order to limit the pressure rise in a low-head application. This means that the machine needs to be small and that the entrance-to-exit diameters decrease with the decreasing head [51]. The smaller size further limits the flow rate and thus the power.

In general, pump-turbines are worse at part-load conditions compared to a pure pump or turbine since the pump-turbine design is often a trade-off to reach acceptable performance at design conditions [52,53]. Delgado et al. [54] reported that it is hard to predict part-load performance for PATs, especially in turbine mode since pump manufacturers usually do not supply any data of this. Stepanoff [42] stated that centrifugal machines have preferable efficiency as a function of flow rate; however, axial machines have a flatter efficiency curve as a function of head. This further suggests that an axial machine is preferable in a low-head scenario due to the fact that part-load operations will be less influenced by the large variation in head of a low-head PHS application.

Lately, axial-flow pump-turbines with two runners, rotating in opposite direction from one another, have been proposed as an alternative for low-head PHS. They are usually referred to as counter-rotating pump-turbines (CRPT) due to the rotation of the individual runners, as illustrated in Fig. 4. According to Furukawa [55], the advantages of those machines are that they can be of smaller size, have a more stable head-flow rate characteristic curve, and have a wider range of high efficiency with individual speed control of the runners when compared to a single runner axial machine. Several numerical studies predict that a well designed low-head counter-rotating pump-turbine may achieve efficiencies of up to 80%–90% in both pump and turbine mode [56–58]. Fahlbeck et al. [59] showed numerical results for a prototype counter-rotating pump-turbine in pump mode with a peak efficiency of 91%, heads up to 12 metre, flow rates between 60–160 m^3/s, and a maximum power of almost 14 MW.

Additional non-conventional machines have also been studied as low-head PHS. The Archimedes screw, depicted in Fig. 4, is a viable option for heads between 2–10 m, discharge ranges up to 15 m^3/s, and power output of up to 355 kW [36,43,60]. The Archimedes screw enables lower installation and maintenance costs compared to other conventional pump-turbines and can reach efficiencies of up to 90% in turbine mode [61,62]. An additional benefit is that the Archimedes screw presents better conditions for fish-friendliness when compared to conventional bladed pump-turbines [43,61,63].

Positive displacement (PD) pumps are usually chosen when the system requires low specific speeds [45]. Some PD pumps can also represent a good alternative when reversible flows must be taken into account, thus resembling a PAT [64]. Positive displacement pumps are self-priming, typically produce low flow rates, can handle big variations in head without significantly changing their efficiency, and are often regarded as a good choice for viscous fluids or fluids with the presence of solids or precipitates that need to be handled [45,50]. Rotary positive displacement machines have already been studied as micro hydro turbines in water supply pipelines with pressures up to 5 bar (hydraulic head equivalent to 51 metre) and presented efficiencies between 60%–80% [65–68]. From all the available PD alternatives, the lobe and gear pump configurations – illustrated in Fig. 4 – are the most suitable options to handle reversible flow. Given the low specific speed, PD pumps could most likely be regarded as a fish-friendly technology [44]. On the other hand, only the lobe design seems to handle fish and solid without extra mitigation measures. A few small-scale projects have tested PD RPTs [64]. However, further investigations and real-scale

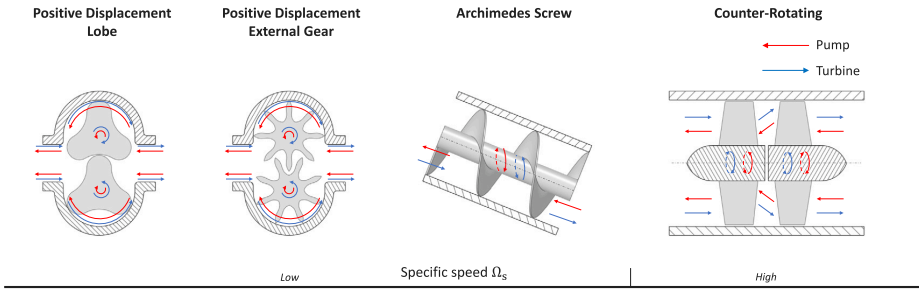

Fig. 4. Principle view of non-conventional pump-turbine configurations. The drawing is based on principles showed in [45,55,56].

prototypes are still needed to validate the use of PD RPTs in low-head pumped storage application.

Pump-turbines in PHS applications can operate at fixed or variable rotational speed. Variable speed machines take advantage of a wider operating range at high efficiency and can thus produce power in a wider spectrum [38,69]. Moreover, variable speed units ensure greater penetration and bring more flexibility to PHS operations, especially for smaller machines [70]. Despite the technical advantages, this technology is about 30% more expensive than fixed speed units. Thus, the choice between the two speed control options relies on both techno-economic and demand aspects [38,70].

4. Grid integration of energy storage systems

A reliable electrical power grid is a balanced system. As generation and demand fluctuate perpetually, transmission system operators (TSO) and distribution system operators (DSO) have to keep the system balance everywhere in the electrical grid. This balance ensures that the grid operates at its nominal frequency (50 or 60 Hz) and that voltage and power load remain within a certain limit at all times. However, the higher the penetration of intermittent renewable energy sources, the more insecure this balance. Thus, the increasing penetration of IRES is a challenge that TSO and DSO have to handle [71,72].

At the present time, power systems rely on conventional power plants utilising synchronous generators contributing significantly to the stabilisation of the electrical power system, using the rotating masses in their generators (rotors). The synchronous generators keep the frequency steady at its nominal value due to their large flywheel masses and thereby assure system stability. In the case of generation or load fluctuation leading to sudden grid frequency deviations, the rotor's combined inertia keeps the generators rotating and consequently supports the grid stability [73]. On the contrary, not all IRES have large rotating masses and most are integrated into the grid via converters, subsequently decoupling the rotating masses from the grid frequency. Therefore, they do not have any natural inertia (spinning reserve) and thus operate in an entirely different way than synchronous generators. As of today, the grid-connected converters for IRES follow the grid frequency by using a phase locked loop (PLL). This tracks the grid frequency in order to keep the IRES converters synchronised to the grid. The PLL control concept is known as grid-following control [73,74].

To tackle the challenge of increasing IRES and decreasing natural system inertia without affecting the system stability, two approaches are feasible. The first is to maintain a minimum number of rotating machines. Among other purposes, the contribution of short-circuit power and voltage support can provide the necessary inertia to the transmission system in a case of disturbances in the grid [75,76]. The second solution is through IRES itself. This occurs by using the capabilities of the power electronics, or energy storage systems (ESS), to provide and ensure a stable grid frequency without any synchronous rotating machines. For this purpose, a grid-forming control mode is currently being developed and tested in many research projects. Here, the

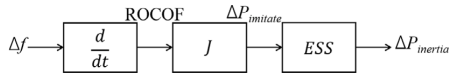

Fig. 5. Simplified block diagram for synthetic electrical inertia control [80,81]. Here, Δf is the deviation of system frequency, ROCOF is the rate of change of frequency, J is the virtual inertia control constant, $\Delta P_{\text{imitate}}$ is the active power of the converter, and $\Delta P_{\text{inertia}}$ is the emulated virtual inertia power that could be imitated into the system.

controlled converter acts as an AC voltage source with stated voltage, phase, and frequency. By controlling the voltage magnitude and frequency, the converter behaves very similar to a synchronous generator. The fundamental difference between grid-following and grid-forming is the way of synchronisation. By applying the swing Eqs. (3) and (4) [77], the grid-forming control strategy calculates the voltage angle and amplitude deviation, using current power transfer. It is thus self-synchronising. Therefore, a converter using grid-forming control coupled with an ESS is currently being discussed as a viable alternative to imitate the synchronous generator's behaviour regarding frequency control, especially its ability to provide synthetic electrical inertia [73,74,78]. In power plants with rotating mass and consequent inertia that are decoupled from the grid frequency, an additional control loop is required that gives a power reference proportional to the derivative of grid frequency. To provide the additional power requested by the synthetic inertia, the plant may still rely on the physical inertia present but due to its decoupled nature depends on said synthetic inertia control.

$$P_{\text{m}} - P_{\text{e}} = J\omega_0 \frac{\text{d}\omega}{\text{d}t} \tag{3}$$

$$\omega = \frac{\text{d}\vartheta}{\text{d}t} \tag{4}$$

Here, P_{m} is the mechanical power, P_{e} is the electrical power, ω_0 is the nominal angular frequency, ω is the output angular frequency, ϑ is the rotation angle, and J is the total moment of inertia of the rotor mass.

Fig. 5 shows a simplified block diagram for a synthetic electrical inertia control system. As illustrated, ESS are needed along the grid-forming control to provide the necessary synthetic electrical inertia. This shows that ESS are an important factor in the energy transition and will play a key role in the future. Energy storage systems will provide inertia for local grid stability as well as other necessary AS, such as steady state voltage control, fast reactive current injections, short-circuit current, black start capability, and island operation capability [79].

Moreover, ESS will also need to compensate for weather and seasonal fluctuations in the power supply from IRES, specially from wind and solar power. For all the previous reasons, ESS are becoming increasingly important. New possibilities for medium and long-term ESS with sufficient storage capacity and flexibility, in accordance with

the respective requirements, are needed to meet the growing demand from IRES. Low-head PHS system is a power generation system and serves at the same time as an ESS. This makes the integration of PHS (low-head or high-head) via grid-forming controlled converter a vitally important milestone of the energy transition in order to provide the necessary storage capacity needed for grid stability and flexibility. The grid integration of low-head PHS via a grid-forming, controlled converter will not only be of great significance for countries with flat topographies such as Denmark, Belgium, and the Netherlands. It will also be essential for countries with a high share of offshore wind energy as these could enable the concept of energy islands.

5. Electric machines and control for low-head pumped hydro storage

5.1. Electric machines

In traditional high-head, high-power PHS, synchronous machines with excitation winding and direct grid connection are used. However, doubly-fed induction machines have been adopted in Europe since 2006 for lower power applications. Doubly-fed induction machines are coupled to a partially rated converter with rotor winding to increase the operating range, which increases turbine efficiency at lower speeds [82]. As can be seen from Eq. (2), RPT operation at low head and high power reduces the nominal rotational speed for a fixed specific speed. Therefore, the power take-off (PTO) in low-head PHS needs to be designed to operate at high efficiency for low rotational speeds. Furthermore, variable speed RPTs require a highly efficient PTO over a wide operating range. Doubly-fed induction machines with a gearbox were the classical choice for such low-speed applications. However, with the recent decrease in cost of power electronics, permanent magnet synchronous machines (PMSM) with a fully rated converter are opted for instead [83–90]. Advantages include a high power density, high efficiency, and controllability over a wide operating range [91,92]. Furthermore, PMSMs with a large pole number avert the use of reduction gearing, which reduces energy losses and increases reliability [93,94]. However, the increased cost of permanent magnets (PM) and converter losses limits its application for high-power installations.

A more recent development in PMSMs is the axial flux PMSM (AF-PMSM), which has a magnetic flux direction parallel to the axis of rotation, in contrast to their radial counterparts. These disc-type machines have a high diameter-to-length ratio, can accommodate high pole numbers, and are suitable for high-torque low-speed applications [95–97]. They have a higher power density and use less core iron, leading to a lower weight [96,98,99], which in turn results in a higher torque-to-weight ratio. The possible topologies are single-stator single-rotor (SSSR), double-stator single-rotor (DSSR), or single-stator double-rotor (SSDR). Furthermore, different concepts can be differentiated on the use of surface mounted or interior PMs, slotted or slotless armature, presence or absence of stator core, concentrated or distributed windings, etc. [100].

Single-stator single-rotor topologies [101] are simple in design and compact. However, there is a strong imbalanced axial force between the stator and rotor. Therefore, the rotor disc width needs to be increased to avoid twisting [96]. Double-stator single-rotor topologies [102] are a valuable alternative to SSDR topologies. Double-stator single-rotor uses fewer PMs, but experiences more copper losses due to poor winding utilisation [96]. A DSSR machine with integrated permanent magnets has a high power-to-inertia ratio, since the rotor disc serves no magnetic purpose and is eliminated [100]. The reduced inertia is a significant benefit in a grid-supporting low-head PHS. In a slotted stator AF-PMSM, cogging torque results from the interaction between the PMs and the stator slots. This undesired torque can be significantly reduced by changing the angle between both stators [103]. However, this also reduces power output. Finally, SSDR is deemed the most favourable AF-PMSM topology. Next to decreased copper losses, the use of a stator yoke and the corresponding iron losses can be averted. This can be achieved by using a north–south PM arrangement of the rotors. Then, the flux path is completely axial, obviating the magnetic function of the yoke. The single-stator double-rotor topology has already been adopted in wind and tidal turbine applications [104,105]. An SSDR with coreless stator maximises efficiency, while averting cogging torque and torque ripple [106–108]. Since the flux path is axial, grain-oriented material – which has greater magnetic permeability in one direction – can be used in the stator slots. This results in significantly lower iron losses compared to non-oriented material [109], while reducing PM use compared to coreless alternatives [100].

Especially in high-voltage electric machines, the vast majority of occurring faults are stator faults, followed by rotor and bearing faults [110]. Therefore, AF-PMSMs with concentrated windings can offer a significant advantage by adopting a Modular Machine Drive (MMD) design. If a fault arises in one of the stator windings, the MMD can compensate this with the other modules and remain functional albeit the maximum power is reduced [111,112]. This fault-tolerant design improves the reliability of the electric machine, which is a considerable advantage for a low-head PHS system providing grid support. The reliability can be further increased by means of condition monitoring techniques and fault or anomaly detection methods [113,114]. Thanks to the drastic increase in computational power in the past years (both local and in the cloud), these techniques have become more data-driven, relying on, e.g., machine learning [115,116], including artificial neural networks [117], support vector machines [118], and deep learning [119,120]. The use of digital twins for predictive maintenance of mechanical components [121] or the full drivetrain [122] shows promising results and offer a perspective for the future of condition monitoring [123]. These techniques can be applied on the electric machine, and in extension on the whole drivetrain. Current, voltage, magnetic flux, speed, temperature, and vibration signals can be captured on the electric machine and serve as inputs for the condition monitoring system.

It can be concluded that the PMSM is currently the most sensible electric machine technology for modern low-head PHS due to its high efficiency and direct-drive capability, although the use of rare earth materials is a drawback. The principles of axial flux design, modularity for fault tolerance and data-driven condition monitoring are likely to play a role in the further improvement of the PMSM.

5.2. Torque and speed control

In variable speed PHS, the machine speed is altered to reach a power setpoint as fast and precise as possible, both in pump and turbine mode. Therefore, the machine torque must be precisely controlled. Field oriented control (FOC) is a vector control method that has been widely used in low-head micro-hydropower installations [83–89]. The main advantage is an independent control of the machine torque, and thus, highly dynamic performance. This is necessary in PHS to quickly react to changes to the rapidly fluctuating grid frequency. The general principle of FOC is to regulate the i_d and i_q currents in the rotating reference frame. The electrical dynamics of a PMSM can be modelled by Eqs. (5) and (6). Here, $\Omega_e \Psi_{PM}$ is the back-EMF of the permanent magnets. R is the stator resistance. L_q and L_d are the q and d axis inductances, respectively. $\Omega_e L i$ is the armature reaction EMF, through which the q and d schemes are coupled.

$$v_d = R\, i_d + L_d \frac{di_d}{dt} - \Omega_e L_q i_q \tag{5}$$

$$v_q = R\, i_q + L_q \frac{di_q}{dt} + \Omega_e (L_d i_d + \Psi_{PM}) \tag{6}$$

By regulating the d and q axis currents, the torque can be regulated as shown in the general torque Eq. (7) of the PMSM.

$$T = p\, \frac{3}{2} \left[\Psi_{PM} i_q + (L_d - L_q) i_d i_q \right] \tag{7}$$

95

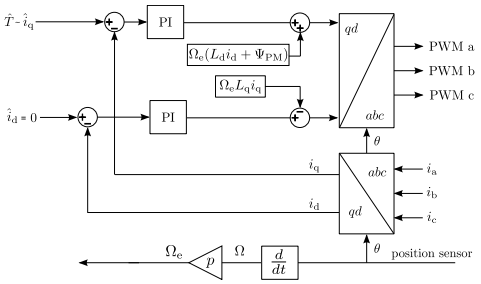

Fig. 6. Decoupled field oriented control of a PMSM with estimated back-EMF feedforward.

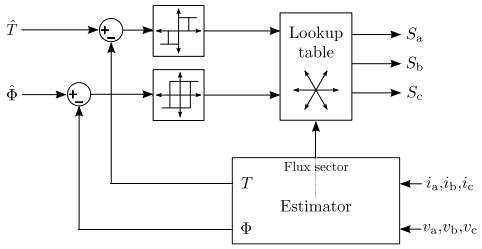

Fig. 7. Control schematic of DTC.

Here, p is the pole pair number and Ψ_{PM} is the constant flux of the permanent magnets. Fig. 6 shows the control scheme of a field oriented controlled PMSM. On the bottom right, the stator currents are measured and transformed to the rotating q, d reference frame. These signals are compared with the setpoints on the left and controlled by two PI controllers. These controllers determine the duty ratios resulting in the Pulse-Width Modulated (PWM) signals for the converter. In FOC, $\hat{i}_d$ is set to 0. Eq. (7) shows that the machine torque is directly proportional to i_q, resulting in a highly dynamic control. To achieve decoupled control of both currents, the coupling terms in Eq. (7) are used as a feedforward. Furthermore, a back-EMF estimator can be implemented in the q current control.

Although FOC is highly dynamic and easy to implement, setting $i_d = 0$ is not the most efficient way to reach a desired torque setpoint for a PMSM with saliency, like an interior magnet PMSM. Therefore, maximum torque per ampere (MTPA) control can reduce copper losses and increase overall efficiency in low-head hydropower applications. The MTPA accomplishes this by minimising $i_s = \sqrt{i_q^2 + i_d^2}$ for every torque setpoint [124]. Applications with interior magnet PMSMs in wind turbines found a reduction in Joule losses (up to 4.2%), while maintaining a dynamic response to changing torque setpoints [124,125].

The position sensor plays a critical role in FOC. However, a position sensor is costly and its signal can contain noise. Therefore, saliency-based sensorless rotor position estimators [88,89,126,127] are proposed for low-power systems, since they can increase reliability and reduce cost [89]. For low rotational speed runners, as in low-head PHS, the saliency-based approach is the most suitable [89]. Here, a high pulse frequency is injected, while the current response, which depends on the rotor magnetic flux position, is observed.

Active distribution rejection control (ADRC) is used in torque and speed control to account for known and unknown electrical, hydraulical, or mechanical disturbances in the system, increasing performance and robustness. Guo et al. [84] applies a first order ADRC for a PMSM in a hydropower application, where the known disturbances are mechanical friction and hydraulic torque. A second order state observer is used to estimate the rotational speed and hydraulic torque. ADCR is especially useful in low-head high-power PHS, since any change in the system tubes has a significant influence on the head losses, because of the high flow rate at low head.

Direct torque control (DTC) is an alternative control method to FOC. In DTC, the electromagnetic torque and stator flux are controlled by switching between a discrete number of stator voltage vectors, which in turn form the stator flux vector interacting with the rotor flux. Based on the torque and flux linkage reference and the current flux vector position, a lookup table is consulted to select the optimal voltage vector. If e.g. the torque must be increased, a voltage vector is selected so that the angle between stator and rotor flux is increased. Fig. 7 visualises the control schematic. To find the torque and stator flux, an estimator based on phase voltages and currents is used (bottom). These estimated values are compared to torque and flux setpoints. Hysteresis controllers then determine the proper voltage vector from a lookup table, resulting in the switching signals. Direct torque control has a slightly better torque response compared to FOC and does not require a position sensor [128,129]. However, DTC relies on an accurate estimator. Especially at low speeds, an estimator based on phase voltages and currents cannot accurately estimate the stator flux [130] which makes it less suitable for low-head PHS. Although some improved estimator algorithms have been studied [130], this drawback is best averted by using a position sensor in the estimator. Disadvantages of DTC include variable switching frequency, high harmonic current distortion, and torque ripple [128,129,131]. To achieve a smoother dynamic response and thus less torque and flux ripple, space vector modulation (SVM) is used instead of the lookup table [128,129,132].

5.3. Power control

In the power control of low-head PHS, the goal is to reach a power setpoint as fast and efficiently as possible. Three main control parameters are determined: the pump/turbine rotational speed Ω; the inlet vane angle α; and the blade pitch β. An RPT with only Ω as control parameter is defined as a non-regulated RPT. A single- and double-regulated RPT further include, respectively inlet vane control, and inlet vane and blade pitch control. In low-head PHS, a regulated RPT is recommended, because it allows the RPT to be operated at high efficiency in a large operating range of heads, flow rate, and power setpoint.

5.3.1. Maximum power point tracking algorithms

Maximum power point tracking (MPPT)-based algorithms are used to find the optimal speed setpoint for a certain power setpoint in turbine mode. In a low-head turbine, this power setpoint is the maximum available power, hence the name MPPT. In grid-supporting PHS, this may not be the case, as the power setpoints depend on grid frequency. Therefore, adjustments need to be made to the existing algorithms. The MPPT algorithms can be divided into direct and indirect methods. Direct MPPT algorithms are based on iterative extremum-seeking control algorithms. These algorithms require limited knowledge of the system, but are inherently slow due to their iterative behaviour, making them less suitable for grid-supporting PHS. However, they can still be used in storage systems with lower dynamic requirements because of their simplicity. Indirect methods are based on a model of the system, making them more dynamic but less flexible. Most of the existing MPPT control methods rely on flow rate measurement. However, a flow rate sensor is costly and has a certain error. In low-head RPTs, the accuracy can further decrease due to a non-uniform flow, a short intake, and high turbulence [133]. To evade these drawbacks, Borkowski and Dariusz [90] presented a flow rate estimator. The estimator is based on an artificial neural network (ANN), which is trained by experimental data.

96

Among direct MPPT control methods, the perturb and observe algorithm has been investigated for non-regulated low-head turbines. The principle operation consists of altering or perturbing the rotational speed Ω, i.e. accelerating or decelerating, and analysing the change in output power P, measured at the electric machine or converter. If the power has increased, the sign of $\mathrm{d}\Omega$ is maintained and the procedure continues. Otherwise, $\mathrm{d}\Omega$ is reversed [83]. Eq. (8) shows how the speed setpoint $\hat{\Omega}$ is altered after each iteration. Note that $\delta(t)$ implies the sign of $\mathrm{d}\Omega$.

$$\hat{\Omega} = \int_{t_{k-1}}^{t_{k-1}+T_s} K\delta(t)\ \mathrm{d}t \tag{8}$$

$$\delta(t) = \mathrm{sgn}(P_k - P_{k-1})\ \mathrm{sgn}(\Omega_k - \Omega_{k-1}) \tag{9}$$

Inherent to this method is that the system will still perturb Ω when the MPP is reached, resulting in an oscillation around the MPP. Step size K is an adaptive value that increases when the power is continuously rising and decreases when the power is fluctuating [83]. However, the dynamic behaviour of this method is not optimal. If K is too low after oscillations and the MPP shifts, the dynamic response is poor. To allow both dynamic response and minimal power fluctuation around the MPP, K can be taken proportional to the power gradient $\frac{\Delta P}{\Delta \Omega}$ [134]. Due to the parabolic nature of the turbine characteristics, K is high when far away from the MPP and gradually decreases when the MPP is neared. Note that using this gradient-based step size cannot be used to reach a lower power setpoint $\hat{P}$. However, the step size here can be proportional to $|\hat{P} - P|$. In wind turbine applications, fuzzy logic is recently used to find the value of K, where the perturbed variable is the generator voltage, which is proportional to the generator speed [135–137].

Gradient descent control is a direct maximum efficiency point tracking (MEPT) algorithm that allows multiple control variables, opposed to the perturb and observe algorithm. However, to derive the efficiency, an accurate flow sensor is necessary, which was discussed to be a challenge in low-head PHS systems [133]. On every operating point, the control variables are incremented with the direction of their partial derivatives of efficiency at the current operating point, multiplied by a step size k [138]. In Eq. (10), α is the vane opening and β is the blade pitch.

$$\Delta\alpha = k\frac{\partial\eta}{\partial\alpha} \quad \Delta\beta = k\frac{\partial\eta}{\partial\beta} \quad \Delta\Omega = k\frac{\partial\eta}{\partial\Omega} \tag{10}$$

If the time constants of the control parameters are known, k can be chosen differently for each control parameter. Furthermore, k can be adaptive and defined by a line search algorithm at every iteration [139]. Although this control algorithm shows great potential, any disturbances on the gradient estimation due to measurement error or mutual influence between control parameters has a great impact on the convergence [138]. Therefore, a moving average filter and a Kalman filter can, respectively, be used to increase robustness [90,140]. Furthermore, Borkowski [90] accounts for the time delay of flow rate settlement after a change in turbine control parameter further reduce risk of a non-converging control.

Indirect MPPT algorithms rely on prior knowledge of the system in order to determine the optimal torque or speed reference to achieve a power setpoint. Recently, this system knowledge is mostly captured in the form of empirical equations, hill charts, or lookup tables, which are derived from measurements or numerical analysis like computational fluid dynamics. Márquez et al. [141] derived an empirical formula for a propeller turbine, which is a modified Kaplan turbine, designed for low-heads and low flow rates. Eq. (11) relates the non-regulated turbine efficiency to flow rate and turbine speed.

$$\eta_h(\Omega, Q) = 3.33\ Q\left[\frac{1}{2}\left(\frac{90}{\lambda_i} + Q + 0.78\right)e^{\frac{-50}{\lambda_i}}\right] \tag{11}$$

$$\lambda_i = \left[\frac{1}{(\lambda + 0.089)} - 0.0035\right]^{-1}, \quad \lambda = \frac{RA\Omega}{Q}$$

Although this model can be used in low-head control models, it is important to note that flow rate Q is a function of head and rotational speed $Q = f(H, \Omega)$ for a non-regulated RPT. Therefore, changing Ω will affect flow rate Q as well. Zhang et al. [142] proposes a polynomial empirical equation for the efficiency of a turbine $\eta_h(\Omega, Q)$, where the coefficients can be derived from experimental data. Borkowski and Dariusz [143] used an ANN to compose and validate an efficiency equation $\eta_h(\Omega, Q)$ together with a flow rate characteristic $Q(\Omega, \alpha)$ for a regulated turbine. The control system based on these characteristics requires no flow rate sensing. However, the Q characterisation is for a constant head and the flow rate is approximated by a linear function of speed. This limits its application under varying head at low rotational speeds.

Similarly, ANN has also been used to form lookup tables [144]. Lookup tables can be constructed over a large operating range during on-site measurements or by using an existing dataset. Pérez-Diaz and Fraile-Ardanuy [144] use two ANNs to train the head and efficiency for input parameters Q, Ω, and α. A possible application of the resulting lookup tables is to find reference $\hat{\Omega}$ and $\hat{\alpha}$ to reach the optimal efficiency for a given head. In this control system, no flow sensor is necessary, thus reducing cost and increasing reliability, especially for low-head systems.

Hill charts define the relation between flow rate Q, rotational speed Ω, inlet vane angle α, and efficiency η for a constant head H. Therefore, if Ω and α are known, Q and η can be read from the graph. Furthermore, α and η are plotted versus the unitary rotational speed Ω_{11} and unitary flow rate Q_{11} in Eq. (12), making hill charts scalable for different heads. However, in a real system, the losses $H_L(Q)$ have to be taken into account, making it difficult to estimate the net head across the turbine without a flow rate sensor. Especially in a low-head high-power system, where the flow rate is high, these losses have a significant influence on the efficiency.

$$\Omega_{11} = \frac{\Omega\, D}{\sqrt{H}}, \quad Q_{11} = \frac{Q}{D^2\sqrt{H}} \tag{12}$$

Q_{11} and Ω_{11} can also be compensated when the Reynolds number of the real system differs from the design [145]. Fraile-Ardanuy et al. [146] applied a hill chart to a control system in order to find the optimal efficiency speed for given α and measured Q. For a reduced-scale RPT [147], a lookup table is trained based on measurements. The lookup table is used to find $\hat{\Omega}$ for given measured H and $\hat{P}$. However, the speed is controlled by α, while it was shown in the paper that $Q_{11} = f(\alpha, \Omega)$. However, the proposed control system is promising for low-head hydropower if both Ω and α are controlled separately. Then, the RPT could be controlled to reach $\hat{P}$ at the highest efficiency for a certain measured H.

One drawback of using turbine characteristics is that the electrical machine and converter losses are not included. Therefore, the overall MPP may differ from the turbine MPP [87]. De Kooning et al. [148] found that the MPP displacement in wind turbines was greater for low wind and thus lower rotational speeds. In direct MPPT methods, these losses are included if the power is measured on the converter side. Another drawback of indirect MPPT methods is that they do not account for system performance deterioration over a long time period. However, reinforcement learning, as proposed for wind turbines [149,150], can solve this problem at the cost of a higher real computational intensity.

5.3.2. Model predictive control

An important factor in RPT operation and control that is often overlooked in traditional MPPT strategies is the transient effect of the water supply system caused by a control action. The transient flow equations are described in Section 6.1. Fang et al. [151] stated that increasing the control action magnitude actually decreased the output power, while the settling and maximum turbine pressure deviation increased. Therefore, it can be seen how using an MPPT control that does not account for these effects can have poor dynamic behaviour

when applied to a real system. In some studies on MPPT control, the water inertia time T_w is incorporated as a time delay on the control action [90] or as an extra mechanical inertia on the RPT [152]. However, this does not fully capture the transient effects. Therefore, model predictive control (MPC) is applied to PHS systems [153–155]. In MPC, a detailed model of the full PHS system, including hydraulic transients, losses, and an RPT model, are used. Based on a certain operating state setpoint, an internal optimisation algorithm simulates control actions and observes the predicted outcomes of the model. The outcomes are then given a cost value based on the power response. These predictions are made for multiple future time samples. Each time sample, this process is repeated. Therefore, MPC is an accurate control method that can work on complex systems, at the cost of a significantly high computational intensity. Furthermore, MPC can also incorporate system constraints, such as maximum pressure deviation and mechanical rate limits. Chaoshun et al. [153] proposed using a nonlinear MPC, which includes the elastic water hammer effect in a high-head PHS plant. Liang et al. [154] used MPC to define the optimal switching time between pump and turbine mode for a multi-RPT PHS plant. However, these studies did not include pressure constraints, which are especially important in systems with long pipelines. The MPC for a 40 metre PHS plant by Mennemann et al. [155] included this effect. MPC is currently mostly investigated for high-head PHS. However, the benefits of adapting MPC for low-head PHS could be substantial, because of the potentially increased influence of transient effects, as described in Section 6.1. For a dynamic system providing frequency support, the MPC's computational intensity increases even further, which might slow down the optimisation algorithm. However, with the recent advancements made in parallel computing with, e.g., multi-core processors (CPUs) and many-core processors such as graphical processing units (GPUs), the MPC process can be accelerated [156], making it suitable for complex dynamic systems like low-head PHS.

6. Modelling of low-head systems

The overall objective of developing a model of a given system is to have a representation of the real world. Since such a model will always be a simplified depiction, it is crucial to weigh which aspects are essential and what should be left out or simplified. In the case of numerical models, this also helps to improve performance and reduce the computational resources necessary. At the end, a well formulated model allows to predict the behaviour of a system to a greater extent and wider scenarios than experiments and interpolating empirical data. These predictions are crucial in developing such systems to understand performance and dynamics, aid optimisation, and can be required for accurate control during operation. The mathematical models are typically derived from first principles, such as balance equations of mass, energy, or momentum, but can also be based on phenomenological or empirical observations or a mixture of both.

Models for high-head PHS are comprehensive and well researched while attention to low-head PHS applications has been limited. Fundamentally, the same approaches can be used. There are, however, differences in the relevance of individual model components. From a hydrodynamic point of view, the major difference is a shift towards higher flow and reduced head for a given power. The increase in the mass flow rate of water may cause the system to be more prone to water hammer effects. Cavitation is a further effect to consider when choosing model components for a low-head scenario. Reaction turbines, such as Francis or Kaplan turbines that are suitable for medium- and low-head applications, are considered more susceptible to the effect [157].

The different relation between flow and head also affects turbomachinery and power take-off. The shift to a higher flow and lower pressure at the machine side closer to the upper reservoir typically results in lower angular velocity and higher torque at the runner and motor-generator. This is due to an increased runner tip speed as a consequence of enlarged machines. In combination with the likely use of variable speed control which may cause even lower speeds at off-design operation points, this may, for example, not just affect the choice of motor-generator architecture but could also affect the drivetrain losses. When choosing modelling approaches for individual system components, considering these characteristics specific for low-head PHS helps to cover the relevant aspects while also optimising performance.

6.1. Hydrodynamics

One of the most common approaches in PHS is to model the penstock as a rigid conduit in addition to the consideration of water being an incompressible fluid. A widespread approach making these assumptions is based on the net force on the body of water which can be given through both the rate of change of momentum and the differences in pressure head to obtain the change in time of the volumetric flow rate as shown in Eq. (13) [158–160].

$$L\frac{\mathrm{d}Q}{\mathrm{d}t} = \left(H - H_\mathrm{T} - H_\mathrm{L}\right) Ag \tag{13}$$

Here, Q is the volumetric flow rate through the conduit and turbine, H is the head over the body of water, H_T is the turbine head, H_L represents the head losses within the conduit, g is the gravitational acceleration, A is the conduit cross-sectional area, and L is the conduit length. The turbine head can be obtained either from empirical data or physical models as a function of both its rotational speed and flow rate, while the major and minor head losses are typically represented through well known hydraulic models, such as the Darcy–Weisbach formulation in combination with the Colebrook equation [50]. To complete the conduit component of the system model, these equations are typically coupled with equations relating to a governor, such as a gate or guide vanes and mechanical power of the turbine as given in Eq. (1).

Using the above mentioned combination of ordinary differential and algebraic equations to model the water column as a rigid body is one the simplest methods to cover the system dynamics. However, to accurately depict transients in the system, such as travelling pressure waves, an approach using coupled partial differential equations considering compressibility and elasticity is required [161]. This could be particularly relevant in applications where enlarged mass flow rates of water are subject to sudden changes of flow rates and heads, such as low-head PHS. A commonly used 1-D approach considering these effects uses the so-called, water hammer equations. These relate pressure head and water velocity as a function of position and time as shown in Eqs. (14) and (15) [162,163].

$$\frac{\partial H}{\partial t} = -U\frac{\partial H}{\partial x} - \frac{a^2}{g}\frac{\partial U}{\partial x} \tag{14}$$

$$\frac{\partial U}{\partial t} = -U\frac{\partial U}{\partial x} - \frac{fU|U|}{2D} - g\frac{\partial H}{\partial x} \tag{15}$$

Here we have H as the pressure head, U as water velocity, a as the pressure wave velocity, g as gravitational acceleration, D as the conduit diameter, and f as friction factor. If appropriate, simplifications can be made neglecting velocity head or friction losses. The set of partial differential equations can be solved either directly or by transforming it first into a series of ordinary differential equations.

Comparisons of similar approaches have shown that treating the conduit as rigid results in a reduction in computational resources necessary and hence, decreased simulation time. However, if the underlying scenario requires, higher accuracy can be achieved when considering elasticity and compressibility effects [163,164].

Aside from travelling pressure waves, another effect that may be of higher relevance in a low-head high-flow system is cavitation. The inception of cavitation is dependent on the amount and type of particles in the water allowing for nuclei to sustain [165]. Low-head PHS is a promising candidate for seawater applications in coastal regions. In such, breaking waves mixing particles from the seabed with the salty water could increase the risk for cavitation to occur. Its likelihood is

also increased when pump-turbines work at off-design conditions as a consequence of variable speed operation.

This formation of vapour bubbles occurs when the local reference pressure in the fluid reaches its vapour pressure. Fundamental numerical estimates for the likelihood of cavitation occurrence use different forms of a dimensionless cavitation parameter, such as *Thoma's* cavitation number shown in Eq. (16) [166].

$$\sigma = \frac{p_r - p_v(T)}{\Delta p} \tag{16}$$

Such cavitation numbers characterise how close the local reference pressure is to the vapour pressure of the fluid. It is calculated from the reference pressure p_r, the vapour pressure at the given temperature $p_v(T)$, and the characteristic system pressure difference Δp. Approaches using various forms of the cavitation number have shown widespread use in a variety of hydrodynamic applications. It has been found, however, that studies giving too much emphasis to it, result in poor repeatability and inconsistency between them. This is due to a wide variety of definitions of the cavitation number as well as the neglect of other factors, such as the influence of geometry, flow velocity, or fluid temperature [167]. More accurate approaches typically include representations of the dynamics of the vapour bubble cluster. While computationally more intensive, these allow to model growth and collapse of the nuclei based on the Rayleigh–Plesset equation derived from the conservation of mass allowing to solve for the time-dependent vapour bubble radius [168,169].

6.2. Power take-off

Variable speed operation of PHS does not just enable to work at improved efficiency under varying conditions but also improves the capability to provide AS. When modelling newly developed low-head PHS systems, this should be considered. For variable speed systems in low-head PHS as well as related and comparable wind power generation, a variety of power take-off architectures and controls are available. Commonly used are models representing doubly-fed induction or permanent magnet synchronous motor-generators, respectively, in combination with drivetrain models of the change in angular velocity based on torque balance and inertia [161,170,171]. To model the drivetrain, the simplest model consider a lumped rigid body approach with a rigid shaft such that all rotating masses and hence rotational inertias can be added together, leading to Eq. (17).

$$J \frac{\mathrm{d}\omega}{\mathrm{d}t} = \tau_h - \tau_g - D_f \omega \tag{17}$$

This ordinary differential equation relates the change in angular velocity ω and rotational mass moment of inertia of the system J to the balance of hydraulic torque τ_h, generator torque τ_g, as well as friction typically represented as a viscous damping torque $D_f\omega$. Typical implementations modelling the electrical dynamics of motor-generators use space-vector representation with the d-q frame of reference. An example for such an approach for a PMSM can be found in Eqs. (5) and (6) described in Section 5.2.

A further point of interest to modelling the PTO of low-head PHS in combination with variable speed operation is a potential shift to higher Joule and reduced iron losses. The changing loss characteristics could affect control and supporting models when tracking optimal operating point to extract maximum power as shown on the example of wind turbines [172]. Effects that are potentially less relevant for low-head applications are the influence of cogging torque and resulting speed ripple. The shift towards lower angular velocity and increased torque for a given power means cogging will be a smaller fraction of the total torque. Additionally, larger diameters of the rotating mass lead to increased rotational inertia. An increase here correlates with a reduction in speed ripple [173]. This becomes clear when including a cogging torque in Eq. (17).

7. Conclusion

Due to the rapid rise of intermittent renewable energy sources, penetration levels will exceed what can be compensated for by alternative stability measures, and large-scale integration of energy storage will become imperative. This increase in demand for short- and long-term balancing and the provision of ancillary services will contribute to novel systems turning into cost-effective solutions. While pumped hydro storage is a promising candidate to improve grid stability, its limitations in deployability call for a conceptual adaptation. Shifting the operating range from traditional high-head towards low-head applications could pave the way to utilise PHS in regions where so far it had not been feasible. Further technological advancements can significantly contribute to enhancing its capability to improve grid stability while also making it cost competitive. Based on the lack of research on low-head PHS, this review discusses challenges and the potential of low-head PHS while giving an overview of pumped storage technologies and their applicability to low-head applications. The main outcomes are the following:

- In a low-head context, the choice of pump-turbine design is highly dependent on the flow rate of the system. Axial flow pump-turbines, with variable speed drives, are the most suitable solution for high flow rates which leads to higher power outputs. On the other hand, other designs, such as Archimedes screw or rotary positive displacement configurations, can be beneficial at lower flow rates and micro- or small-scale locations.
- The discussion on grid integration has shown that, to compensate for an increase in intermittent generation and a reduction in spinning reserves, a combination of grid-forming control alongside bulk energy storage is necessary. To ensure grid stability, such systems will need to provide synthetic inertia next to other ancillary services, namely steady state voltage control, fast reactive current injections, short circuit currents, black start, and island operation capability.
- For the power take-off, axial flux PMSMs are the most promising electric machines for low-head PHS due to their high efficiency, high power density, and suitability for high-torque-low-speed operation. The machine torque can be controlled to achieve a speed setpoint by either field oriented control or direct torque control, with the latter having a slightly better torque response if a position sensor is used, but increasing torque ripple. Active distribution rejection control can be used to complement the torque and speed control, increasing performance and robustness. To derive the speed setpoint, MPPT algorithms based on RPT models are suitable for low-head PHS because of their short response time and steady power output. However, it is important to include the whole system with its losses to have precise control. Model predictive control is a computationally intense control method that can account for transient effects in complex systems, making it a valuable option for low-head PHS.
- When modelling low-head PHS, the same fundamental approaches of traditional PHS can be used. However, the change in system characteristics being a shift to larger masses of water and reduced head requires more attention on certain model components. Modelling hydrodynamics in more detail allows to cover transients such as water hammer and estimate the risk of cavitation. Paying further attention to changing motor-generator dynamics can help to accurately predict performance and improve control.

There are considerable opportunities for further research to improve low-head pumped storage technology and facilitate economic viability. Firstly, a detailed economic analysis incorporating a predicted increase in revenue from energy arbitrage and the provision of AS combined with improved control strategies optimised for these may serve as a further proof of concept. Additionally, modelling and simulation efforts integrating the proposed components and analysing performance on

a system level can help to estimate technical potential for round-trip efficiencies, mode-switching times, and power ramp rates. Finally, a step from such theoretical results to prototyping and implementation would attract attention of stakeholders and pave the way for large-scale deployment. With these steps taken, low-head PHS has the potential to be a significant facilitator for the ongoing energy transition.

Declaration of competing interest

The authors declare that they have no known competing financial interests or personal relationships that could have appeared to influence the work reported in this paper.

Acknowledgements

This research is part of a project that has received funding from the European Union's Horizon 2020 research and innovation programme under grant agreement No. 883553. The authors would like to thank the International Hydropower Association for providing us with Fig. 2.

References

[1] International Energy Agency. Global energy review 2021. Global energy review 2020. 2021, p. 1–36.
[2] International Energy Agency. Renewables information - overview (2020 edition). IEA Stat 2020;497.
[3] Jülch V. Comparison of electricity storage options using levelized cost of storage (LCOS) method. Appl Energy 2016;183:1594–606.
[4] Barnhart CJ, Benson SM. On the importance of reducing the energetic and material demands of electrical energy storage. Energy Environ Sci 2013;6(4):1083–92.
[5] REN21. Renewables 2021 global status report. 2021.
[6] Rehman S, Al-Hadhrami LM, Alam MM. Pumped hydro energy storage system: A technological review. Renew Sustain Energy Rev 2015;44:586–98.
[7] Richter W, Vereide K, Pikl FG, Pummer E. Economic and sustainable energy transition enabled by pumped-storage hydropower plants. 2020, p. 1–10.
[8] IHA. Hydropower status report 2020. International Hydropower Association; 2020, p. 1–44.
[9] Rogner M, Law S. Pumped storage tracking tool. International Hydropower Association; 2021.
[10] Koohi-Fayegh S, Rosen MA. A review of energy storage types, applications and recent developments. J Energy Storage 2020;27:101047.
[11] Wissenschaftliche Dienste des Deutschen Bundestages. Vor- und Nachteile verschiedener Energiespeichersysteme. 2014.
[12] Statkraft Markets GmbH. Speicherlösungen für den Energiemarkt der Zukunft.
[13] Ren J, Ren X. Sustainability ranking of energy storage technologies under uncertainties. J Clean Prod 2018;170:1387–98.
[14] Stocks M, Stocks R, Lu B, Cheng C, Blakers A. Global atlas of closed-loop pumped hydro energy storage. Joule 2021;5(1):270–84.
[15] Blakers A, Stocks M, Lu B, Cheng C. A review of pumped hydro energy storage. Prog Energy 2021;3(2):022003.
[16] Barbour E, Wilson IA, Radcliffe J, Ding Y, Li Y. A review of pumped hydro energy storage development in significant international electricity markets. Renew Sustain Energy Rev 2016;61:421–32.
[17] Joseph A, Chelliah TR, Lee SS, Lee K-b. Reliability of variable speed pumped-storage plant. Electronics 2018;7(10).
[18] Ardizzon G, Cavazzini G, Pavesi G. A new generation of small hydro and pumped-hydro power plants: Advances and future challenges. Renew Sustain Energy Rev 2014;31:746–61.
[19] Kougias I, Aggidis G, Avellan F, Deniz S, Lundin U, Moro A, et al. Analysis of emerging technologies in the hydropower sector. Renew Sustain Energy Rev 2019;113:109257.
[20] Javed MS, Zhong D, Ma T, Song A, Ahmed S. Hybrid pumped hydro and battery storage for renewable energy based power supply system. Appl Energy 2020;257(May 2019):114026.
[21] Bódis K, Monforti F, Szabó S. Could Europe have more mini hydro sites? A suitability analysis based on continentally harmonized geographical and hydrological data. Renew Sustain Energy Rev 2014;37:794–808.
[22] Deane JP, Ó Gallachóir BP, McKeogh EJ. Techno-economic review of existing and new pumped hydro energy storage plant. Renew Sustain Energy Rev 2010;14(4):1293–302.
[23] Puchta M, Bard J, Dick C, Hau D, Krautkremer B, Thalemann F, et al. Development and testing of a novel offshore pumped storage concept for storing energy at sea - Stensea. J Energy Storage 2017;14:271–5.
[24] Pradhan A, Marence M, Franca MJ. The adoption of seawater pump storage hydropower systems increases the share of renewable energy production in small island developing states. Renew Energy 2021;177:448–60.
[25] Berrada A, Loudiyi K, Zorkani I. System design and economic performance of gravity energy storage. J Clean Prod 2017;156:317–26.
[26] Feltes J, Kazachkov Y, Gong B, Trouille B, Donalek P, Koritarov V, et al. Modeling ternary pumped storage units. 2013.
[27] Fisher RK, Koutník J, Meier L, Loose V, Engels K, Beyer T. A comparison of advanced pumped storage equipment drivers in the US and Europe. 2012.
[28] Nicolet C, Béguin A. Variable speed and ternary units to mitigate wind and solar intermittent production. 2014.
[29] Sterner M, Stadler I. Handbook of energy storage. 2019.
[30] European Environment Agency. EU Renewable electricity has reduced environmental pressures; targeted actions help further reduce impacts. 2021, p. 1–14.
[31] Foley AM, Leahy PG, Li K, McKeogh EJ, Morrison AP. A long-term analysis of pumped hydro storage to firm wind power. Appl Energy 2015;137(2015):638–48.
[32] Zakeri B, Syri S. Electrical energy storage systems: A comparative life cycle cost analysis. Renew Sustain Energy Rev 2015;42:569–96.
[33] Kougias I, Szabó S. Pumped hydroelectric storage utilization assessment: Forerunner of renewable energy integration or Trojan horse? Energy 2017;140:318–29.
[34] Hunt J, Byers E, Riahi K, Langan S. Comparison between seasonal pumped-storage and conventional reservoir dams from the water, energy and land nexus perspective. Energy Convers Manage 2018;166:385–401.
[35] McLean E, Kearney D. An evaluation of seawater pumped hydro storage for regulating the export of renewable energy to the national grid. Energy Procedia 2014;46:152–60.
[36] Okot DK. Review of small hydropower technology. Renew Sustain Energy Rev 2013;26:515–20.
[37] Loots I, Van Dijk M, Barta B, Van Vuuren SJ, Bhagwan JN. A review of low head hydropower technologies and applications in a South African context. Renew Sustain Energy Rev 2015;50(2015):1254–68.
[38] Hunt JD, Zakeri B, Lopes R, Barbosa PSF, Nascimento A, Castro NJd, et al. Existing and new arrangements of pumped-hydro storage plants. Renew Sustain Energy Rev 2020;129:109914.
[39] Vasudevan KR, Ramachandaramurthy VK, Venugopal G, Ekanayake JB, Tiong SK. Variable speed pumped hydro storage: A review of converters, controls and energy management strategies. Renew Sustain Energy Rev 2021;135:110156.
[40] Chapallaz JM, Eichenberger P, Fischer G. Manual on pumps used as turbines, Vol. 11. Deutsches Zentrum fur Entwicklungstechnologien GATE; 1992, p. 229.
[41] Dixon SL, Hall CA. Fluid mechanics and thermodynamics of turbomachinery. Seventh ed.. Butterworth-Heinemann; 2014.
[42] Stepanoff AJ. Centrifugal and axial flow pumps : theory, design and application. Wiley; 1948.
[43] Ak M, Kentel E, Kucukali S. A fuzzy logic tool to evaluate low-head hydropower technologies at the outlet of wastewater treatment plants. Renew Sustain Energy Rev 2017;68:727–37.
[44] Hogan TW, Cada GF, Amaral SV. The status of environmentally enhanced hydropower turbines. Fisheries 2014;39(4):164–72.
[45] Karassik IJ, Messina JP, Cooper P, Heald CC. Pump handbook, 4th ed.. New York: McGraw-Hill Education; 2008.
[46] Carravetta A, Derakhshan Houreh S, Ramos HM. Introduction. In: Pumps as turbines: fundamentals and applications. Springer Tracts in Mechanical Engineering, Cham: Springer International Publishing; 2018, p. 3–26.
[47] Bogenrieder W. 2.6. Pumped Storage power plants. In: Heinloth K, editor. Renewable energy, Vol. 3C. Springer-Verlag Berlin Heidelberg; 2006, p. 165–96.
[48] Breeze P. Chapter 8 - pumped storage hydropower. In: Breeze P, editor. Hydropower. Academic Press; 2018, p. 73–8.
[49] Morabito A, de Oliveira e Silva G, Hendrick P. Deriaz pump-turbine for pumped hydro energy storage and micro applications. J Energy Storage 2019;24:100788.
[50] White FM. Fluid mechanics, eighth edition. 2016.
[51] Braitsch W, Haas H. 2.7 Turbines for hydroelectric power. In: Heinloth K, editor. Renewable energy, Vol. 3C. Springer Berlin Heidelberg; 2006, p. 197–222.
[52] Novara D, McNabola A. A model for the extrapolation of the characteristic curves of pumps as Turbines from a datum best efficiency point. Energy Convers Manage 2018;174:1–7.
[53] Binama M, Su W-T, Li X-B, Li F-C, Wei X-Z, An S. Investigation on pump as turbine (PAT) technical aspects for micro hydropower schemes: A state-of-the-art review. Renew Sustain Energy Rev 2017;79:148–79.
[54] Delgado J, Andolfatto L, Covas DIC, Avellan F. Hill chart modelling using the Hermite polynomial chaos expansion for the performance prediction of pumps running as turbines. Energy Convers Manage 2019;187:578–92.
[55] Furukawa A, Shigemitsu T, Watanabe S. Performance test and flow measurement of contra-rotating axial flow pump. J Therm Sci 2007;16(1):7–13.

[56] Fahlbeck J, Nilsson H, Salehi S. Flow characteristics of preliminary shutdown and startup sequences for a model counter-rotating pump-turbine. Energies 2021;14(12):3593.

[57] Kim J-W, Suh J-W, Choi Y-S, Lee K-Y, Kanemoto T, Kim J-H. Optimized blade design of counter-rotating-type pump-turbine unit operating in pump and turbine modes. Int J Rotating Mach 2018.

[58] Kim J-H, Kasahara R, Kanemoto T, Miyaji T, Choi Y-S, Kim J-H, et al. Multi-objective optimization of a counterrotating type pump-turbine unit operated at turbine mode. Adv Mech Eng 2014;6:467235.

[59] Fahlbeck J, Nilsson H, Salehi S, Zangeneh M, Joseph M. Numerical analysis of an initial design of a counter-rotating pump-turbine. IOP Conf Series: Earth Environ Sci 2021;774(1):12066.

[60] YoosefDoost A, Lubitz WD. Archimedes screw turbines: A sustainable development solution for green and renewable energy generation—A review of potential and design procedures. Sustainability 2020;12(18):7352.

[61] Zhou D, Deng ZD. Ultra-low-head hydroelectric technology: A review. Renew Sustain Energy Rev 2017;78(May):23–30.

[62] Waters S, Aggidis GA. Over 2000 years in review: Revival of the archimedes screw from pump to turbine. Renew Sustain Energy Rev 2015;51:497–505.

[63] Sari MA, Badruzzaman M, Cherchi C, Swindle M, Ajami N, Jacangelo JG. Recent innovations and trends in in-conduit hydropower technologies and their applications in water distribution systems. J Environ Manage 2018;228:416–28.

[64] Krampe P, Ørke PR. Four-quadrant operation of rotary lobe pumps and regenerative throttling. In: Pump users international forum 2012, international rotating equipment conference 2012. 2012.

[65] Kurokawa J, Matsui J, Choi Y-D. Flow analysis in positive displacement micro-hydro turbine and development of low pulsation turbine. Int J Fluid Mach Syst 2008;1(1):76–85.

[66] Phommachanh D, Kurokawa J, Choi Y-D, Nakajima N. Development of a positive displacement micro-hydro turbine. Jsme Int J Series B-Fluids Therm Eng 2006;49:482–9.

[67] Sonawat A, Choi Y-S, Kim KM, Kim J-H. Parametric study on the effect of inlet and outlet pipe shape on the flow fluctuation characteristics associated with a positive displacement hydraulic turbine. Renew Energy 2021;163:1046–62.

[68] Sonawat A, Kim S-J, Yang H-M, Choi Y-S, Kim K-M, Lee Y-K, et al. Positive displacement turbine - a novel solution to the pressure differential control valve failure problem and energy utilization. Energy 2020;190:116400.

[69] Bocquel A, Janning J. Analysis of a 300 MW variable speed drive for pump-storage plant applications. In: 2005 european conference on power electronics and applications. 2005, p. 10 pp.–P.10.

[70] Javed MS, Ma T, Jurasz J, Amin MY. Solar and wind power generation systems with pumped hydro storage: Review and future perspectives. Renew Energy 2020;148:176–92.

[71] Jover MC. Optimal joint day-ahead energy and secondary regulation reserve scheduling of pumped-storage power plants operating with variable speed or in hydraulic short-circuit mode in the Iberian electricity market. (Ph.D. thesis), Technical University of Madrid; 2017.

[72] Next Kraftwerke GmbH. What are ancillary services?.

[73] Colas F, Qoria T, Guillaud X, Gruson F. Deliverable 3.5: Local control for GridForming converters: Experimental validation. tech. rep., 2019.

[74] Qudaih M, Engel B, Truijen D, Kooning J, Stockman K, Hoffstaedt J, et al. The contribution of low head pumped hydro storage to a successful energy transition. 2020.

[75] Siemens AG. Parallel compensation comprehensive solutions for safe and reliable grid operation. tech. rep., 2016.

[76] ENTSO-E. Synchronous condenser. ENTSO-E Technopedia 2021.

[77] Unruh P, Nuschke M, Strauß P, Welck F. Overview on grid-forming inverter control methods. Energies 2020;13(10).

[78] Laudahn S, Seidel J, Engel B, Bülo T, Premm D. Substitution of synchronous generator based instantaneous frequency control utilizing inverter-coupled DER. In: 2016 IEEE 7th international symposium on power electronics for distributed generation systems. 2016, p. 1–8.

[79] EU. DIrective (eu) 2019/944 of the European Parliament and of the council of 5 june 2019 on common rules for the internal market for electricity and amending directive 2012/27/EU. tech. rep., 2019.

[80] Kerdphol T, Watanabe M, Mitani Y, Phunpeng V. Applying virtual inertia control topology to SMES system for frequency stability improvement of low-inertia microgrids driven by high renewables. Energies 2019;12(20).

[81] Kerdphol T, Rahman FS, Mitani Y. Virtual inertia control application to enhance frequency stability of interconnected power systems with high renewable energy penetration. Energies 2018;11(4).

[82] Alizadeh Bidgoli M, Yang W, Ahmadian A. DFIM Versus synchronous machine for variable speed pumped storage hydropower plants: A comparative evaluation of technical performance. Renew Energy 2020;159:72–86.

[83] Belhadji L, Bacha S, Munteanu I, Rumeau A, Roye D. Adaptive MPPT applied to variable-speed microhydropower plant. IEEE Trans Energy Convers 2013;28(1):34–43.

[84] Guo B, Bacha S, Alamir M, Mohamed A, Boudinet C. LADRC Applied to variable speed micro-hydro plants: Experimental validation. Control Eng Pract 2019;85:290–8.

[85] Márquez JL, Molina MG, Pacas JM. Dynamic modeling, simulation and control design of an advanced micro-hydro power plant for distributed generation applications. Int J Hydrog Energy 2010;35(11):5772–7.

[86] Ducar I, Marinescu C. Increasing the efficiency of motor-pump systems using a vector controlled drive for PMSM application. In: 2014 international symposium on fundamentals of electrical engineering. 2014, p. 1–5.

[87] Iman-Eini H, Frey D, Bacha S, Boudinet C, Schanen J-L. Evaluation of loss effect on optimum operation of variable speed micro-hydropower energy conversion systems. Renew Energy 2019;131:1022–34.

[88] Abd El Maguid Ahmed W, Adel MM, Taha M, Saleh AA. PSO Technique applied to sensorless field-oriented control PMSM drive with discretized RL-fractional integral. Alex Eng J 2021;60(4):4029–40.

[89] Bonifacio J, Amann N, Kennel R. Silent low speed self-sensing strategy for permanent magnet synchronous machines based on subtractive filtering. In: 2017 brazilian power electronics conference. 2017, p. 1–6.

[90] Borkowski D. Maximum efficiency point tracking (MEPT) for variable speed small hydropower plant with neural network based estimation of turbine discharge. IEEE Trans Energy Convers 2017;32(3):1090–8.

[91] Sanchez AG, Molina MG, Lede AMR. Dynamic model of wind energy conversion systems with PMSG-based variable-speed wind turbines for power system studies. Int J Hydrog Energy 2012;37(13):10064–9.

[92] Tripathi SM, Tiwari AN, Singh D. Grid-integrated permanent magnet synchronous generator based wind energy conversion systems: A technology review. Renew Sustain Energy Rev 2015;51:1288–305.

[93] Dubrovskiy G, Peter S, Lappeen E-M, Mikerov A, Dzhankhotov V, Pyrhonen J. General comparison of direct and geared drives for control applications. In: 2014 16th european conference on power electronics and applications. 2014, p. 1–6.

[94] Touimi K, Benbouzid M, Tavner P. Tidal stream turbines: With or without a gearbox? Ocean Eng 2018;170:74–88.

[95] Cavagnino A, Lazzari M, Profumo F, Tenconi A. A comparison between the axial flux and the radial flux structures for PM synchronous motors. IEEE Trans Ind Appl 2002;38(6):1517–24.

[96] Gieras J, Wang R-J, Kamper M. Axial flux permanent magnet brushless machines. Springer; 2008, p. 55–6.

[97] Vansompel H, Sergeant P, Dupré L. Optimized design considering the mass influence of an axial flux permanent-magnet synchronous generator with concentrated pole windings. IEEE Trans Magn 2010;46(12):4101–7.

[98] Sitapati K, Krishnan R. Performance comparisons of radial and axial field, permanent-magnet, brushless machines. IEEE Trans Ind Appl 2001;37(5):1219–26.

[99] Pop AA, Jurca F, Oprea C, Chirca M, Breban S, Radulescu MM. Axial-flux vs. radial-flux permanent-magnet synchronous generators for micro-wind turbine application. In: 2013 15th european conference on power electronics and applications. 2013, p. 1–10.

[100] Kahourzade S, Mahmoudi A, Ping HW, Uddin MN. A comprehensive review of axial-flux permanent-magnet machines. Can J Electr Comput Eng 2014;37(1):19–33.

[101] Wirtayasa K, Irasari P, Kasim M, Widiyanto P, Hikmawan M. Design of an axial-flux permanent-magnet generator(AFPMG) 1 kw, 220 volt, 300 rpm, 1 phase for pico hydro power plants. In: 2017 international conference on sustainable energy engineering and application. 2017, p. 172–9.

[102] Djebarri S, Charpentier JF, Scuiller F, Benbouzid M. Design and performance analysis of double stator axial flux pm generator for rim driven marine current turbines. IEEE J Ocean Eng 2016;41(1):50–66.

[103] Mengesha S, Rajput S, Lineykin S, Averbukh M. The effects of cogging torque reduction in axial flux machines. Micromachines 2021;12:323.

[104] Laxminarayan SS, Singh M, Saifee AH, Mittal A. Design, modeling and simulation of variable speed axial flux permanent magnet wind generator. Sustain Energy Technol Assess 2017;19:114–24.

[105] Jin J, Charpentier JF, Tang T. Preliminary design of a TORUS type axial flux generator for direct-driven tidal current turbine. In: 2014 first international conference on green energy. 2014, p. 20–5.

[106] Anitha N, Bharanikumar R. Design and analysis of axial flux permanent magnet machine for wind power applications. In: 2019 international conference on power electronics applications and technology in present energy scenario. 2019, p. 1–4.

[107] El-Hasan TS. Development of axial flux permanent magnet generator for direct driven micro wind turbine. In: 2016 IEEE international conference on renewable energy research and applications. 2016, p. 169–72.

[108] Lok C, Balakrishnan V, T Subramaniam R. Implementation of hybrid pattern search–genetic algorithm into optimizing axial-flux permanent magnet coreless generator(AFPMG). Electr Eng 2017;99.

101

[109] Kowal D, Sergeant P, Dupre L, den Bossche A. Comparison of nonoriented and grain-oriented material in an axial flux permanent-magnet machine. IEEE Trans Magn 2010;46(2):279–85.
[110] He J, Somogyi C, Strandt A, Demerdash NAO. Diagnosis of stator winding short-circuit faults in an interior permanent magnet synchronous machine. In: 2014 IEEE energy conversion congress and exposition. 2014, p. 3125–30.
[111] Verkroost L, Vansompel H, Belie FD, Sergeant P. Distributed control strategies for modular permanent magnet synchronous machines taking into account mutual inductances. In: 2020 IEEE/ASME international conference on advanced intelligent mechatronics (aim), proceedings. IEEE; 2020, p. 66–71.
[112] Mohamed AHR, Vansompel H, Sergeant P. An integrated modular motor drive with shared cooling for axial flux motor drives. IEEE Trans Ind Electron 2020;1–10.
[113] Chen Y, Liang S, Li W, Liang H, Wang C. Faults and diagnosis methods of permanent magnet synchronous motors: A review. Appl Sci 2019;9(2116).
[114] Kudelina K, Asad B, Vaimann T, Rassõlkin A, Kallaste A, Khang HV. Methods of condition monitoring and fault detection for electrical machines. Energies 2021;14(22).
[115] Stetco A, Dinmohammadi F, Zhao X, Robu V, Flynn D, Barnes M, et al. Machine learning methods for wind turbine condition monitoring: A review. Renew Energy 2019;133:620–35.
[116] Lei Y, Yang B, Jiang X, Jia F, Li N, Nandi AK. Applications of machine learning to machine fault diagnosis: A review and roadmap. Mech Syst Signal Process 2020;138:106587.
[117] Lee H, Jeong H, Koo G, Ban J, Kim SW. Attention recurrent neural network-based severity estimation method for interturn short-circuit fault in permanent magnet synchronous machines. IEEE Trans Ind Electron 2021;68(4):3445–53.
[118] Ebrahimi BM, Faiz J. Feature extraction for short-circuit fault detection in permanent-magnet synchronous motors using stator-current monitoring. IEEE Trans Power Electron 2010;25(10):2673–82.
[119] Kao I-H, Wang W-J, Lai Y-H, Perng J-W. Analysis of permanent magnet synchronous motor fault diagnosis based on learning. IEEE Trans Instrum Meas 2019;68(2):310–24.
[120] Piedad EJ, Chen Y-T, Chang H-C, Kuo C-C. Frequency occurrence plot-based convolutional neural network for motor fault diagnosis. Electronics 2020;9(10).
[121] Liu Z, Chen W, Zhang C, Yang C, Chu H. Data super-network fault prediction model and maintenance strategy for mechanical product based on digital twin. IEEE Access 2019;7:177284–96.
[122] Rassõlkin A, Orosz T, Demidova GL, Kuts V, Rjabtšikov V, Vaimann T, et al. Implementation of digital twins for electrical energy conversion systems in selected case studies. Proc Est Acad Sci 2021;70(1):19–39.
[123] Falekas G, Karlis A. Digital twin in electrical machine control and predictive maintenance: State-of-the-art and future prospects. Energies 2021;14(18).
[124] Chowdhury MM, Haque ME, Saha S, Mahmud MA, Gargoom A, Oo AMT. An enhanced control scheme for an IPM synchronous generator based wind turbine with MTPA trajectory and maximum power extraction. IEEE Trans Energy Convers 2018;33(2):556–66.
[125] Demirkov B. Improved wind turbine control using maximum torque per ampere control strategy taking into account the magnetic saturation. Electrotech Electron (E+E) 2019;54(2):26–34.
[126] Salem WAA, Osman GF, Arfa SH. Adaptive neuro-fuzzy inference system based field oriented control of PMSM speed estimation. In: 2018 twentieth international middle east power systems conference. 2018, p. 626–31.
[127] Scicluna K, Staines CS, Raute R. Sensorless position control of a PMSM for steer-by-wire applications. In: 2016 international conference on control, decision and information technologies. 2016, p. 46–51.
[128] Gupta NP, Gupta P. Performance analysis of direct torque control of PMSM drive using SVPWM - inverter. In: 2012 IEEE 5th india international conference on power electronics. 2012, p. 1–6.
[129] El Mourabit Y, Derouich A, El Ghzizal A, El Ouanjli N, Zamzoum O. DTC-SVM Control for permanent magnet synchronous generator based variable speed wind turbine. Int J Power Electron Drive Syst 2017;8(4):1732–43.
[130] Foo G, Rahman MF. Sensorless direct torque and flux-controlled IPM synchronous motor drive at very low speed without signal injection. IEEE Trans Ind Electron 2010;57(1):395–403.
[131] Beng GFH. Sensorless direct torque and flux control of interior permanent magnet synchronous motors at very low speeds including standstill. (Ph.D. thesis), The University of New South Wales; 2010.
[132] Mesloub H, Boumaaraf R, Benchouia MT, Goléa A, Goléa N, Srairi K. Comparative study of conventional DTC and DTC-svm based control of PMSM motor — Simulation and experimental results. Math Comput Simul 2020;167:296–307.
[133] Staubli T, Abgottspon A. Discharge measurement in low head hydro power plants. In: 2017 international conference on energy and environment. 2017, p. 226–30.
[134] Krishnakumar R. V, Vigna KR, Gomathi V, Ekanayake JB, Tiong SK. Modelling and simulation of variable speed pico hydel energy storage system for microgrid applications. J Energy Storage 2019;24:100808.
[135] Mozafarpoor-Khoshrodi S-H, Shahgholian G. Improvement of perturb and observe method for maximum power point tracking in wind energy conversion system using fuzzy controller. Energy Equip Syst 2016;4(2):111–22.
[136] Putri R, Pujiantara M, Priyadi A, Ise T, Purnomo M. Maximum power extraction improvement using sensorless controller based on adaptive perturb and observe algorithm for PMSG wind turbine application. IET Electr Power Appl. 2018;12(4):455–62.
[137] Shahi A, Bhattacharjee C. A study analysis of fuzzy based p&o MPPT scheme in PMSG based wind turbine. In: 2018 technologies for smart-city energy security and power. 2018, p. 1–4.
[138] Borghetti A, Naldi G, Paolone M, Alberti M. Maximum efficiency point tracking for adjustable-speed small hydro power plant. 2008, p. 1–7.
[139] Chao R-M, Ko S-H, Lin H-K, Wang I-K. Evaluation of a distributed photovoltaic system in grid-connected and standalone applications by different MPPT algorithms. Energies 2018;11(6).
[140] Atta KT, Johansson A, Cervantes MJ, Gustafsson T. Phasor extremum seeking and its application in kaplan turbine control. In: 2014 IEEE conference on control applications. 2014, p. 298–303.
[141] Márquez JL, Molina MG, Pacas JM. Dynamic modeling, simulation and control design of an advanced micro-hydro power plant for distributed generation applications. Int J Hydrog Energy 2010;35(11):5772–7.
[142] Zhang J, Leontidis V, Dazin A, Tounzi A, Delarue P, Caignaert G, et al. Canal lock variable speed hydropower turbine design and control. IET Renew Power Gener 2018;12(14):1698–707.
[143] Borkowski D. Analytical model of small hydropower plant working at variable speed. IEEE Trans Energy Convers 2018;33(4):1886–94.
[144] Pérez-Diaz JI, Fraile-Ardanuy J. Neural networks for optimal operation of a run-of-river adjustable speed hydro power plant with axial-flow propeller turbine. In: 16th mediterranean conference on control and automation congress centre. 2008, p. 309–14.
[145] Heckelsmueller G. Application of variable speed operation on francis turbines. IngenierÍA E InvestigaciÓN 2015;35:12–6.
[146] Fraile-Ardanuy J, Wilhelmi JR, Fraile-Mora J, Pérez-Díaz J, Sarasúa I. Speed control of run-of-river variable speed hydro plants. 2006.
[147] Pannatier Y, Kawkabani B, Nicolet C, Simond J-J, Schwery A, Allenbach P. Investigation of control strategies for variable-speed pump-turbine units by using a simplified model of the converters. IEEE Trans Ind Electron 2010;57(9):3039–49.
[148] De Kooning JDM, Vandoorn TL, Van de Vyver J, Meersman B, Vandevelde L. Displacement of the maximum power point caused by losses in wind turbine systems. Renew Energy 2016;85:273–80.
[149] Wei C, Zhang Z, Qiao W, Qu L. Reinforcement-learning-based intelligent maximum power point tracking control for wind energy conversion systems. IEEE Trans Ind Electron 2015;62(10):6360–70.
[150] Tomin N, Kurbatsky V, Guliyev H. Intelligent control of a wind turbine based on reinforcement learning. In: 2019 16th conference on electrical machines, drives and power systems. 2019, p. 1–6.
[151] Fang H, Chen L, Dlakavu N, Shen Z. Basic modeling and simulation tool for analysis of hydraulic transients in hydroelectric power plants. IEEE Trans Energy Convers 2008;23(3):834–41.
[152] Borkowski D, Majdak M. Small hydropower plants with variable speed operation—An optimal operation curve determination. Energies 2020;13(23).
[153] Li C, Mao Y, Yang J, Wang Z, Xu Y. A nonlinear generalized predictive control for pumped storage unit. Renew Energy 2017;114:945–59.
[154] Liang L, Hou Y, Hill DJ. GPU-Based enumeration model predictive control of pumped storage to enhance operational flexibility. IEEE Trans Smart Grid 2019;10(5):5223–33.
[155] Mennemann J-F, Marko L, Schmidt J, Kemmetmüller W, Kugi A. Nonlinear model predictive control of a variable-speed pumped-storage power plant. IEEE Trans Control Syst Technol 2021;29(2):645–60.
[156] Abughalieh K, Alawneh S. A survey of parallel implementations for model predictive control. IEEE Access 2019;1.
[157] Kumar P, Saini RP. Study of cavitation in hydro turbines-A review. Renew Sustain Energy Rev 2010;14(1):374–83.
[158] Mover, Working Group Prime and Supply, Energy. Hydraulic turbine and turbine control models for system dynamic studies. IEEE Trans Power Syst 1992;7(1):167–79.
[159] Berrada A, Loudiyi K, Garde R. Dynamic modeling of gravity energy storage coupled with a PV energy plant. Energy 2017;134:323–35.
[160] Jaeger ED, Janssens N, Malfliet B, Van De Meulebroeke FV. Hydro turbine model for system dynamic studies. IEEE Trans Power Syst 1994;9(4):1709–15.
[161] Mohanpurkar M, Ouroua A, Hovsapian R, Luo Y, Singh M, Muljadi E, et al. Real-time co-simulation of adjustable-speed pumped storage hydro for transient stability analysis. Electr Power Syst Res 2018;154:276–86.
[162] Sharma JD, Kumar A. Development and implementation of non- linear hydro turbine model with elastic effect of water column and surge tank. Int J Electr Electron Res 2014;2(4):234–43.

[163] Taniguchi H, Nagao T, Higasa H. Development of a pumped-storage power station model for power system stability study. Electr Eng Japan 1992;112(3):50–62.
[164] Vytvytsky L, Lie B. Comparison of elastic vs. inelastic penstock model using OpenModelica. In: Proceedings Of the 58th conference on simulation and modelling, Vol. 138. reykjavik, iceland; 2017, p. 20–8, september 25th – 27th, 2017.
[165] Kuiper G. Chapter 3 physics of cavitation : GAS CONTENT. Cavitation Ship Propuls 2010;9–79.
[166] Franc J-P, Michel J-M. Fundamentals of cavitation. 2005.
[167] Šarc A, Stepišnik-Perdih T, Petkovšek M, Dular M. The issue of cavitation number value in studies of water treatment by hydrodynamic cavitation. Ultrason Sonochemistry 2017;34:51–9.
[168] Carlton J. Marine propellers and propulsion. 2019.
[169] Kumar PS, Pandit AB. Modeling hydrodynamic cavitation. Chem Eng Technol 1999;22:1017–27.
[170] Papaefthimiou S, Papathanassiou S. Modeling of a variable speed wind turbine with synchronous generator. In: European wind energy conference and exhibition 2009, Vol. 7. EWEC 2009, (ISIE):IEEE; 2009, p. 4439–48.
[171] Wu F, Zhang XP, Ju P. Modeling and control of the wind turbine with the direct drive permanent magnet generator integrated to power grid. In: 3rd international conference on deregulation and restructuring and power technologies. (April):2008, p. 57–60.
[172] De Kooning JDM, Vandoorn TL, de Vyver J, Meersman B, Vandevelde L. Displacement of the maximum power point caused by losses in wind turbine systems. Renew Energy 2016;85:273–80.
[173] Kral C, Pirker F, Pascoli G. The impact of inertia on rotor faults effects theoretical aspects of the vienna monitoring method. In: 2007 IEEE international symposium on diagnostics for electric machines, power electronics and drives, Vol.23. (4):2007, p. 77–82.

B.2 Published

Gans, L.H.A., Trivedi, C., Iliev, I., & Storli, P.T. (2023). An experimental and numerical study of a three-lobe pump for pumped hydro storage applications. *Journal of Physics: Conference Series, 2629(1)*, 012010. https://doi.org/10.1088/1742-6596/2629/1/012010

Abstract Pumped hydro storage (PHS) plays an important role as a matured technology that accounts for the vast majority of global energy storage capacity, and its expansion is therefore desirable. The expansion of PHS in mid- and high-water heads is limited to topographic features, but there is an untapped potential in low-head applications. For most of the PHS applications, a Francis reversible pump-turbine (RPT) is regarded as the most common and cost-effective machine, but it is not a suitable option for water heads of less than 30m. In its place, positive displacement machines like lobe pumps could potentially work as RPT machines and unleash new possibilities for low-head pumped hydroelectric storage. In addition, unlike bladed pump-turbines, lobe pumps-turbines present a fish friendliness design, an important attribute to preserve the aquatic wildlife. This work will therefore present a three-lobe pump that could potentially be used in low-head PHS. An experimental model for a lobe machine will be presented, and its results will be used to validate the computational fluid dynamic simulations. Numerical investigations will address the characteristic curves regarding water-head, rotation speed and flow rate.

Contribution I took on the role of the main contributor to this paper, overseeing the execution of numerical simulations for validation purposes. The conceptualization and design of the experimental setup were collaborative efforts with our partner at Chalmers University of Technology. The Chalmers team was responsible for the complete execution of the experiments. The publication covers parts of Chapter 4.

An experimental and numerical study of a three-lobe pump for pumped hydro storage applications

L H A Gans[1*], C Trivedi[1], I Iliev[2] and P T Storli[1]

[1] Department of Energy and Process Engineering, Norwegian University of Science and Technology, Alfred Getz' vei 4, 7034 Trondheim, Norway
[2] SINTEF Energi AS, Sem Sælands vei 11, 7034 Trondheim, Norway
*E-Mail: luiz.h.a.gans@ntnu.no

Abstract. Pumped hydro storage (PHS) plays an important role as a matured technology that accounts for the vast majority of global energy storage capacity, and its expansion is therefore desirable. The expansion of PHS in mid- and high-water heads is limited to topographic features, but there is an untapped potential in low-head applications. For most of the PHS applications, a Francis reversible pump-turbine (RPT) is regarded as the most common and cost-effective machine, but it is not a suitable option for water heads of less than 30m. In its place, positive displacement machines like lobe pumps could potentially work as RPT machines and unleash new possibilities for low-head pumped hydroelectric storage. In addition, unlike bladed pump-turbines, lobe pumps-turbines present a fish friendliness design, an important attribute to preserve the aquatic wildlife. This work will therefore present a three-lobe pump that could potentially be used in low-head PHS. An experimental model for a lobe machine will be presented, and its results will be used to validate the computational fluid dynamic simulations. Numerical investigations will address the characteristic curves regarding water-head, rotation speed and flow rate.

Keywords: Lobe pump, pumped hydro storage, experiment, numerical validation.

1. Introduction

With a growing share of intermittent renewable energy sources, especially solar and wind power, and as a means to allow a higher penetration of these energy supplies, the implementation and expansion of energy storage systems will be necessary to maintain grid stability and enhance its flexibility. Energy storage technologies can detain energy during periods when demand or costs are low, or when electricity supply exceeds demand, and can return that same energy when demand or energy costs are high. Hoffstaedt et al. (2022) made an extensive review on technologies that could suit low-head pumped hydro storage (LH PHS), a promising field in terms of energy storage where systems typically operate at water heads lower than 30m, but that lacks further investigations and full scale experiments in real life scenarios. The same authors address different reversible pumps and turbines machines that could address the challenges in low-head applications, in lieu of Francis turbines which is the dominant technology for PHS in mid- and high-head applications but that are not suitable for low elevations. One of the technologies mentioned is the lobe pump, a positive displacement machine that can be reversible and also work in turbine mode. Regarding turbine mode, Sonawat et al. (2021) find positive displacement turbines in applications with low flowrate, high head and lower specific speeds, operating below the operational range of conventional turbines.

1.1 Positive displacement machines

Positive Displacement (PD) machines are a type of fluid handling equipment that work by trapping a fixed amount of fluid and then forcing it to move between two locations. Unlike centrifugal pumps, which rely on the kinetic energy of the fluid to move it, PD machines maintain a constant flow rate by changing the volume of the fluid trapped inside the chambers of the pump. This makes them ideal for applications where maintaining a consistent flow rate is important.

Hoffstaedt et al. (2022) explain that a lobe pump presents an efficiency that remains relatively stable despite changes in head. The lack of sharp blades contributes to a more fish-friendly design, particularly when operating at low rotation speeds. These qualities are desirable in a LH PHS application. However, lobe machines have yet to be proven as a viable alternative.

1.2 Design aspects of lobe pumps and turbines

Rotary positive displacement machine such as lobe pumps and turbines present clearances between rotors and casing, and also clearances between both rotors. These gaps are expected to prevent the rotors to touch each other or to touch the casing at any instant of the pump or turbine operation. If there is any contact point, changes in flow rate, pressure drop, leakages and surface wear may occur and affect the operation of the machine. Plus, depending on the clearance sizes, cavitation and unwanted vibrations can occur. Phommacchanh et. al. (2006) showed in their PD turbine that it achieved a higher efficiency than a conventional turbine and it could sustain high efficiencies under the wide range of operating conditions. They also found out that the efficiency of turbine mode is much improved when reducing the clearance between the rotating and stationary parts of the turbine because of the amount of water leakage through those gaps. Complementary, they noticed that the torque efficiency of small side clearances decreased noticeably in the range of low-pressure region. But the improvement of the volumetric efficiency of the turbine with small side clearances was much higher than the torque efficiency reduction. Also, PD turbine with a smaller side clearance obtained much higher output power and consequently higher efficiency than the case with a large clearance at the same head and flow rate. Kang et al. (2012) also made the same conclusions, and proved that smaller clearances between rotor and casing walls produced much higher efficiencies, while the gap between lobes should be verified individually for each case.

The rotor surface profile can affect performance considerably. Kang et al. (2012) investigated this topic and they found that less pressure drop was generated by the cycloidal lobe. They also stated that the combination of less vortex and lower speed helps epicycloidal lobe pump to take an advantage over circular lobe pump, since it would prevent backward flow from the discharge area to suction area. Another advantage for the cycloidal profile was that it generated a characteristic curve with higher slope ratio, which resulted in higher efficiency of the pump because of the smaller leakage level in pump mode. Plus, the average value of pressure head of epicycloidal lobes was nearly 10% higher than that of circular pump in all studied cases. Finally, multi-lobe pumps with up to 4 lobes were compared, and they found that both tri- and four-lobe pumps provided more stable output and higher capacity than the two-lobe design, with no important differences between the tri- and four-lobe pumps. At the same time, the use of multi-lobes did not improve pump performance.

Finally, in order to reduce pressure pulsation, Kurokawa et al. (2008) explained that one can install a small sized simple surge tank at the inlet and outlet of the turbine, and that could reduce the pulsation amplitude by 75%. However, it should be possible to reduce pulsation without installing supplemental (and expensive) structures. That is one of the reasons why the authors studied a pair of four-lobe type rotor twisted helically with a twist of 11º, and they compare it with a three-lobe rotor. The authors explain that pressure pulsation increases remarkably with an increase of rotational speed and differential pressure in a three-lobe straight turbine. In the other hand, the twisted rotors reduced to about 20% of that by straight three-lobe rotor. As the helical lobe presents a bigger surface area, leakages are expected to be higher through both tip clearances and centre clearances. Torque and leakage are almost dependent only on the differential pressure, same as the straight 3-lobe type, but torque efficiency becomes much higher.

Complementary, Sonawat et al. (2021) say that machines that suffer of large pulsations in the flow can cause the generation of noise, vibration and fatigue, leading to the structural damage or breakdown of the device. So, they suggest the use of twisted rotors in order to damp most of the flow fluctuations. Sonawat et al. (2020) had a special look at the occurrence of cavitation in PD turbines by doing multi-phase CFD simulations, and they showed that the utilization of a 45º twisted rotor could practically eliminate the occurrence of cavitation because the contact area of the fluid for both rotors was uniform irrespective of the orientation or rotation of the lobes. Hence there was no abrupt change in the fluid properties. In the other hand, the 45º twisted rotor produced 1.15% less theoretical hydraulic efficiency compared to the straight lobe design due to increase in the leakage losses associated with it. But a vibration free device ensures a better longevity of the machine, which also can reduce maintenance costs.

2. Experimental setup

A model scale experiment was designed and built by the Laboratory of Fluid and Thermal Science group at Chalmers University of Technology to verify how a lobe machine would behave in low rotation speeds and it was used to validate the numerical simulations in this work.

First, one set of experiments was executed by the Chalmers group and it did not contain a diffuser in the design, as shown in Figure 1. Later, a diffuser was introduced at the inlet in order to smooth the flow transition. The experiment with the modified geometry was carried out by the Norwegian group at Chalmers University. As shown in Figure 1, the experimental rig consisted of two pipes connecting to the main channel which contained the PD RPT. The geometry consists of a casing and two straight rotors with three lobes each that follow a cycloidal profile. Twisted rotors were not considered in this work because the low rotational speed is intended for this experiment, thus vibration and cavitation should not be present, and a straight surface shape should provide a better hydraulic efficiency. Driving and driven rotors are synchronized with a gearbox. Rotors were 3D-printed and manufactured in acrylic (PMMA), as well as the housing that constrains the water flow. The overall design and dimensions can be seen at Figure 1 and the rig in Figure 2.

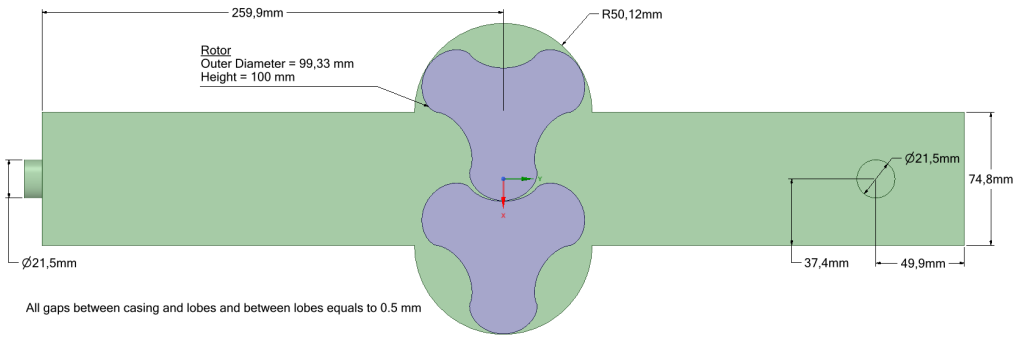

Figure 1. Lobe pump machine designed in model scale.

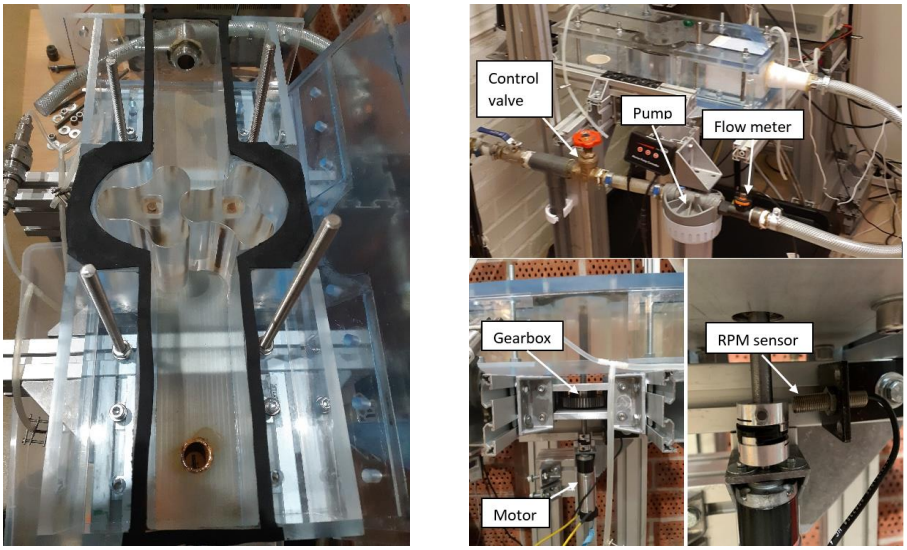

(a) (b)

Figure 2. Rig layout for the lobe machine. (a) Top view and (b) equipment for operating the rig.

The test setup is a circular system, as depicted in Figure 2, where the water travels from the bottom outlet of the testing section, through a hose, through a flow meter, through a control valve, through an external pump, and back to the inlet of the testing section. The control valve is employed to adjust the necessary head during pump mode. The rotor lobes are rotated by a motor and a gearbox that connects the rotation of the two rotors, causing them to rotate at the exact same rotational speed but in opposite directions. An RPM sensor is used to monitor the rotational speed.

3. Numerical setup

Computational Fluid Dynamic (CFD) simulations were prepared in ANSYS 2020 R2 and CFX Solver. Transient simulations with single-phase water covering a single rotor revolution were sufficient to obtain stable pulsation values.

The immersed boundary method (IBM) was chosen to simulate the fluid-structure interaction in this problem. IBM treats the rotors as immersed bodies that indicates which numerical cells are inside the fluid or solid domain and interpolates values along the solid-fluid interface at the rotor surface (ANSYS CFX Refence Guide, 2020). IBM allows to gain computational time without the need to recalculate the numerical mesh for each time step. As consequence, the velocity in the fluid region that overlaps the immersed solid is enforced through a body force in the momentum equations. Therefore, a Momentum Source Scaling Factor (MSSF) is defined in CFX as a representation of the penalty method. In this method, fluid-structure interaction is modelled as a penalty force added to the fluid momentum equation that penalizes fluid velocity when it penetrates the structure. A higher MSSF value results in a closer match between fluid velocity and solid body velocity, leading to a lower error, but it also increases the likelihood of solver failure as the forcing term becomes larger, causing the numerical system to become stiff. So, an automatic solver control was set to control the MSSF. ANSYS CFX User Manual states that for a gear pump (a machine with similar behaviour to lobe pump), flow rate errors can be as high as 50% for MSSF equals to 10, and 9% for MSSF equals to 100.

Figure 3 shows the created mesh, and its statistics are described in Table 1. An inflation layer with 7 prisms was created to fill the space between the rotors and casing, so the leakages around the lobes could be properly modelled by the IBM method. The mesh refinement for the immersed body only needs to accurately depict the surface profile of the lobe.

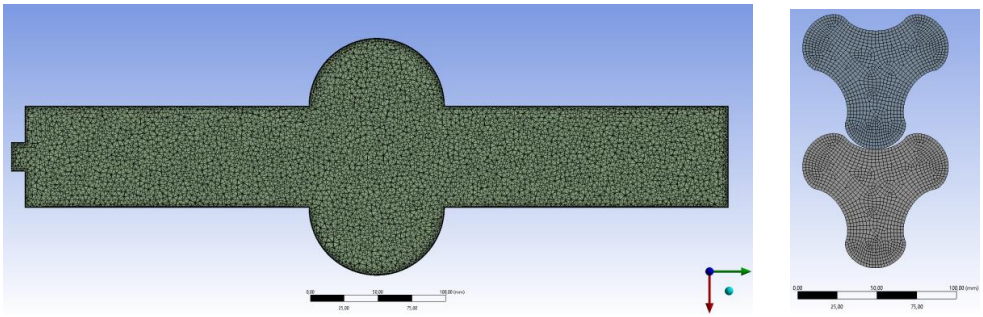

(a) (b)

Figure 3. Mesh for (a) Fluid Domain (stationary) and (b) Immersed Solid domain (rotating).

Table 1. Mesh statistics

Mesh	Unstructured + Inflation
Number of nodes	916 507
Number of elements	2 277 848

Preliminary transient simulations showed that maximum Courant number achieved values under 1.0 over all the domain for all time steps, showing that a time step equivalent to 1º of rotation was sufficient to represent the CFD simulation in this work. Table 2 shows the calculated time-step and total simulation time expressions, which are only dependent on the rotational speed of the rotors.

Table 2. Analysis settings

Analysis Type	Transient
Total time for each simulation	1 complete turn, t = 1/(n[rpm]*60)
Time Step	1º of rotation, dt = 1/(n[rpm]*60)/360

Different boundary conditions for rotating displacement pump simulations were tested by Schiffer (2012), who also used IBM in ANSYS CFX. Thus, Table 3 indicates the boundary conditions that represented the experimental setup.

Table 3. Settings and Boundary conditions

Domain	CFX Options	Boundary conditions / Settings
Fluid (stationary)	Opening at low pressure side	Opening Pressure and Direction, Relative Pressure = 1 atm, Normal to boundary condition
	Opening at high pressure side	Opening Pressure and Direction, Relative Pressure = 1 atm + ‘measured pressure difference’, Normal to boundary condition
	Walls	No slip
	Turbulence Model	Shear Stress Transport, Automatic wall function
Immersed Solid (rotating)	Angular Velocity	30/35/40/45/50/55/60 rpm

4. Results and discussions

This study, following Schiffer (2012), verified the appropriate use of boundary conditions and allowed us to obtain and compare the average values for flow rate and pressure difference without the need to analyse the pulsation behaviour commonly found in positive displacement machines.

All the experimental tested points are indicated in Figure 4. It shows the characteristic pump curves for two configurations: one with and one without a diffuser at the inlet.

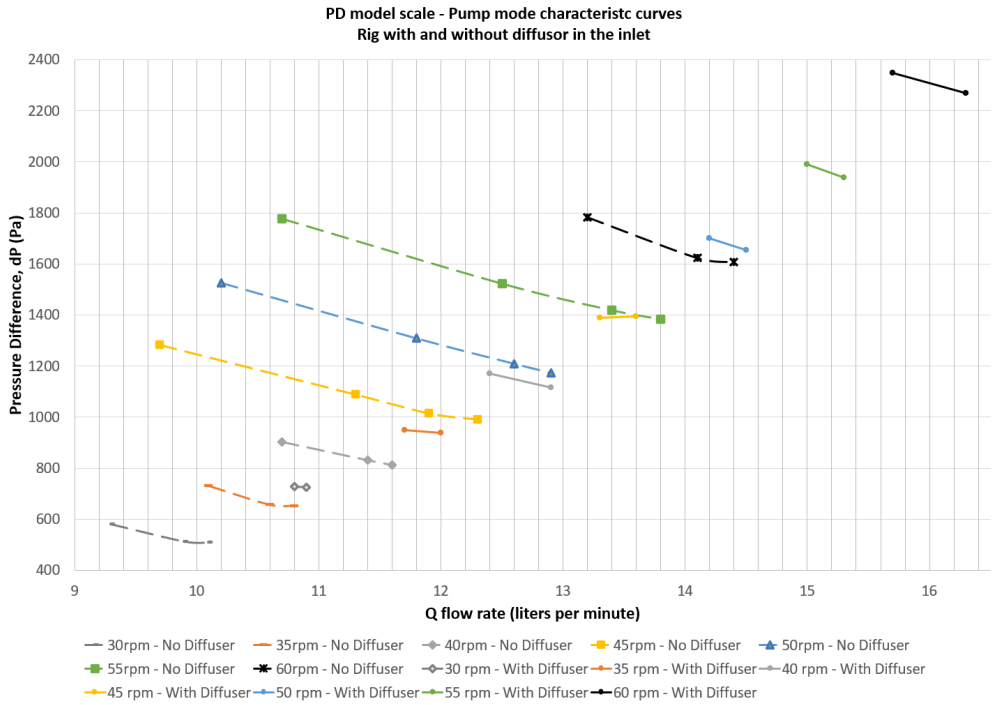

Figure 4. Experimental results for PD model scale

In Figure 4 the characteristic curves for both cases present a linear relation between flow rate and pressure difference, as expected in lobe pumps. Rotors operate between 30 and 60 rpm, and they produced flow rates between 9 and 16 litres per minute when pressure differences between 400 and 2400 Pa were imposed, which represents equivalent water-heads ranged from 4 to 23 cm. The higher the rotation speed, the higher the generated flow rate. We can also notice that, for the same rotation speed, the characteristic curves between the two geometries differ considerably, even though the only additional feature, the diffuser, was included in the inlet and did not interfere directly in the rotors zone. Thus, the diffusor was able to reduce drag by slowing down the fluid velocity and spreading it over a larger area, which reduced the turbulence and kinetic energy, and promoted a more efficient flow. So, it was observed that the small scale of the experimental model was very sensitive to variations in geometry or operation conditions, even small ones. Kang et al. (2012) addressed the same difficulties in measurements and measuring equipment can have significant errors.

Figure 5 shows the comparison between experimental and numerical data for the configuration without a diffuser in the inlet.

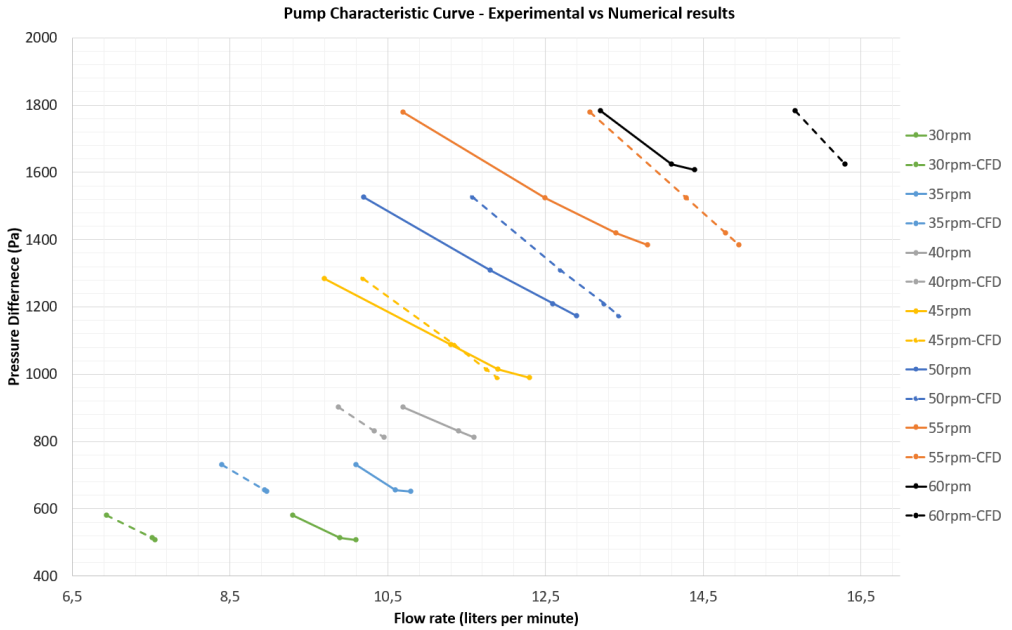

Figure 5. Comparison between experimental and numerical data for geometry without a diffuser.

In Figure 5, all points stayed below 5% error for rotation speed equals to 45 rpm. At 30 and 60 rpm, errors increased up to ±25%. We can also observe that the slope of the experimental and numerical curves remains the same inside the same set, but the numerical slope is a little higher than the experimental ones, which indicates that the numerical simulations underestimated the real leakages. Different reasons can explain those results. Initially, a higher MSSF could also decrease the error since IBM can induce unrealistic numerical leakage through the immersed solid bodies. Also, a more detailed mesh could be applied along the centreline of the model to accurately capture leakage between lobes. Moreover, the presence of bubbles during the experiment, although minimal, and the difficulty of maintaining the lobes with a constant rotor-rotor gap value could have generated abnormal behaviour in the system. Despite the differences explained above, errors were still under the estimated range provided by the ANSYS CFX Reference Guide.

Finally, due to the compact size of the test setup, the mechanical losses in the gearbox and seals prevented the runner from rotating in turbine mode, regardless of the head and flow rate. Hence, the motor had to be employed also in turbine mode to overcome those losses, so a net hydraulic torque could be estimated from the resulting pressure difference and flow rates. Despite the adjustments, significant uncertainties were still present and prevented this machine to provide reliable data in turbine mode.

5. Conclusions

A three-lobe pump was studied to investigate the potentials of positive displacement machines as reversible pump turbine units for low-head pumped hydro storage applications. Linear relationship between flow rate and water head was observed in both experiment and numerical analyses. In pump mode the model scale achieved around 16 litres per minute of flow rate when operating at 60 rpm, under water-heads close to 23cm, and in the presence of a diffuser. Because of the closed loop configuration of the experiment and scale of the model, it was not possible to test the machine in higher head conditions, and small variations led to big uncertainties. Numerical simulations followed the experimental trends, but despite the numerical errors being within the expect errors for the IBM technique, a mesh refinement located in the centreline should be implemented to improve the accuracy and reduce the discrepancy between CFD and experimental data. A higher MSSF value could also

decrease unrealistic leakages through the solid bodies. Apart from the pump mode, the small-scale machine presented too high mechanical losses in the system that prevented it to operate in turbine mode. Therefore, the next step is to build another experiment with two open reservoirs in two different levels in order to provide the necessary setup to study the lobe machine in turbine mode, and as a full reversible pump-turbine machine intended for LH PHS. With a bigger model, experimental uncertainties are expected to decrease, and global efficiencies, torques and generated power can be estimated. With the new experiment, a numerical study could be validated for turbine mode and eventually provide an optimized design for the round trip of the PD RPT machine.

Acknowledgements

We would like to express our gratitude to Petter Miltén, Professor Valery Chernoray and Professor Håkan Nilsson from the Laboratory of Fluid and Thermal Science at Chalmers University of Technology for their invaluable contributions to the design and execution of the experiments presented in this paper. Their expertise and support were essential to launch and investigate this innovative project. This project has received funding from the European Union's Horizon 2020 research and innovation programme under grant agreement No. 883553.

References

[1] Hoffstaedt J P, Truijen D P K, Fahlbeck J, Gans L H A, Qudaih M, Laguna A J, de Kooning J D M, Stockman K, Nilsson H, Storli P-T, Engel B, Marence M & Bricker J D 2022, *Low-head pumped hydro storage: A review of applicable technologies for design, grid integration, control and modelling*. Renewable and Sustainable Energy Reviews **158**, 112119. https://doi.org/10.1016/J.RSER.2022.112119

[2] Sonawat A, Choi Y-S, Kim K M, Kim J-H 2021, *Parametric study on the effect of inlet and outlet pipe shape on the flow fluctuation characteristics associated with a positive displacement hydraulic turbine*, Renewable Energy **163**, pp 1046-1062, ISSN 0960-1481, https://doi.org/10.1016/j.renene.2020.09.025

[3] Phommacchanh D, Kurokawa J, Choi Y D, Nakajima N 2006, *Development of a positive displacement micro-hydro turbine*. JSME International Journal, Series B, Vol. 49, No. 2, pp. 482-489. doi:10.1299/jsmeb.49.482

[4] Kang Y-H, Vu H-H and Hsu C-H 2012, *Factors Impacting on Performance of Lobe Pumps: A Numerical Evaluation.* Journal of Mechanics **28**, pp 229-238 doi:10.1017/jmech.2012.26

[5] Kurokawa J, Matsui J, Choi Y-Do 2008, *Flow Analysis in Positive Displacement Micro-Hydro Turbine and Development of Low Pulsation Turbine*, International Journal of Fluid Machinery and Systems, Volume 1, Issue 1, Pages 76-85, Online ISSN 1882-9554, https://doi.org/10.5293/IJFMS.2008.1.1.076

[6] ANSYS CFX Reference Guide, Fluid Structure Interaction, Release 2020 R2.

[7] ANSYS CFX Solver Theory Guide, Release 2020 R2.

[8] Sonawat A, Kim S-J, Yang H-M, Choi Y-S, Kim K-M, Lee Y-K, Kim J-H 2020, *Positive displacement turbine - A novel solution to the pressure differential control valve failure problem and energy utilization*, Energy **190**, 116400, ISSN 0360-5442, https://doi.org/10.1016/j.energy.2019.116400

[9] Schiffer J 2012, *A comparison of CFD-calculations and measurements of the fluid flow in Rotating Displacement Pumps*. International Rotating Equipment Conference 2012, Düsseldorf.

B.3 Published

Gans, L.H.A. & Storli, P-T (2023). Multidisciplinary optimized PD design. *European Union's Horizon 2020, ALPHEUS*, grant agreement 883553. `https://alpheus-h2020.eu/wp-content/uploads/2020/06/D2.4-Multidisciplinary-optimized-PD-design-V2.0.pdf`

Executive Summary This report presents the work and conclusions regarding the multidisciplinary optimization of a positive displacement reversible pump-turbine (PD RPT) machine. Both an analytical and numerical model of such a PD RPT is made, analysed for 10 MW scale and laboratory scale, respectively. The analytical model is partially verified and includes fish mortality and the subsequent effect on main dimensions if fish mortality is given a cost. The conclusion is that a PD RPT is likely not to be a fish friendly energy storage machine for the longer (> 1m) fish species found in coastal regions. The numerical model is validated using high-fidelity experimental results and is used to optimize the laboratory scale test rig that will be manufactured and experimentally studied in the ALPHEUS project. A structural analysis of the operation of this indicates that there are no reasons for concern with respect to structural integrity and fatigue of this laboratory scale model.

Contribution The primary contribution of the author to this report involved supplying essential simulations for addressing the multidisciplinary optimization of a positive displacement reversible pump-turbine (PD RPT) machine. In addition to conducting a literature review on lobe pumps and turbines and detailing the experimental setup, I assumed responsibility for incorporating numerical validation of the Computational Fluid Dynamics (CFD) models, utilizing existing experimental and Particle Image Velocimetry (PIV) data, and conducting sensitivity tests. I conducted numerical simulations to determine optimal gap sizes, channel dimensions, and provided characteristic curves for flow rate, efficiency, and power for the design of a new rig. Furthermore, I performed fluid-structure simulations to evaluate mechanical loads and ensure the safety of the new machine.

The publication covers parts of Chapters 4 and 5.

B.4 In preparation

Gans, L.H.A., Iliev, I, Storli, P.-T., Trivedi, C (n.d.). CFD modeling and PIV experimental validation of flow fields of a three-lobe reversible pump-turbine. *Computers & Fluids* (target journal)

Abstract This study combines Computational Fluid Dynamics (CFD) modeling and Particle Image Velocimetry (PIV) experimental validation to comprehensively investigate the flow fields of a three-lobe reversible pump-turbine. The CFD model captures the intricate fluid dynamics within the pump-turbine through detailed numerical simulations, offering insights into the complex interactions of flow phenomena. The model's accuracy is rigorously assessed and validated through numerical sensitivity studies and PIV experiments, providing a robust foundation for understanding flow behavior. This integrative approach enhances our understanding of the three-lobe reversible pump-turbine's hydraulic performance and contributes to developing efficient and reliable pump-turbine technologies.

Contribution This publication aims to contribute to Chapter 3 and Chapter 4, highlighting vital aspects related to the numerical validation of positive displacement machines, particularly reversible lobe pumps operating at extremely low rotations and showcasing their inherent flow characteristics.

Gans, L.H.A., Trivedi, C, Iliev, I, Storli, P.-T. (n.d.). A comparison between the immersed boundary method and the dynamic mesh technique as CFD tools in lobe pump and hydropower applications. *International Journal of Computational Fluid Dynamics* (target journal)

Abstract The dynamic mesh and the immersed boundary (IB) method can be used to address problems with boundary motion. While the dynamic mesh can apply three dynamic schemes (smoothing, layering, and remeshing) to recreate the numerical mesh for each time step and then replace the boundary conditions in the Navier-Stokes equations, the IB method does not interfere with the mesh of the fluid domain over time, but it evaluates the fluid-structure interaction through interpolations around the interface. Since both methods can be used when an incompressible body emerges in an incompressible fluid domain, this work aims to investigate each technique's advantages and disadvantages. A particular focus is given to the computational cost and accuracy of the results. This study evaluates its numerical application in a lobe pump intended for pumped hydro storage applications. A model scale provided the experimental data in order to assess the accuracy of the numerical results, whose boundary conditions depended only on the rotational speed of the lobes and the water head in the system. Numerical investigations will analyze and compare flow rate values and velocity fields, turbulence models, mesh

refinement for solid and fluid domains, mesh inflation near the gaps of the lobe pump and casing (intended for wall function calculations), and the correspondent mesh quality criteria.

Contribution This publication aims to elucidate the advantages and disadvantages of two distinct meshing techniques employed in CFD simulations, as elaborated in Chapter 4. It delves into various numerical aspects, including Y+ values, Courant numbers, computational time, and numerical stabilities.

Gans, L.H.A., Iliev, I, Storli, P.-T., Trivedi, C (n.d.). A numerical design study of a three-lobe reversible pump-turbine for seawater low-head pump hydro storage. *Journal of Energy Storage* (target journal)

Abstract This study conducts a numerical design investigation into the performance of a three-lobe reversible pump-turbine designed for low-head seawater pumped hydro storage. Utilizing computational fluid dynamics simulations, we systematically analyze the impact of key design parameters on efficiency and hydraulic performance. The model, validated against experimental data, reveals insights into the trade-offs and considerations crucial for optimizing energy conversion efficiency and operational flexibility. The findings contribute to understanding reversible pump-turbines, particularly in the context of sustainable energy storage solutions for coastal environments. This research lays the groundwork for future experimental validation and practical implementation, offering a promising avenue for advancing seawater low-head pumped hydro storage technologies.

Contribution This publication is designed to augment the content in Chapter 6 by conducting a comparison and validation against experimental data obtained from a forthcoming rig of a reversible three-lobe pump-turbine, set to be assembled at TU Braunschweig.